EFFECTS OF HEAVY DOPING
AND METALLIC CONTAMINATION ON ELECTRICAL CHARACTERISTICS OF SEMICONDUCTOR DEVICES

BY

KER-WEN TENG

A DISSERTATION PRESENTED TO THE GRADUATE COUNCIL
OF THE UNIVERSITY OF FLORIDA IN
PARTIAL FULFILLMENT OF THE REQUIREMENTS
FOR THE DEGREE OF DOCTOR PHILOSOPHY

UNIVERSITY OF FLORIDA

1984

ACKNOWLEDGEMENTS

I am indebted to my family for their encouragement and parental support which helped me pursue my graduate studies.

Throughout the course of this study, I benefited significantly from suggestions, encouragement, and support of my advisor, Professor Sheng S. Li. His research insignt and excellent tutoring in semiconductor electronics have been invaluable for developing and guiding my research.

I extend my gratutude to Professors A. Neugroschel and D. Burk for their helpful discussions and participation on my committee. I am also grateful to Professors T. Anderson and P. H. Holloway for their interests in serving on my committee.

Appreciation is extended to my collegues, W. Krull and S. Y. Yang, for their many stimulating discussions.

I would like to express my appreciation to my typist, Mrs. Claire Myers, for her excellent work.

Finally, no words can adequately describe the support, understanding, and effort of my wife, Ellen, in preparing this dissertation with me.

Table of Contents

Page

ACKNOWLEDGEMENTS....................ii

LIST OF SYMBOLS....................vii

ABSTRACT....................x

CHAPTER

I. INTRODUCTION....................1

II. EFFECTS OF HEAVY DOPING ON THE BUILT-IN POTENTIAL, DEBYE LENGTH, DEPLETION LAYER WIDTH, AND DEPLETION CAPACITANCE IN A HEAVILY-DOPED PN JUNCTION DIODE....................5

2.1 Introduction....................5

2.2 Models for the heavy doping effects....................6

2.2.1 The carrier degeneracy....................6

2.2.2 The dopant impurity density-dependent dielectric constant....................7

2.2.3 The bandgap narrowing....................9

2.3 Derivation....................10

2.3.1 Built-in potential....................10

2.3.2 Debye length....................11

2.3.3 Depletion layer width and depletion capacitance...12

2.4 Results and Discussion....................16

2.5 Summary and Conclusion....................19

III. EFFECTS OF HEAVY DOPING ON THE EINSTEIN RELATION....................30

3.1 Introduction....................30

3.2 Theoretical analysis....................31

3.2.1 Einstein relation for majority carriers..........31

3.2.2 Einstein relation for minority carriers..........33

3.3 Discussion..........35

IV. THEORY OF ELECTRICAL CHARACTERISTICS OF A HEAVILY-DOPED PN DIODE..........40

4.1 Introduction..........40

4.2 Theoretical treatment..........42

4.2.1 Electrical potential and carrier densities..........42

4.2.2 Built-in potential..........44

4.2.3 Graded junction diode..........46

4.3 Results and Discussion..........53

4.4 Summary and conclusions..........56

V. EFFECTS OF HEAVY DOPING ON THE BUILT-IN POTENTIAL, DEPLETION LAYER WIDTH, DEPLETION CAPACITANCE, AND I-V CHARACTERISTICS OF A HEAVILY-DOPED HETEROJUNCTION DIODE..........61

5.1 Introduction..........61

5.2 Graded heterojunction..........63

5.2.1 Built-in potential..........63

5.2.2 Depletion layer width and depletion capacitance...65

5.3 Abrupt heterojunction..........67

5.3.1 Built-in potential..........67

5.3.2 Depletion layer width and depletion capacitance...69

5.3.3 I-V characteristics..........70

5.4 Results and discussion..........72

5.5 Summary and Conclusions..........74

VI. EFFECTS OF HEAVY DOPING ON I-V CHARACTERISTICS OF GaAs JFET AND MESFET DEVICES..........86

6.1 Introduction..........86

6.2 Theoretical analysis....................................88

6.3 Results and discussion..................................91

6.4 Summary and conclusion..................................93

VII. EXPERIMENTAL METHODS FOR STUDYING THE METALLIC CONTAMINATION IN SILICON DEVICES..............................98

7.1 Current-voltage (I-V) measurement.......................98

7.2 Capacitance-voltage (C-V) measurement..................100

7.3 Thermally stimulated capacitance (TSCAP) measurement....101

7.4 Deep level transient spectroscopy (DLTS) measurement....103

7.4.1 Principles of the DLTS technique.................104

7.4.2 Minority carrier injection.......................105

7.4.3 Majority carrier injection.......................105

7.4.4 Trap concentration...............................106

7.4.5 Activation energy of a deep level trap...........107

VIII. THE EFFECTS OF METALLIC CONTAMINATION ON THE DEVICE PERFORMANCE...................................115

8.1 Introduction..115

8.2 Tested devices and structures..........................117

8.3 Experimental observation...............................117

8.3.1 Results and discussion on phase 1 group B (P1PB) diodes............................118

8.3.2 Results and discussion on phase 1 group C (P1PC) diodes............................119

8.3.3 Results and discussion on phase 1 group D (P1P2) MOS capacitors...................120

8.3.4 Results and discusson on phase 2 part 1 (P2P1) diodes............................124

8.4 Summary and conclusion.................................126

IX. SUMMARY AND CONCLUSION.................................171

APPENDIX DERIVATION OF THE DEPLETION LAYER WIDTH VS. BUILT-IN POTENTIAL FOR A HEAVILY DOPED LINEARLY GRADED PN JUNCTION.............................174

REFERENCES 177

BIOGRAPHICAL SKETCH...181

LIST OF SYMBOLS

a	net doping concentration gradient of a linearly graded junction.
$C_{jA(L)}$	depletion capacitance per unit area in an abrupt (linearly-graded) p-n junction.
C_0	depletion layer capacitance.
ΔC	capacitance change due to the majority or minority carrier emission.
E_c^N	conduction band edges in the quasi-neutral n-region.
E_v^P	valence band edges in the quasi-neutral p-region.
E_g^i	intrisic bandgap.
$E_g^{N(P)}$	bandgap in n- (p-) type region.
$E_i^{N(P)}$	intrinsic Fermi level for n- (p-) type semiconductor.
E_t	activation energy of the trap.
e	reduced energy.
e_n^t	electron thermal emission rate.
g	degeneracy factor of the defect level.
k	Boltzmann constant.
$K_{sn(p)}$	dopant density-dependent dielectric constant in n- (p-) type semiconductor.
$L_{D(DH)}$	Debye length in nondegenerate (degenerate) case.
L_g	inverse of reduced bandgap gradient in the transition region of a heavily-doped graded pn junction.
n_i	intrinsic carrier density (cm^{-3}).

n	electron density (cm^{-3}).
$n_{ie}^{N(P)}$	effective intrinsic carrier density in n- (p-) region (cm^{-3}).
$N_{A(D)}$	acceptor (donor) density (cm^{-3}).
N_B	background dopant density (cm^{-3}).
$N_{c(v)}$	effective density of conduction (valence) band states (cm^{-3}).
N_0	critical concentration of dopant density-dependent dielectric constant.
N_t	trap density.
$N_{xn(p)}$	net donor (acceptor) density.
n^*	ideality factor.
p	hole density (cm^{-3}).
T	absolute temperature.
V_a	applied voltage.
$\langle v \rangle$	carrier thermal velocity.
$x_{d(L)}^H$	depletion layer width for a heavily-doped abrupt (linearly-graded) junction.
$x_{dA(G)}$	depletion layer width for a heavily-doped abrupt (graded) heterojunction.
$x_{n(L)}^H$	space charge region edge at n-side of a heavily-doped abrupt (linearly-graded) junction.
$x_{p(L)}^H$	space charge region edge at p-side of a heavily-doped abrupt (linearly-graded) junction.
χ	electron affinity.
β	d. c. current gain.
$\eta_{n(p)}$	reduced Fermi energy in n- (p-) type semiconductor.
ρ	charge density.
$\sigma_{n(p)}$	thermal capture cross section for electrons (holes).

ϕ_{bi}^{G}	built-in potential for a heavily-doped graded pn junction.
ϕ_{bi}^{H}	built-in potential for a heavily doped pn junction.
ϕ_{D}	total built-in potential for a heavily-doped abrupt heterojunction.
$\phi_{DN(P)}$	built-in potential on the N- (P-) side for a heavily-doped abrupt heterojunction.
ϕ_{g}^{H}	gradient voltage for a linearly-graded p-n junction.
$\phi_{n(p)}$	potential at quasi-neutral n- (p-) region.
$\phi_{n(p)}^{*}$	Fermi-potential at quasi-neutral n- (p-) region.
ε_{o}	permitivity in vacuum.
ε_{s}	permitivity in semiconductor with a constant value.
$\varepsilon_{sn(p)}$	permitivity in n- (p-) type semiconductor.
τ_{e}	effective carrier lifetime in the space charge region.
$\tau_{n(p)}$	lifetime of electrons (holes).

Abstract of Dissertation Presented to the Graduate Council
of the University of Florida in Partial Fulfillment
of the Requirements for the Degree of Doctor of Philosophy

EFFECTS OF HEAVY DOPING AND METALLIC CONTAMINATION ON ELECTRICAL CHARACTERISTICS OF SEMICONDUCTOR DEVICES

By

Ker-Wen Teng

December 1984

Chairman: Sheng-San Li
Major Department: Electrical Engineering

A theoretical analysis of the effects of increasing the density of shallow impurity dopants on semiconductor devices and an experimental study of the metallic contamination on electrical characteristics of silicon devices have been presented in this dissertation. Numerical calculations of the heavy doping effects such as carrier degeneracy, bandgap narrowing, and dopant density-dependent dielectric constant have been carried out in degenerate semiconductors by employing the empirical models reported in earlier research. The results show that the increasing shallow impurity density will have significant effects on the junction built-in potential and the I-V characteristics of a heavily-doped PN junction diode, heterojunction diode, E-JFETs, and E-MESFETs.

The results from the current-voltage (I-V), capacitance voltage, thermally stimulated capacitance (TSCAP), and the Deep Level Transient Spectroscopy (DLTS) measurements show that the metallic contaminants presented in the silicon devices will introduce several deep-level hole and electron traps. Experimental evidence shows that the metallic contamination will influence the temperature and frequency dependence of the high frequency MOS capacitor C-V behavior. In addition, the reverse leakage current and 1/f noise were found closely related to the density of deep level traps introduced by the metallic contamination in the silicon JFET devices studied. The results presented in this dissertation will help obtain a better understanding of the effects of heavy doping and metallic contamination on the electrical characteristics of semiconductor devices.

CHAPTER I
INTRODUCTION

The advancement of semiconductor material technology has made possible the development of new semiconductor devices and integrated circuits (IC) during the past three decades. As a result, there is a remarkable evolution of semiconductor devices from the early discrete components to the very large scale integrated circuits (VLSI) and very high speed integrated circuits (VHSIC) at the present time.

Shallow impurity dopants are intentionally added into a semiconductor via thermal diffusion or ion implantation process in order to supply conduction electrons or holes for semiconductor devices. Thus, the density of doped impurities will significantly affect the electrical characteristics of semiconductor devices. Occasionally, a semiconductor is found to be contaminated with unexpected impurities which cause the failure of device operation. These unexpected impurities are brought into a semiconductor device during the fabrication processes of an integrated circuit, where the processes become so complex in the modern semiconductor technology in which numerous processing steps were used during each IC fabrication.

In the design and fabrication of a high speed, low power, VLSI or VHSIC, it is necessary to increase the density of shallow impurity dopants in order to reduce the size, the parasitic capacitance, and the parasitic resistance of active devices in the circuits. In addition, even a small amount of contaminated impurities inside a semiconductor will significantly affect the electrical performance of active devices and reduce the IC yield.

The main objectives of this research are (1) to develop theoretical models for heavily doped semiconductor devices (e.g., pn diodes, heterojunctions, transistors, FETS . . .) taking into account the heavy doping effects such as carrier degeneracy, band gap narrowing, and dopant density dependent dielectric constant; (2) to theoretically analyze the effects of heavy doping on the semiconductor device characteristics, and (3) to perform experimental study of the effects of metallic contamination on the device characteristics.

A detailed theoretical study of the effects of increasing the density of shallow impurity dopants on semiconductor devices and an experimental study of the metallic contamination on device characteristics have been carried out in this disseration; these include:

(1) Expressions for the Debye length, built-in potential and depletion layer width of a heavily-doped pn junction diode as well as a heterojunction diode are reformulated. The heavy doping effects such as carrier degeneracy, bandgap narrowing, and dopant density-dependent dielectric constant are accounted for by using the expression for Fermi-energy given by [1], and bandgap narrowing model proposed by [2], as well as the dopant density dependent dielectric constant given by [3].

(2) Theory for a heavily-doped pn junction is modified by treating it as an anisotype graded heterojunction and considering the bandgap narrowing effect. This effect will reduce the bandgap of a heavily-doped semiconductor and result in the bandgap difference between p- and n-region. Thus, the theory for an anisotype graded heterojunction can be modified to describe the electrical behavior of a heavily-doped pn junction assuming a transition region from one side to the other. This transition region extends beyond the space-charge region, and takes place over a large distance as compared to interatomic distances.

(3) Computer analysis of the effects of heavy doping on various semiconductor devices such as pn diode, heterojunction, metal-semiconductor field-effect transistor (MESFET), and junction field-effect transistor (JFET) are performed using the theoretical models presented in this dissertation.

(4) The effects of metallic contamination on the electrical characteristics of silicon devices are experimentally studied. The experimental tools employed in this study include the current voltage (I-V), capacitance voltage (C-V), thermally stimulated capacitance (TSCAP) and deep level transient spectroscoopy (DLTS) measurements. From these measurements, one can determine the energy levels, density of defects, defect profile, and the capture cross-section for each trap level. These trap levels are introduced into the forbidden bandgap of semiconductor by the contaminated

impurities. Thus, it provides us with means of identifying the unknown impurities. In addition, we can study the correlations between the densities of metallic contaminants and the electrical characteristics of devices.

Study of the effects of heavy doping on the built-in potential, Debye length, depletion layer width, and depletion capacitance in a heavily-doped abrupt or linearly graded pn junction diode are described in Chapter II. The effects of heavy doping on the Einstein relationship for both majority and minority carriers in a semiconductor are theoretically analyzed in Chapter III. The theory for current-voltage relationship of a heavily-doped pn diode is proposed in Chapter IV, in which the diode is treated as a device with a linearly varying bandgap across the transition region.

In Chapter V, the effects of the heavy doping on the built-in potential, depletion layer width, and depletion capacitance in a heavily doped abrupt or graded heterojunction are depicted. Calculations are also performed for a AlGaAs-GaAs heterojunction diode using the expressions derived in this chapter.

Chapter VI deals with the effects of heavy doping on current-voltage characterisitcs of a heavily-doped JFET and MESFET device, computer calculations are carried out for a typical GaAs JFET and MESFET with channel doping up to 5×10^{18} cm^{-3}.

The experimental methods employed for studying the effects of metallic contamination on the device performance are described in Chapter VII. Chapter VIII presents the experimental results. A summary and coclusions are given in Chapter IX. Suggestion for future research are also included.

CHAPTER II
EFFECTS OF HEAVY DOPING ON THE BUILT-IN POTENTIAL, DEBYE LENGTH, DEPLETION LAYER WIDTH, AND DEPLETION CAPACITANCE IN A HEAVILY-DOPED PN JUNCTION DIODE

2.1 Introduction

Since heavy doping effects play an important role in the performance of semiconductor devices containing heavily-doped pn junctions, many experimental and theoretical studies [1-7] have been reported on determining the impurity density-dependent dielectric constant [4], bandgap narrowing [5-7] and analytical modeling of these effects. For example, Castner et al. [4] observed a donor density dependent dielectric constant from capacitance measurement on heavily-doped n-type silicon. Andrews et al. [3] proposed an analytical model to account for the effect of impurity density-dependent dielectric constant on the electric field and charge density in a graded n^+-p junction. Dumke [5] determined the bandgap narrowing in the heavily-doped n-type silicon from luminescence measurements, and confirmed that the density of states in the shifted bandedge states for degenerate silicon may still be approximated by using parabolic density of states without introducing significant errors. However, there are no reports on extension of the non-degenerate pn junction theory to account for the heavy doping effects such as carrier degeneracy, impurity density-dependent dielectric constant, and bandgap narrowing on the Debye length, built-in potential, the depletion layer width and depletion capacitance of a heavily-doped pn junction diode.

The purpose of this chapter is to analyze the effects of heavy doping on the built-in potential, Debye length, depletion layer width, and depletion capacitance in a heavily-doped abrupt or linearly graded pn junction diode. Calculations were performed for the p^{++}-n abrupt junction and linearly graded junction using the empirical approximation for the reduced Fermi-energy given by [1], the empirical model for the dopant density-dependent dielectric constant K_{sn} given by [3], and the bandgap narrowing model proposed by [2]. Details of all these models are described in section 2.2. Section 2.3 deals with theoretical analysis and reformulation of the expressions for the built-in potential, Debye length, depletion layer width, and depletion capacitance for a heavily-doped pn junction diode. Results and discussion are given in section 2.4. Conclusions are given in section 2.5.

2.2 Models for the heavy doping effects

Analysis of the heavy doping effects on diode characteristics of a heavily-doped pn junction was made possible by employing the results reported in [1-3] for the heavy doping effects such as carrier degeneracy, dopant density-dependent dielectric constant and bandgap narrowing. Expressions for calculating the different heavy doping effects are described as follows:

2.2.1 The carrier degeneracy

The effect of carrier degeneracy may be taken into account by tractably using an empirical approximation for the reduced Fermi-energy, η, given by [1]. Thus, the reduced Fermi-energy for electrons and holes in a heavily-doped n- and p-type semiconductor may be approximated by

$$\eta_n = F_{1/2}^{-1}(Y_n) \simeq \ln(Y_n) + F(Y_n) \qquad (2.1)$$

$$\eta_p \simeq \ln(Y_p) + F(Y_p) \qquad (2.2)$$

where

$$F(Y_{n,p}) = Y_{n,p} \cdot [64 + 3.5354 \cdot Y_{n,p} \cdot (1 + \frac{Y_{n,p}^{1/2}}{64})]^{-1/4} \qquad (2.3)$$

and $Y_n = n/N_c$, $Y_p = p/N_v$, $n(p)$ is the electron (hole) density; N_c (N_v) is the effective density of conduction (valence) band states. Values of $F(Y)$ vary from 10^{-3} to 1 for n-type silicon, and 2×10^{-3} to 1.8 for p-type silicon for dopant densities in the range of 1×10^{17} to 1×10^{20} cm^{-3}. Equation (2.3) may generate an error $\Delta\eta$ with several alterations of sign in the range $0 < \eta < 12$, but with peak excursions $|\Delta\eta_{max}| < 10^{-4}$ [8]. The calculated values of $F(Y)$ for electrons and holes based on Eq. (2.3) for silicon are shown in Fig. 2.1. Note that the first term on the r.h.s. of Eqs. (2.1) and (2.2) is the direct result of the nondegenerate statistics which relates the carrier density to the reduced Fermi energy, while the second term, $F(Y_n)$ may be considered as a correction for the Fermi-Dirac statistics for the degenerate case.

2.2.2 The dopant impurity density-dependent dielectric constant

Experimental results [4] show that increase in the static dielectric constnat for Sb, P, and As donors in Si was associated with increase in net ionized donor density, $N_{xn} = N_D - N_A$. The results indicate a possible divergence in the static dielectric constant, K_{sn} at a critical concentration N_o. Typically, $N_o \sim 4 \times 10^{18}$ cm^{-3} for phosphorus and $\sim 7 \times 10^{18}$ cm^{-3} for arsenic. For example, the dielectric constant for N-type Si at room temperature can be written as [3]

$$K_{sn} = \begin{cases} 11.7 , & \text{for } n < 10^{16} \text{ cm}^{-3} \\ A_n \exp(B_n N_{xn}) , & \text{for } n > 10^{16} \text{ cm}^{-3} \end{cases} \tag{2.4}$$

By using $K_{sn} = K_m$ at $N_{xn} = N_o$, and $K_{sn} = 11.7$ at $N_{xn} = 10^{16}$ cm^{-3}, we obtain

$$A_n = 11.7 \, (k_m/11.7)^{-K_o} \tag{2.5}$$

$$B_n = K_o \cdot 10^{-16} \cdot \ell n(k_m/11.7) \tag{2.6}$$

The value of K_m, which determines the rate of increase in $K_{sn}(n)$ with dopant density, was chosen as 50. Values of K_o are equal to 0.002506 and 0.001429 for P and As doped Si, respectively. The model given by Eq. (2.4) is sufficient to show trends and its consistency with the experimental data reported by [4], in which values of K_{sn} are varied from 11.7 to 72 for phosphorus doped Si and 11.7 to 33 for As doped silicon for dopant densities in the range of 10^{17} - 5 x 10^{18} cm^{-3}, respectively.

2.2.3 The bandgap narrowing

Recently, Berggren and Sernelius [2] have proposed a rigorous theoretical model for bandgap narrowing calculations in heavily-doped many valley semiconductor. They attributed the bandgap narrowing to the free-carrier-impurity interaction, the correlation energy, as well as the random distribution of impurity ions.

The calculated bandgap narrowing values presented in [2] were found in excellent agreement with the bandgap narrowing data determined from the luminescence measurements by Dumke [5] for the heavily-doped Si. Thus, the bandgap narrowing values reported by [2, 5] will be used to estimate its effects on the diode parameters of a heavily-doped pn junction.

We represent the dopant density dependent bangap narrowing for silicon by a five degree polynomial formulation for dopant density, N_D, greater than 10^{17} cm^{-3} [2, 5]:

$$\Delta E_g = A_o + A_1 x + A_2 x^2 + A_3 x^3 + A_4 x^4 + A_5 x^5 \tag{2.7}$$

where $x = \log(N_D/10^{17})$, $A_o = 17$, $A_1 = 15.483244$, $A_2 = 7.1771826$, $A_3 = 0.06657874$, $A_4 = -1.1285211$, and $A_5 = 0.40151523$.

The expressions given by Eqs. (2.1), (2.2), (2.4), and (2.7), which account for the heavy doping effects described above, will be used to compare the values of built-in potential, Debye length, depletion layer width, and depletion capacitance obtained by conventional (nondegenerate) expressions from those predicted by Eqs. (2.1) through (2.7) for the heavily doped pn junction.

2.3 Derivation

2.3.1 Built-in potential

The built-in potential, $\phi_{bi} \equiv \phi_n - \phi_p$ ($\phi_p < 0$), is the total potential change from the quasi-neutral p-type ragion to the quasi-neutral n-type region (as shown in Fig. 2.2); it is a function of the dopant density in each region. From Fig. 2.2, ϕ_n and ϕ_p are the potential at the quasi-neutral edges x_n and $-x_p$, respectively, and may be defined by

$$\phi_n \equiv -(\frac{1}{q} E_i^N - \phi_n^*) \qquad (2.8)$$

$$\phi_p \equiv \frac{1}{q} E_i^P + \phi_p^* \qquad (2.9)$$

where E_i^N (< 0) and E_i^P (< 0) denote the intrinsic Fermi level for n- and p-type semiconductor, respectively, and

$$\phi_n^* \equiv \frac{1}{q} (E_f - E_c^N) = \frac{kT}{q} \eta_n \qquad (2.10)$$

$$\phi_p^* \equiv - \frac{1}{q} (E_f - E_v^P) = - \frac{kT}{q} \eta_p \qquad (2.11)$$

where E_v^P and E_c^N are the valence and conduction band edges in the quasi-neutral p- and n-type regions, respectively. Thus, we may obtain the modified built-in potential, ϕ_{bi}^H, for a heavily-doped pn junction as

$$\phi_{bi}^{H} \equiv \phi_n - \phi_p = (\phi_n^* - \phi_p^*) + \frac{1}{q} E_g^*$$

$$= (\frac{kT}{q}) \ln (\frac{pn}{N_V N_C}) + \frac{kT}{q} [F(Y_n) + F(Y_p)] + \frac{1}{q} E_g^* \qquad (2.12)$$

and

$$E_g^* = E_g^i - \frac{1}{2} (\Delta E_g^N + \Delta E_g^P) \qquad (2.13)$$

where E_g^i is the intrinsic bandgap, ΔE_g^N and ΔE_g^P are the bandgap narrowing in the n- and p- type material, respectively.

2.3.2 Debye length

In order to investigate the validity of the depletion approximation for a heavily-doped abrupt junction, we study the effects of heavy doping on the extrinsic Debye length by using the standard procedures described elsewhere [9].

If we consider a uniformly doped p^{++}-n^{+} junction with the space charge region edges at $-x_p$ and x_n, assuming only small variations of potential from ϕ_n^* near $x = x_n$ and neglecting the minority carrier concentration, p, with $\phi' = \phi_n^* - \phi$, we may then write the Poisson's equation in the form

$$\frac{d^2\phi}{dx^2} = \frac{q}{\varepsilon_{sn}} (N_D - n) = \frac{q}{\varepsilon_{sn}} [N_D - N_C F_{1/2}(\frac{q}{kT}(\phi_n^* - \phi'))]$$

$$= \frac{q}{\varepsilon_{sn}} \cdot N_D \cdot [1 - \frac{F_{1/2}(\frac{q}{kT}(\phi_n^* - \phi'))}{F_{1/2}(\frac{q}{kT}(\phi_n^*))} \qquad (2.14)$$

where $F_{1/2}$ is the Fermi-Dirac integral of order one-half, and ε_{sn} (= $K_{sn} \cdot \varepsilon_0$) is the permitivity of the seimconductor; ε_0 is the permitivity in vacuum, and K_{sn} is the dopant density-dependent dielectric constant given by Eq. (2.4). We may expand $F_{1/2}\,[\frac{q}{kT}\,(\phi_n^* - \phi')]$ in Eq. (2.14) in a Taylor series, and retain only the first two terms, which yields

$$\frac{d^2\phi}{dx^2} \simeq \frac{q}{\varepsilon_{sn}} \cdot N_D \cdot \frac{q}{kT}\,\frac{F_{-1/2}(\frac{q}{kT}\,\phi_n^*)}{F_{1/2}(\frac{q}{kT}\,\phi_n^*)}\,\phi' = \frac{\phi'}{L_{DH}^2} \qquad (2.15)$$

where L_{DH} is the modified extrinsic Debye length for a heavily-doped abrupt pn junction, and is given by

$$L_{DH} = [\frac{\varepsilon_{sn}kT}{q^2N_D}\,\frac{F_{1/2}(\eta_n)}{F_{-1/2}(\eta_n)}]^{1/2} = L_D[\frac{F_{1/2}(\eta_n)}{F_{-1/2}(\eta_n)}]^{1/2} \qquad (2.16)$$

where L_D is the Debye length for the nondegenerate case. It is noted that Eq. (2.16) will reduce to the coventional expression as dopant density approaching nondegenerate regime. Landsberg [13] has also reported similar results, but without including the effect of dopant impurity density-dependent dielectric constant. Thus, it is obvious that both dopant density-dependent dielectric constant and carrier degeneracy will have significant effects on the extrinsic Debye length.

2.3.3 Depletion layer width and depletion capacitance

The depletion layer width and depletion capacitance are two important parameters for the design and modeling of a semiconductor device. Since the dielectric constant is a function of dopant impurity density, it will obviously affect the depletion layer width and depletion capacitance of a heavily-doped abrupt junction, as well as a linearly graded junction, and result in a change of depletion layer width and depletion capacitance from that given by the nondegenerate case. We shall first deal with a uniformly doped p^{++}-n^{+} abrupt junction (as shown in Fig. 2.3). If ε_{sn} $(= K_{sn} \cdot \varepsilon_0)$ and ε_{sp} $(= K_{sp} \cdot \varepsilon_0)$ are the permitivity in the n- and p-type regions, respectively, and K_{sn} and K_{sp} are a function of dopant impurity density, then we may write

$$E(x) = \frac{-qN_D}{\varepsilon_{sn}} (x_n^H - x) , \quad 0 < x < x_n^H$$

$$E(x) = \frac{-qN_A}{\varepsilon_{sp}} (x + x_p^H) , \quad -x_p^H < x < 0 \tag{2.17}$$

Thus, the potential is given by

$$\phi(x) = \phi_n - \frac{qN_D}{2\varepsilon_o K_{sn}} (x_n^H - x)^2 , \quad 0 < x < x_n^H$$

$$\phi(x) = \phi_p + \frac{qN_A}{2\varepsilon_o K_{sp}} (x + x_p^H)^2 , \quad -x_p^H < x < 0 \tag{2.18}$$

for the abrupt junction, with $N_A \cdot x_p^H = N_D \cdot x_n^H$, the depletion layer width for a heavily-doped abrupt junction can be expressed by

$$x_d = x_n^H + x_p^H$$

$$= \left[\frac{2\varepsilon_o}{q} \frac{\phi_{bi}^H}{\frac{N_A}{K_{sn}} + \frac{N_D}{K_{sp}}}\right]^{1/2} \cdot \left[\left(\frac{N_A}{N_D}\right)^{1/2} + \left(\frac{N_D}{N_A}\right)^{1/2}\right] \tag{2.19}$$

Since the depletion layer width is dominated by the lightly-doped region, we may write the depletion layer width for the heavily-doped abrupt junction as a function of applied voltage by including the effect of two majority-carrier distribution tails [10] and replacing the modified built-in potential ϕ_{bi}^H in Eq. (2.19) by $(\phi_{bi}^H - V_a - \frac{2kT}{q})$ so that

$$x_d^H = \left[\frac{2\varepsilon_o}{q} \cdot \frac{(\phi_{bi}^H - V_a - \frac{2kT}{q})}{(N_A/K_{sn} + N_D/K_{sp})}\right]^{1/2} \cdot \left[\left(\frac{N_A}{N_D}\right)^{1/2} + \left(\frac{N_D}{N_A}\right)^{1/2}\right] \tag{2.20}$$

The depletion capacitance per unit area for a heavily-doped abrupt junction is given by

$$C_{jA} = \frac{dQ}{dV_a} = N_D^{1/2} N_A^{1/2} \cdot \left(\frac{q\varepsilon_o}{2 \cdot (N_A/K_{sn} + N_D/K_{sp}) \cdot (\phi_{bi}^H - V_a - \frac{2kT}{q})}\right)^{1/2}$$

$$= \varepsilon_{snp}/x_d^H \tag{2.21}$$

where

$$\varepsilon_{snp} = \frac{\varepsilon_o(N_A + N_D)}{(N_A/K_{sn} + N_D/K_{sp})} \tag{2.22}$$

which shows that dielectric constant in the heavily-doped n- and p-type regions depends on dopant impurity density instead of a constant $\varepsilon_s = 11.7$. The depletion capacitance for the heavily doped case may be obtained from Eq. (2.21), which is also dopant density dependent.

Similar calculations may be performed for the case of a heavily-doped linearly graded junction with $N_D - N_A = ax$, where "a" is the net doping concentration gradient. Detailed mathematical derivation of the depletion layer width x_{dL}^H and the built-in potential, ϕ_{bi}^H, in a heavily-doped linearly-graded junction taking into account the heavy doping effects are described in the Appendix. It can be shown that from Eq. (A-10)

$$\begin{aligned}\phi_{bi}^H &\equiv \phi_n - \phi_p \\ &= \frac{qa}{2\varepsilon_o}\left\{\frac{1}{A}\left[-\frac{1}{4C_n}(x_{dL}^H)^2 + \frac{1}{C_n^2}e^{\frac{1}{2}C_n x_{dL}^H}\cdot x_{dL}^H - \frac{2}{C_n^3}\cdot\left(e^{\frac{1}{2}C_n x_{dL}^H} - 1\right)\right]\right. \\ &\qquad \left. - \frac{1}{A_p}\left[-\frac{1}{4C_p}(x_{dL}^H)^2 + \frac{1}{C_p^2}e^{-\frac{1}{2}C_p x_{dL}^H}\cdot x_{dL}^H - \frac{2}{C_p^3}\left(e^{-\frac{1}{2}C_p x_{dL}^H} - 1\right)\right]\right\}\end{aligned} \tag{2.23}$$

where a is the gradient of net doping concentration, A_n (A_p) is the constant of K_{sn} (K_{sp}), repsectively, and $C_n = -B_n a$, $C_p = B_p a$ are the parameters characterized only by junction properties such as the dopant impurity density and the net dopant concentration gradient, a. It is noted that the depletion layer width, x_{dL}^H, may be expressed as a function of applied voltage with $\varepsilon_s = 11.7$ (i.e., without taking into account the effect of dopant density-dependent dielectric constant) by

$$x_{dL}^{H} = x_{pL}^{H} + x_{nL}^{H} = \left[\frac{12 \cdot \varepsilon_s(\phi_{bi}^{H} - V_a)}{qa}\right]^{1/3} \tag{2.24}$$

Thus, the depletion capacitance for a heavily-doped linearly graded pn junction with $\varepsilon_s = 11.7$ is given by [11]

$$C_{jL}^{H} = \left[\frac{q\varepsilon_s^2 a}{12(\phi_g^H - V_a)}\right]^{1/3} \tag{2.25}$$

where the gradient voltage [12] for the heavily-doped linearly graded junction is given by

$$\phi_g^H = \frac{2}{3}\left(\frac{kT}{q}\right) \ell n \left[\frac{a^2\varepsilon_s kT/q}{8q(n_{ie}^N n_{ie}^P)^{3/2}}\right] \tag{2.26}$$

and the effective intrinsic density n_{ie}^N and n_{ie}^P in the n- and p-regions are given respectively by:

$$n_{ie}^N = [n_i^2 \exp(\Delta E_g^P/kT)F_{1/2}(\eta_n) \exp(-\eta_n)]^{1/2} \tag{2.27}$$

$$n_{ie}^P = [n_i^2 \exp(\Delta E_g^N/kT)F_{1/2}(\eta_p) \exp(-\eta_p)]^{1/2} \tag{2.28}$$

where n_i is the intrinsic carrier denisty.

In order to determine the depletion layer width in a heavily-doped linearly graded junction, we need to choose a suitable trial value of x_{dL}^H, and then use iteration procedures on Eqs. (2.12), (2.23) or (2.24) with a known net dopant concentration gradient, a. The exact value of x_{dL}^H can then be obtained.

2.4 Results and Discussion

Calculations of the effects of heavy doping on the built-in potential, Debye length, depletion layer width, and depletion capacitance for a heavily-doped pn junction were carried out by using the expressions derived in section 2.1. Figure 2.4 shows the calculated built-in potential vs. background doping density, N_B, for a p^{++}-n (or n^{++}-p) abrupt junction. The doping density of p^{++} (or n^{++}) side is assumed to be 1×10^{20} cm^{-3}, and N_B is the impurity concentration on the lightly-doped side. From Fig. 2.4, it is shown that the modified built-in potential, x_{bi}^{H}, calculated from Eq. (2.12), is about 50 to 75 mV smaller than those calculated from the conventional expression. Thus, the heavy doping effects such as carrier degeneracy and bandgap narrowing have a significant influence on the value of built-in potential of a heavily doped abrupt pn junction.

The result for the Debye length, depletion layer width and depletion capacitance of a p^{++}-n abrupt junction are shown in Fig. 2.5, 2.6 and 2.7, respectively, in which the doping density of the p^{++} side is assumed to be 1×10^{20} cm^{-3}. From Fig. 2.5, it is clearly shown that the effects of carrier degeneracy and dopant density-dependent dielectric constant have considerable influence on the Debye length. The effect of dopant density-dependent dielectric constant on the Debye length is clearly shown in Table 2.1. Figure 2.6 and 2.7 show the depletion layer width and depletion capacitance calculated from Eqs. (2.20) and (2.21), with and without including the effect of dopant density-dependent dielectric constant. The results shows that the effects of carrier degeneracy and bandgap narrowing have little influence on the depletion layer width and depletion capacitance. On the other hand, the result shows that the dopant density dependent dielectric constant is the only heavy doping effect which will have a strong infuence on these two parameters. Table 2.1 shows the calculated results of L_D and x_n at $N_B = 5 \times 10^{18}$ cm^{-3}. Thus, the depletion approximation is still valid up to this dopant density.

Fig. 2.8 shows the gradient voltage calculated from Eq. (2.26) for a heavily-doped linearly-graded junction, where dielectric constant $\varepsilon_s = 11.7$ is used. Thus, the change in the gradient voltage shown in Fig. 2.8 may be attributed to the effects of bandgap narrowing and carrier degeneracy. The results of depletion layer width and depletion capacitance for a heavily-doped linearly-graded junction calculated from Eqs. (2.24) and (2.25) are shown in Fig. 2.9, where dielectric constant $\varepsilon_s = 11.7$ is used. From Fig. 2.9 it is clearly shown that carrier degeneracy and bandgap narrowing have little effect on the depletion layer width and depletion capacitance. The results show little difference from those predicted by the nondegenerate expressions.

From the results shown above, it is clear that the doping density-dependent dielectric constant is important in the heavy doping regime. For an isotropic semiconductor, the dielectric constant depends on the properties of atoms and the manner in which the atoms are assembled to form a crystal (through the effect of local E-field). Clausisus-Mossotti relation [4] can relate the dielectric constant to electronic polarizability, which is resulted from the displacement of electron shell (or cloud) relative to the atom nucleus. Since the high extrinsic impurity concentration and the nonuniform distribution of these impurities will probably affect the local E-field and alter the displacement between nucleus and electron shell, the heavily-doped semiconductor dielectric constant is also expected to be changed. Further experimental investigation on the dielectric constant anomaly is needed.

2.5 Summary and Conclusions

A theoretical analysis of the heavy doping effects on the built-in potential, depletion layer width, Debye length, and depletion capacitance for a heavily-doped pn junction has been presented in this chapter. Numerical calculations of the heavy doping effects such as carrier degeneracy, dopant density-dependent dielectric constant, and bandgap narrowing were carried out by employing the empirical models described in section 2.2. The results of present studies show that 1) bandgap narrowing and carrier degeneracy have important effects on the junction built-in potential; 2) carrier degeneracy and dopant impurity density-dependent dielectric constant have a significant influence on the Debye length for the abrupt junction case, and 3) the dopant impurity density-dependent dielectric constant is the only heavy doping effect which will have a strong influence on the depletion layer width and depletion capacitance. The present results showed that the new calculated values for the Debye length, built-in potential, and depletion capacitance may differ significantly from those predicted by the nondegenerate theories.

TABLE 2.1

A comparison of the calculated diode parameters for a heavily-doped p^{++}-n diode with and without including the heavy doping effects.

*Physical Parameters	Nondegnerate ε_s = constant	Degenerate ε_s = constant	Degenerate As-doped Si $\varepsilon_s(N_D)$	Degenerate P-doped Si $\varepsilon_s(N_D)$
L_D(Å)	18	25	45	63
X_d(Å)	164	160	280	420
x_n(Å)	156	152	267	400

* $p^{++} = 1.0 \times 10^{20}$ cm^{-3}, n = 5×10^{18} cm^{-3}.

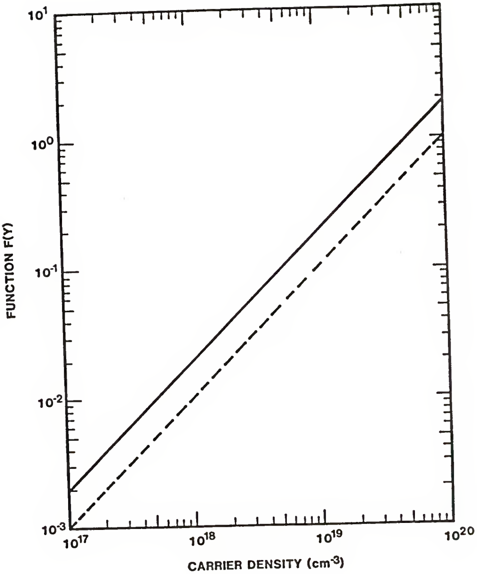

Figure 2.1 Values of function F(Y) vs hole or electron density in the heavily-doped Si at T = 300 k. Where F(Y) is calculated from Eq.(2.3). Solid line is values for electrons, dash line for holes.

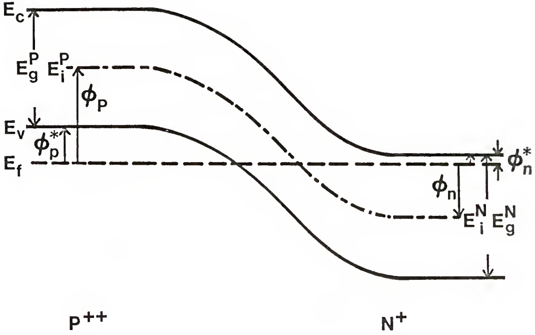

Figure 2.2 Energy band diagram for a heavily-doped p^{++}-n^+ junction diode.

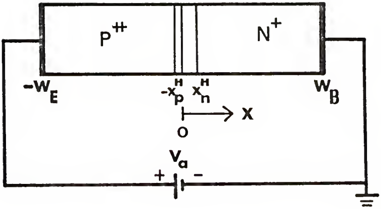

Figure 2.3 Schematic diagram for a heavily-doped p^{++}-n^{+} junction diode used in this study.

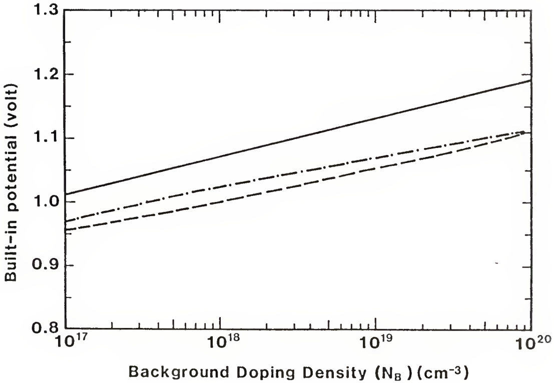

Figure 2.4 Built-in potential vs. background doping density, N_B, for a heavily-doped silicon abrupt pn junction at T = 300 K. Where, the doping dnesity of p^{++}(or N^{++}) side is assumed to be 1 x 10^{20} cm^{-3}, and N_B is for the dopant impurity concentration in the lightly-doped side. Solid line is the predicted values by the conventional theory for a p^{++}-n junction, dash line and dash-dot line are calculated by using Eq. (2.12) for the n^{++}-p and p^{++}-n abrupt junction diode.

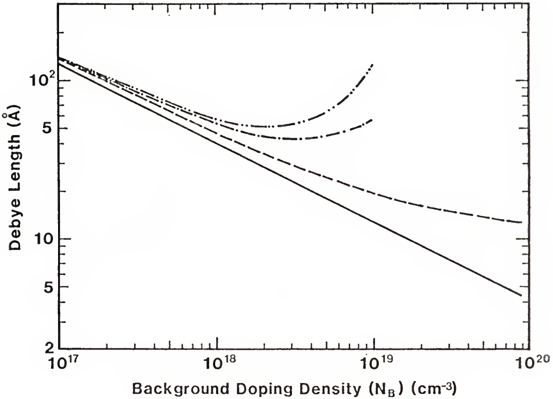

Figure 2.5 The Debye length vs. background dopant density, N_B, for a heavily-doped p^{++}-n^+ Si abrupt junction at T = 300 K. Solid line is the conventionally predicted values, dash line is calculated from Eq. (2.16), using dielectric constant (= 11.7), while dot-dash line and double dot-dash line are calculated from Eq. (2.16) using dopant impurity density-dependent dielectric constant for the As- and P-doped Si.

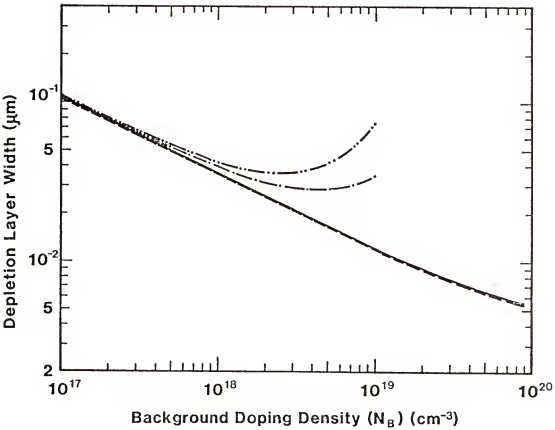

Figure 2.6 Depletion layer width vs. background dopant density, N_B, for a heavily-doped p^{++}-n^{+} Si abrupt junction at $V_a = 0$ and T = 300 K. Solid line is the conventional predicted values; dash line is calculated from Eq. (2.20) with dielectric constant (= 11.7). While, dash-dot and double dot-dash lines are obtained from Eq. (2.20) using dopant impurity-density-dependent dielectric constant for the As- and P-doped Si, respectively.

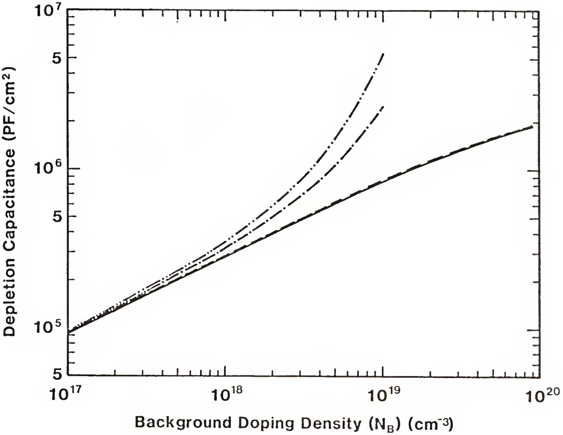

Figure 2.7 Depletion capacitance vs. background dopant density, N_B, for a heavily-doped p^{++}-n^{+} Si abrupt junction at $V_a = 0$ and T = 300 K. Solid line is the conventionally predicted values; dash line is calculated from Eq. (2.21) with dielectric constant equql to 11.7. While dash-dot and double dot-dash lines are obtained from Eq.(2.21) using dopant impurity density-dependent dielectric constant for the As- and P-doped Si, respectively.

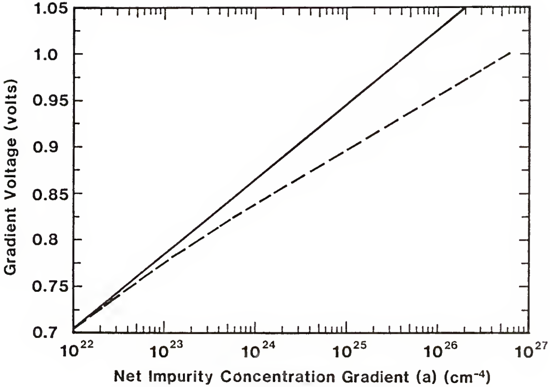

Figure 2.8 Graident voltage vs. net impurity concentration gradient, a, for a heavily-doped Si linearly graded junction at $V_a = 0$ and $T = 300$ K. Solid line is the conventionally predicted values, dash line is calculated from Eq. (2.26) with dielectric constant equql to 11.7.

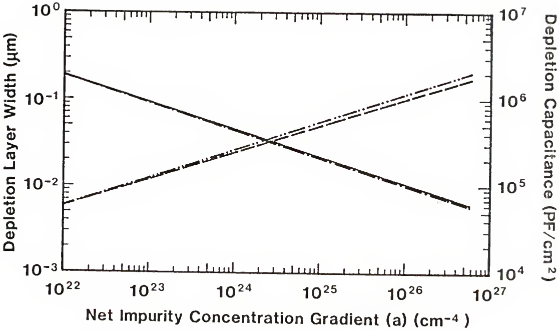

Figure 2.9 Depletion layer width and depletion capacitance vs. net impurity concentration graident, a, for a heavily -doped linearly graded Si pn junction diode at $V_a = 0$ and T = 300 K. Solid line and dash lines are the conventionally predicted depletion layer width and depletion capacitance, respectively; dash-dot line and double dot-dash lines are the values of depletion layer width and depletion capacitance calculated from Eqs. (2.24) and (2.25) using dielectric constant equal to 11.7.

CHAPTER III
EFFECTS OF HEAVY DOPING ON THE EINSTEIN RELATION

3.1 Introduction

Studies of the effect of carrier degeneracy on Einstein relation for the majority carriers [13-15], as well as the effect of bandgap narrowing on the effective intrinsic density [16] and the minority carrier diffusivity [17] in the heavily-doped silicon have been reported by many investigators. The reason for this may be attributed to the poor agreement between the experimental data and the theoretical prediction on the transport parameters in the heavily doped regime, and lack of understanding of the physics underlying the basic mechanisms of heavy doping effects in the degenerate semiconductors. Most of the previous research efforts, however, have been focused on heavy doping effects in the degenerate silicon due to its importance in the IC applications.

Measurements of the minority hole diffusivity [18-22] and the drift mobility [23] have been reported recently for heavily-doped n-type silicon. Although large discrepancies still exist among these reported values for the minority hole diffusivity, the results indicate that values of the minority hole diffusivity tend to saturate for dopant density exceeding 10^{19} cm^{-3} as is shown in Fig. 3.1.

Determination of the minority hole diffusivity in the heavily-doped n-type silicon is usually carried out by using the Einstein relation (i.e., $D_p/\mu_p = kT/q$) assuming that the majority and minority hole mobilities are equal in the heavy doping regime [16,24]. However, recent theoretical calculations [25], and experimental observations [22,23] show that the values of minority hole mobility are considerably lower than that of majority hole mobility in the p-type silicon for the corresponding dopant density. In addition, it is very important to investigate how the effect of bandgap narrowing will affect the Einstein relation for majority carriers and minority carriers.

3.2 Theoretical analysis

3.2.1 Einstein relation for majority carriers

The effects of carrier degeneracy on Einstein relation for majority carriers in a degenerate semiconductor have been studied by employing parabolic density of states and rigid band approximation. These studies proved that the generalized Einstein relation for an n-type degenerate semiconductor may be written as

$$\frac{D_n}{\mu_n} = (\frac{kT}{q})[n/(dn/d\eta_c)]$$

$$= (\frac{kT}{q})[F_{1/2}(\eta_c)/F_{-1/2}(\eta_c)] \quad (3.1)$$

Fig. 3.2 and 3.3 show the D_p/μ_p and D_n/μ_n ratio vs. carrier density for a p- and n-type degenerate silicon, respectively, calculated from Eq. (3.1) for temperatures from 100-400 K. However, the electron density in a degenerate semiconductor can be expressed by

$$n = N_cF_{1/2}(\eta_c) = N_c \frac{1}{\Gamma(3/2)} \int_0^\infty \frac{e^{1/2}}{1 + \exp(e - \eta_c)} \cdot de$$

$$= N_c \frac{1}{\Gamma(3/2)} \int_{e_c}^\infty \frac{(e' - e_c)^{1/2}}{1 + \exp[(e' - e_c) - \eta_c]} \cdot de' \qquad (3.2)$$

where $e = E/kT$ is the reduced energy, $e_c = E_c/kT$ is the reduced conduction band edge, and for a heavily-doped semiconductor, $E_c = E_c^i - \Delta E_g(N)$. $\Delta E_g(N)$ is the bandgap narrowing and depends on the carrier density. Since e_c is an implicit function of reduced Fermi energy, η_c, the mathematical derivation

$$\frac{dn}{d\eta_c} = N_cF_{-1/2}(\eta_c) \qquad (3.3)$$

needs to be carefully examined when the bandgap narrowing effect is considered.

By using Leibnitz's rule for differentiation of integrals, we may write

$$\frac{dn}{d\eta_c} = \int_{e_c(n)}^\infty \frac{d}{d\eta_c} \left\{\frac{[e' - e_c(n)]^{1/2}}{[1 + \exp((e' - e_c) - \eta_c)]}\right\} \cdot de'$$

$$= \frac{N_c}{\Gamma(3/2)} \int_{e_c(n)}^\infty \left\{\frac{d}{d\eta_c}\left[\frac{1}{1 + \exp(e' - e_c(n) - \eta_c)}\right] \cdot (e' - e_c(n))^{1/2}\right.$$

$$\left. - [e' - e_c(n)]^{-1/2} \frac{de_c(n)}{d\eta_c}\left[\frac{1}{1 + \exp(e' - e_c - \eta_c]}\right]\right\} \cdot de'$$

(3.4)

After employing integration by parts and steps of manipulation, the integration of first term of Eq. (3.4) can be expressed by

$$\int_{e_c(n)}^{\infty} \frac{d}{d\eta_c}\left[\frac{1}{1 + \exp(e' - e_c(n) - \eta_c)}\right] \cdot (e' - e_c(n))^{1/2} \cdot de'$$

$$= \int_{e_c(n)}^{\infty} \left[1 + \frac{de_c(n)}{d\eta_c}\right] \cdot \left[\frac{\frac{1}{2}(e' - e_c(n))^{-1/2}}{1 + \exp(e' - e_c(n) - \eta_c)}\right] \cdot de' \tag{3.5}$$

Substituting Eq. (3.5) into (3.4), we obtain

$$\frac{dn}{d\eta_c} = \frac{N_c}{\Gamma(3/2)} \frac{1}{2} \int_0^{\infty} \frac{e^{-1/2}}{1 + \exp(e - \eta_c)}\, de$$

$$= N_c F_{-1/2}(\eta_c) \tag{3.6}$$

This proves that the generalized Einstein relation for majority carriers in a heavily-doped semiconductor is still valid if the parabolic density of states and rigid band approximation were assumed.

3.2.2 Einstein relation for minority carriers

It is instructive to study the effect of bandgap narrowing on Einstein relation for minority carriers. The PN products for an n-type degenerate semiconductor is given by

$$pn = n_i^2 \cdot \exp(\Delta E_g/kT) \cdot F_{1/2}(\eta_c) \cdot \exp(-\eta_c)$$

$$\equiv n_{ie}^2 \tag{3.7}$$

where n_i is the intrinsic carrier density; $\eta_c = (E_F - E_c)/kT$ is the reduced Fermi energy; n_{ie} is the effective intrinsic carrier density; and the bandgap narrowing ΔE_g is defined by

$$\Delta E_g = E_g^i - E_g(n) \tag{3.8}$$

where $E_g(n)$ is the perturbed bandgap. With this definition, ΔE_g is a positive quantity, which varies with n. Taking the partial derivative on both sides of Eq. (3.7) with respect to η_c and dividing by pn yields

$$(\frac{dp}{d\eta_c})/p = (dn_{ie}^2/d\eta_c)/n_{ie}^2 - (dn/d\eta_c)/n \tag{3.9}$$

By substituting Eq. (3.6) into Eq. (3.9), we obtain

$$(\frac{dp}{d\eta_c})/p = -[1 - (d\Delta E_g/d\eta_c)(\frac{1}{kT}) \tag{3.10}$$

The generalized Einstein relation for minority holes is given by

$$\frac{D_p}{\mu_p} = (\frac{kT}{q})[p/(dp/d\eta_v)] \tag{3.11}$$

Using the chain rule, we can write

$$\frac{dp}{dn_v} = \left(\frac{dp}{dn_c}\right)\left(\frac{dn_c}{dn_v}\right)$$

$$= \left(\frac{dp}{dn_c}\right)\left[-1 + \left(\frac{d\Delta E_g}{dn_c}\right) \cdot \left(\frac{1}{kT}\right)\right]^{-1} \qquad (3.12)$$

Finally, from Eq. (3.10) to Eq. (3.12), we obtain

$$\frac{D_p}{\mu_p} = \frac{kT}{q} \qquad (3.13)$$

Thus, the Einstein relation for minority carriers in a heavily-doped semiconductor is still valid, if the parabolic density of states and rigid band approximation are assumed.

3.3 Discussion

From the above theoretical analysis, it is clearly shown that the generalized Einstein relation for majroity carriers and minority carriers in a heavily-doped semiconductor are still valid when the parabolic density of states and rigid band approximations are assumed. Physically, with any gradient of majority carriers concentration there will also be a gradient of the bandgap which gives rise to an effective E-field. This E-field must be taken into account in representing the drift current of the minority holes. When this effective field is included, the Einstein relation for the minority carriers is still given by the usual expression, $D_p = (kT/q)\mu_p$. The reasons for the difference between the diffusion constants, say, holes in a heavily-doped p-type semiconductor and as a minority carrier in a heavily-doped n-type semiconductor may be due to a combination of 1) the difference in the distribution that holes would have in both types of semiconductor and 2) the addition of electron-hole scattering for holes as minority carriers.

It is noted that Eq. (3.1) is not valid when considering the impurity band broading and band-tail states [24, 25] instead of employing the parabolid density of states and rigid band approximation. Additional terms should be added in Eq. (3.1), and problems will become more complicated. Further research in this area is needed.

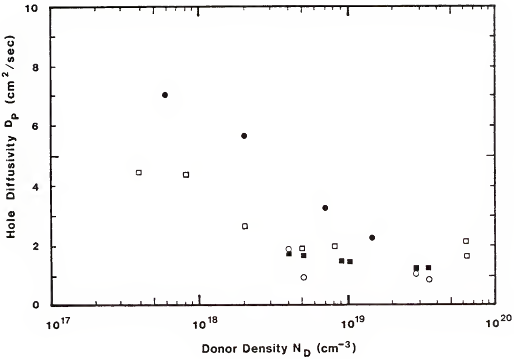

Figure 3.1 Minority hole diffusivity vs. dopant density in n-type Si. Solid dots are the data given by [18], open circles by [19], solid squares by [20], and open squares by [21].

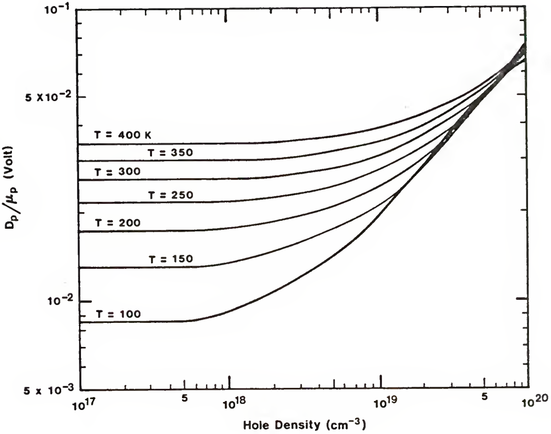

Figure 3.2 Majority hole diffusivity/mobility ratio vs. hole density with temperature as a parameter for p-type Si.

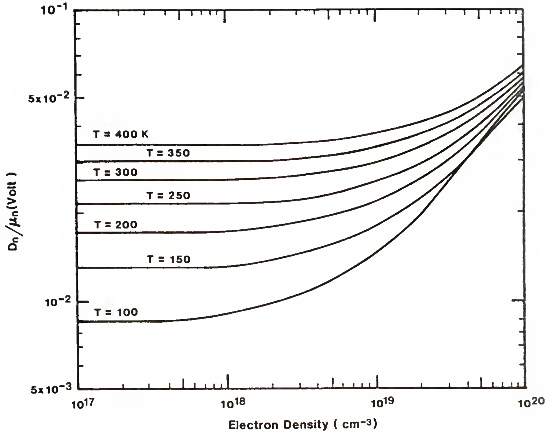

Figure 3.3 Majority electron diffusivity/mobility ratio vs. electron density with temperature as a parameter for n-type silicon.

CHAPTER IV
THEORY OF ELECTRICAL CHARACTERISTICS OF A HEAVILY-DOPED PN DIODE

4.1 Introduction

Bandgap narrowing is one of the fundamental heavy-doping mechanisms that yields a large minority-carrier density, and consequently a large minority-carrier emitter current. Electrical measurements in heavily-doped silicon material and devices indicate that the forbidden energy gap may be smaller than the intrinsic energy gap of pure silicon. These experimental measurements are categorized by [26] as: 1) measurements of the temperature dependence of the current gain in a silicon bipolar transistor [27,28]; 2) measurements of the collector current and its temperature dependence in silicon bipolar transistors [16,29]; 3) measurements of the temperature dependence of the photoresponse of silicon pn junctions and transistors [30]; 4) measurements of the temperature dependence of the emitter current in silicon solar cells (in the dark condition) and bipolar transistors [31]; 5) measurements of the emitter current in different pn jucntion structures [20]; and 6) measurements of the collector current in different pnp bipolar devices with different base width [32].

Rather than providing a direct measurement of the bandgap, the above measurements yield an effective intrinsic carrier density, n_{ie}^2, by employing the conventional current-voltage expression. However, a question arises as to whether the heavy doping effects such as bandgap narrowing, carrier degeneracy, and dopant density-dependent dielectric constant will have a strong influence on the minority-carrier current flow in the device quasi-neutral region, and result in the modification of the nondegenerate pn junction theory. An analysis for the terminal behavior and capacitance of a heavily-doped pn diode is proposed in this Chapter. The expressions for the I-V characteristics and capactance are modified, which include the heavy doping effects. It not only helps the interpretion of the experimental measurements mentioned above, but also suggests means of determining the bandgap narrowing. This research effort will contribute to the understanding of the effects of heavy doping on the carrier transport in a heavily-doped p-n junction diode.

It is well known that the effect of bandgap narrowing is to cause the bandgap shinkage when dopant density is increased in a heavily doped semiconductor. A typical heavily-doped pn junction fabricated by same material will thus display different bandgaps between p- and n-region with smaller bandgap found in the more heavily-doped side. This bandgap difference of a heavily-doped pn junction is similar to that of a typical anisotropic heterojunction diode. However, the p- and n-region in a heavily-doped pn junction still have the same affinities. It gives us a clue to study the effects of heavy doping by modifying the theory of anisotropy of heterojunction diodes [33-35].

In section 4.2, general expressions for electrical potential, carrier density, and built-in potential for a heavily-doped semiconductor device will be derived. Theory for electrical behavior of a heavily-doped graded pn junction diode is then developed. The results of numerical calculations are presented in section 4.3. Section 4.4 shows summary and the conclusions.

4.2 Theoretical treatment

4.2.1 Electrical potential and carrier densities

In this section we cosider a degenerate semiconductor with a dopant concentration that varies with position. When the system is in thermal equilibrium, the electron current and hole current must separately be equal to zero. The total electron current consists of both drift and diffusion components:

$$J_n = q\mu_n n E_x + qD_n \frac{dn}{dx} \tag{4.1}$$

Since $J_n = 0$, we may solve for the electric field E_x in terms of the electron concentration and its gradient

$$\begin{aligned} E_x &= -(D_n/\mu_n)\,\frac{1}{n}\,(dn/dx) = -\frac{kT}{q}\,\frac{n}{dn/d\eta_n}\,\frac{1}{n}\,\frac{dn}{dx} \\ &= -\frac{kT}{q}\,(d\eta_n/dx) \end{aligned} \tag{4.2}$$

Here we have used the generalized Einstein relation for the degenerate semiconductor derived by Landsberg [13]. Since the $F_{1/2}$ (Fermi-Dirac integral of order one-half) for the spherical band in k-space or a parabolic quantum density of states is justified [5,17,36-38], the reduced Fermi energy, η_n, for electrons can be expressed by (see Eq. (2.1)).

$$\eta_n = F^{-1}_{1/2}(Y_n)$$

$$\simeq \ell n(Y_n) + F(Y_n) \qquad (4.3)$$

Eq. (4.3) has an important implication in that it allows us to derive explicit expressions for the excess minority carrier density in a heavily doped p-n diode. This is discussed next.

We may relate the electron density to the electrical potential via Eq. (4.2). Since $E_x = - \frac{d\phi}{dX}$, we have

$$d\phi = \frac{kT}{q} (d\eta_n) \qquad (4.4)$$

at any point in an n-type semiconductor. If we integrate Eq. (4.4) between any two positions--for example, from x_1 to x_2, and through the use of Eq. (4.3), we obtain

$$\phi_{n2} - \phi_{n1} = \frac{kT}{q} (\eta_{n2} - \eta_{n1})$$

$$\simeq \frac{kT}{q} \ell n\ (Y_{n2}/Y_{n1}) + \frac{kT}{q} [F(Y_{n2}) - F(Y_{n1})]$$

$$(4.5)$$

Since $Y_{n2}/Y_{n1} = n_2/n_1$, we can rewrite Eq. (4.5) in exponential form,

$$n_2/n_1 = \exp \left[\frac{q}{kT} (\phi_{n2} - \phi_{n1})\right] \cdot \exp [F(Y_{n1}) - F(Y_{n2})] \qquad (4.6)$$

Note that Eq. (4.6) will reduce to the conventional expression for the nondegenerate case if $F(Y_{n1})$ and $F(Y_{n2})$ are set equal to zero (see Fig. 2.1). A physical interpretation of this result is that ratio of carrier densities at position x_2 and x_1 is related not only to their potential difference but is also influenced by the Fermi-Dirac statistics through the function of F(Y).

Similarly, the ratio of hole densities at positions x_2 and x_1 may be related to the potential ϕ_{p1} and ϕ_{p2} by

$$p_2/p_1 = \exp\left[\frac{q}{kT}(\phi_{p1} - \phi_{p2})\right] \cdot \exp\left[F(Y_{p1}) - F(Y_{p2})\right] \tag{4.7}$$

where $Y_p = p/N_v$; p is the hole density, and N_v is the effective density of the valence band states.

4.2.2 Built-in potential

The expression of built-in potential for a heavily-doped n^+p diode is derived in this section. A heavily-doped graded junction n^+p diode with a transition region modeled to extend beyond the space-charge region is assumed to have a constant bandgap gradient. Variations of the dielectric constant, effective mass, carrier lifetime, and mobility are ignored in this transition region. The junction is said to be graded if the transition from one region to another takes place over a large distance compared to interatomic distances.

Figure 4.1(a) shows the transition region extends from $-X_{ng}$ to X_{pg} and the space charge region is from $-X_n$ to X_p. The energy band diagram is also shown in Fig. 4.1(b).

From Fig. 4.1, the built-in potential ϕ_{bi}^{G} can be expressed by

$$\phi_{bi}^{G} = \phi_{n1}^{*} - \phi_{n2}^{*}$$

$$= \phi_{n1}^{*} + \{ \frac{1}{q} [E_g^P - \frac{\delta E_g}{L} (x_{pg} - x_p)] - \phi_{p2}^{*} \} \qquad (4.8)$$

where $L = x_{pg} + x_{ng}$, $\delta E_g = E_g^P - E_g^N$; E_g^P and E_g^N are the bandgap of p- and n-region, respectively. From Eqs. (2.10) and (2.11), we obtain

$$\phi_{bi}^{G} = \frac{1}{q} [E_g^P - \frac{\delta E_g}{L} (x_{pg} - x_p)] + (\phi_{n1}^{*} - \phi_{p2}^{*})$$

$$= \frac{kT}{q} [\ell n (\frac{np}{N_v N_c})] + \frac{kT}{q} [F(Y_n) + F(Y_p)] + \frac{1}{q} E_{gG}^{*} \qquad (4.9)$$

and

$$E_{gG}^{*} = \frac{1}{q} [(E_g^i - \Delta E_g^P) - \frac{\delta E_g}{L} (x_{pg} - x_p)] \qquad (4.10)$$

where $F(Y_n)$ and $F(Y_p)$ are given by Eq. (2.3) and may be considered as corrections in the Fermi-Dirac statistics for the degenerate region. As shown in Fig. 2.1, both the values of $F(Y_n)$ and $F(Y_p)$ will approach to 2×10^{-3} and 1×10^{-3} when doping density is equal to 10^{17} cm^{-3}. Note that the second term in the right-hand side of Eq. (4.10) is formed from the graded reduction of bandgap in the transition region of the junction.

4.2.3 Graded junction diode

Since a heavily doped p-n junction diode is treated as a device with a linearly varying bandgap in the transition region, additional terms in the transport equation in addition to that of the conventional drift and diffusion will arise from the variation of the energy band edges and from the spatial dependence of the electron and hole density of states, where the rigid band approximation is assumed. We have also made the fixed-field approximation which is valid for low-level injection and depletion approximation to facilitate the solution of Poisson's equation. The model also assumes uniform doping in both n and p regions. The electron and hole current densities, in the rigid band case, may then be written as

$$J_n = -n\mu_n \frac{\partial}{\partial x}(q\phi) + qD_n \frac{\partial n}{\partial x} \tag{4.11}$$

$$J_p = -p\mu_p \frac{\partial}{\partial x}(q\phi + E_g) - qD_p \frac{\partial p}{\partial x} \tag{4.12}$$

Here, μ_p and μ_n are the hole and electron mobilities; D_n and D_p are the electron and hole diffusion coefficients, respectively; ϕ is the electrostatic potential, and E_g denotes the bandgap. Since $J_p = 0$ for the quasi-neutral p-region in thermal equilibrium, we have, for low-level injection

$$q\frac{d\phi}{dx} \cong -kT\frac{d}{dx}(\ell n\ N_A) - \frac{dE_g}{dx} \tag{4.13}$$

For uniform doping, the injected electron and hole currents may thus be expressed by

$$J_n = kT\mu_n \frac{\partial n}{\partial x} + n\mu_n \frac{dE_g}{dx}$$

$$= qD_n \frac{\partial n}{\partial x} + qnD_n \frac{1}{L_g}\,, \qquad x > x_p \tag{4.14}$$

$$J_p = -\,kT\mu_p \frac{\partial p}{\partial x} - p\mu_p \frac{dE_g}{dx}$$

$$= -\,qD_p \frac{\partial p}{\partial x} - qpD_p \frac{1}{L_g}\,, \qquad x < x_n \tag{4.15}$$

where L_g is assumed to be constant in the transition region. The continuity equations for the injected electrons and holes, under steady state condition, can be written as

$$\frac{1}{q}\frac{dJ_n}{dx} = \frac{n - n^0}{\tau_n} = \frac{\hat{n}}{\tau_n} \tag{4.16}$$

$$\frac{1}{q}\frac{dJ_p}{dx} = -\,\left(\frac{p - p^0}{\tau_p}\right) = -\,\frac{\hat{p}}{\tau_p} \tag{4.17}$$

where, τ_n and τ_p are the minority electron and hole lifetimes, respectively. Here τ_n and τ_p are no longer only depending on the Schockley-Hall-Read (SHR) recombination through recombination centers in the degenerate semiconductor, but trap-assisted Auger and band-to-band Auger recombination are important recombination processes which should be included. p° (or n°) denotes the thermal equilibrium carrier density. $\hat{n}$ and $\hat{p}$ are the excess electron and hole densities, respectively. For the boundary conditions that $\Delta n \simeq \Delta p \simeq 0$ at $x = \pm \infty$, and n, p and their gradients are continuous everywhere, the current and continuity equations for the minority carriers are solved by [33]. Thus, the electron and hole densities are given respectively by

$$n(x) = \begin{cases} c_1 e^{k_1 x} + c_2 e^{k_2 x} + \dfrac{(n_{ie}^P)^2}{N_A} \exp\,[-(x - x_{pg})/L_g]\ , & x_p < x < x_{pg} \\ c_3 e^{-x/L_n} + \dfrac{(n_{ie}^P)^2}{N_A}\ , & x > x_{pg} \end{cases} \tag{4.18}$$

$$p(x) = \begin{cases} B_1 e^{\alpha_1 x} + B_2 e^{\alpha_2 x} + \dfrac{(n_{ie}^N)^2}{N_D} \cdot \exp\,[-(x + x_{ng})/L_g], & -x_{ng} < x < -x_n \\ B_3 e^{x/L_p} + \dfrac{(n_{ie}^N)^2}{N_D}, & x < -x_{ng} \end{cases} \tag{4.19}$$

where $L_n = (D_n \tau_n)^{1/2}$, $L_p = (D_p \tau_p)^{1/2}$ are the minority carrier diffusion length; n_{ie}^N and n_{ie}^P are defined by Eq. (2.27) and (2.28). Other constants are defined by

$$k_1 = -\frac{1}{2L_g}\{1 + [1 + (2L_g/L_n)^2]^{1/2}\} \tag{4.20a}$$

$$k_2 = -\frac{1}{2L_g}\{1 - [1 + (2L_g/L_n)^2]^{1/2}\} \tag{4.20b}$$

$$C_1 = \hat{n}(x_p) e^{k_2 x_{pg}} e^{-x_{pg}/L_n} (k_2 + \frac{1}{L_n})/D \tag{4.20c}$$

$$C_2 = -\hat{n}(x_p)e^{k_1 x_{pg}}e^{-x_{pg}/L_n}(k_1 + \frac{1}{L_n})/D \tag{4.20d}$$

$$C_3 = \hat{n}(x_p)e^{k_1 x_{pg}}e^{k_2 x_{pg}}(k_2 - k_1)/D \tag{4.20e}$$

$$D = e^{-x_{pg}/L_n} \cdot [e^{k_1 x_p} \cdot e^{k_2 x_{pg}}(k_2 + \frac{1}{L_n}) - e^{k_2 x_p}e^{k_1 x_{pg}}(k_1 + \frac{1}{L_n})] \tag{4.20f}$$

and

$$\alpha_1 = -\frac{1}{2L_g}\{1 + [1 + (2L_g/L_p)]^{1/2}\} \tag{4.21a}$$

$$\alpha_2 = -\frac{1}{2L_g}\{1 - [1 + (2L_g/L_p)]^{1/2}\} \tag{4.21b}$$

$$B_1 = \hat{p}(-x_n)e^{-\alpha_2 x_{ng}}e^{-x_{ng}/L_p}(\alpha_2 - \frac{1}{L_p})/G \tag{4.21c}$$

$$B_2 = -\hat{p}(-x_n)e^{-\alpha_1 x_{ng}}e^{-x_{ng}/L_p}(\alpha_1 - \frac{1}{L_p})/G \tag{4.21d}$$

$$B_3 = \hat{p}(-x_n)e^{-\alpha_1 x_{ng}}e^{-\alpha_2 x_{ng}}(\alpha_2 - \alpha_1)/G \tag{4.21e}$$

$$G = e^{-x_{ng}/L_p}[e^{-\alpha_2 x_n} \cdot e^{-\alpha_1 x_{ng}}(\frac{1}{L_p} - \alpha_1) - e^{-\alpha_1 x_n} \cdot e^{-\alpha_2 x_{ng}}(\frac{1}{L_p} - \alpha_2)] \tag{4.21f}$$

By substituting Eqs. (4.18) and (4.19) into Eqs. (4.14) and (4.15), we obtain the electron and hole currents at the space charge region boundaries as

$$J_n(x_p) = -qD_n\hat{n}(x_p)\lambda_1 \tag{4.22}$$

$$J_p(-x_n) = -qD_p\hat{p}(-x_n)\lambda_2 \tag{4.23}$$

where

$$\lambda_1 \equiv -e^{k_1 x_p}\frac{C_1}{\hat{n}(x_p)}(k_1 + \frac{1}{L_g}) - e^{k_2 x_p}\frac{C_2}{\hat{n}(x_p)}(k_2 + \frac{1}{L_g}) \tag{4.24}$$

and

$$\lambda_2 \equiv e^{-\alpha_1 x_n}\frac{B_1}{\hat{p}(-x_n)}(\alpha_1 + \frac{1}{L_g}) + e^{-\alpha_2 x_n}\frac{B_2}{\hat{p}(-x_n)}(\alpha_2 + \frac{1}{L_g}) \tag{4.25}$$

By assuming no recombination in the space-charge region, the total forward current density is given by

$$J_{tot} = qD_p\hat{p}(-x_n)\lambda_2 + qD_n\hat{n}(x_p)\lambda_1 \tag{4.26}$$

The minority carrier densities at the space-charge region boundaries may be obtained by using law of the junction as

$$\begin{aligned} n(x_p) &= n^0(x_p)\ \exp\ (qV_a/kT) \\ &= \frac{(n_{ie}^P(x_{pg}))^2}{N_A}\exp\ [(x_{pg} - x_p)/L_g]\cdot\exp\ (qV_a/kT) \end{aligned} \tag{4.27}$$

$$\begin{aligned} p(-x_n) &= p^0(-x_n) \exp (qV_a/kT) \\ &= \frac{(n_{ie}^N(-x_{ng}))^2}{N_D} \cdot \exp [- (x_{ng} - x_n)/L_g] \cdot \exp (qV_a/kT) \end{aligned} \tag{4.28}$$

Thus, the diode current density in Eq. (4.26) can be expressed as

$$\begin{aligned} J_{tot} &= \{qD_p\lambda_2 \frac{(n_{ie}^N)^2}{N_D} \exp[(x_n - x_{ng})/L_g] + qD_n\lambda_1 \frac{(n_{ie}^P)^2}{N_A} \exp[(x_{pg} - x_p)/L_g]\} \\ &\quad \times [\exp (qV_a/kT) - 1] \\ &\equiv J_o \cdot [\exp(qV_a/kT) - 1] \end{aligned} \tag{4.29}$$

It is noted that Eq. (4.29) will reduce to the conventional diode current density expression in the limit of $1/L \cong 1/L_g \cong 0$. The additional exponential terms appeared in Eq. (4.29) are due to the effect of bandgap narrowing.

The space charge region boundaries, X_n and X_p may be obtained as functions of the applied voltage by solving Poisson's equation as described in section 2.3.3. We obtain the voltage drop across the space-charge region as

$$\begin{aligned} V_j &= \phi_{bi}^G - V_a \\ &= \frac{q}{2} (\frac{N_p x_n^2}{e_n} + \frac{N_A x_p^{2\ 2}}{e_p}) + \frac{1}{q} [\frac{\delta E_g}{L} x_p] \end{aligned} \tag{4.30}$$

Since the total charge per unit area in the space-charge region is $Q_{SCR} = qN_Dx_n - qN_Ax_p$, and $|Q_{SCR}| << qN_Dx_n$ or qN_Ax_p, we may assume

$$N_Dx_n \simeq N_Ax_p \tag{4.31}$$

The space charge boundary, X_p and X_n for a heavily-doped pn graded junction can be obtained by using Eq. (4.30) and (4.31)

$$x_p = \frac{2\zeta}{qN_A} [(\frac{1}{C_g^2} + \frac{\phi_{bi}^G - V_a}{\zeta})^{1/2} - \frac{1}{C_g}] \tag{4.32}$$

$$x_n = \frac{2\zeta}{qN_D} [(\frac{1}{C_g^2} + \frac{\phi_{bi}^G - V_a}{\zeta})^{1/2} - \frac{1}{C_g}] \tag{4.33}$$

where

$$\zeta = (q\varepsilon_{sp}\varepsilon_{sn}N_AN_D)/2(\varepsilon_{sp}N_A + \varepsilon_{sn}N_D) \tag{4.34}$$

$$\frac{1}{C_g} = \delta E_g/q^2N_AL \tag{4.35}$$

Thus, the depletion layer width can be written as

$$x_d = (\frac{2\zeta}{q})(\frac{1}{N_A} + \frac{1}{N_D})[(\frac{1}{C_g^2} + \frac{\phi_{bi}^G - V_a}{\zeta})^{1/2} - \frac{1}{C_g}] \tag{4.36}$$

where ϕ_{bi}^G is the built-in potential given by Eq. (4.9).

The transition region boundaries, x_{pg} and x_{ng}, are experimentally determined by the plot of $\frac{1}{C^2}$ vs. V_a. It may be depicted as follows:

The capacitance per unit area is defined by $C = |dQ/dV_a|$, where Q represents the charge per unit area in half of the junction region. We can write

$$C = qN_A \frac{dx_p}{dV_a} \tag{4.37}$$

By substituting Eq. (4.30) and (4.31) into Eq. (4.37), we obtain

$$C = \frac{1}{(x_n/\varepsilon_{sn}) + (x_p/\varepsilon_{sp}) + \frac{1}{C_g}} \tag{4.38}$$

Substituting Eq. (4.31) and (4.32) into (4.38), we have

$$\frac{1}{C^2} = (\frac{1}{C_g^2} + \frac{\phi_{bi}^G - V_a}{\zeta}) \tag{4.39}$$

where $\frac{1}{C_g^2}$ is due to the bandgap narrowing effect imposed on the electric field at the edges of the space charge region. From Eq. (4.39), a plot of $\frac{1}{C^2}$ vs. V_a gives a straight line with an extrapolated interception with voltage axis at

$$V_o = \phi_{bi}^G + \zeta/C_g^2 \tag{4.40}$$

Thus, x_{pg} can be determined from Eq. (4.40) and (4.9) by using the dopant-density dependent bandgap narrowing data and assuming $x_{pg} = x_{ng} = \frac{L}{2}$.

4.3 Results and discussion

Calculations of the effects of heavy doping on the built-in potential and electron current density for a heavily-doped Si n^+p graded junction were carried out by assuming a constant bandgap gradient and using the expressions described in section 4.2. Table 4.1 shows the calculated built-in potential of a heavily-doped Si n^+p graded junction with and without including the heavy doping effects, and assuming $x_{ng} = x_{pg} = L/2$ for different transition region widths. The doping density of n^+ side is assumed to be 1×10^{20} cm^{-3}, and the acceptor density on the lightly doped side is 5×10^{18} cm^{-3}. The bandgap narrowing data used in these calculations are reported by Neugroschel et al. [7]. From Table 4.1, it is shown that the modified built-in potential, ϕ_{bi}^G, calculated from Eq. (4.9) assuming L = 0.05, 0.1, 0.2, and 0.4 μm and without including the effect of dopant density dependent dielectric constant, are about 110 to 140 mV smaller than those calculated from conventional expression. Values of ϕ_{bi}^G calculated from Eq. (4.9) including the effect of dopant density dependent dielectric constant (assuming $\varepsilon_{sp} = 32.9$) are also listed in Table 4.1. The values are about 90 to 140 mV smaller than those calculated from conventional expression. Thus, the heavy doping effects such as carrier degeneracy and bandgap narrowing have an important influence on the value of built-in potential of a heavily-doped Si pn graded junction. Note that the effect of dopant-density dependent dielectric constant will signficantly increase the values of ϕ_{bi}^G in the narrow transition region. As for a wider transition region, the effect of dopant density dependent dielectric constant can almost be ignored.

The results of the calculated electron current density for a heavily-doped Si n^+p graded junction are shown in Figs. 4.2 and 4.3, in which the doping densities of the n^+ and p side are assumed to be 1×10^{20} and 5×10^{18} cm^{-3}, respectively. The corresponding minority carrier diffusivities, D_p and D_n, are assumed to be 1.0 and 5.0 cm^2/sec, respectively; where the minority carrier diffusion lengths, L_p and L_n, are equal to 0.25 and 21 μm [32,21], respectively. Fig. 4.2 shows the electron current density vs. applied forward voltage of a heavily-doped Si n^+p graded junction with a constant bandgap gradient and ε_{sp} = 11.7. Solid line is the values calculated from Eq. (4.22) with L = 0.05 μm, dash line with L = 0.1 μm, and dash-dot line with L = 0.4 μm, respectively; where $x_{ng} = x_{pg} = L/2$ is assumed. The results show that a smaller transition region width will result in smaller electron current density in the quasi-neutral n-region. Fig. 4.3 also shows the electron current density vs. applied forward voltage for the same heavily-doped Si n^+p graded junction with and without including the heavily-doped effects for L = 0.1 μm. Solid line is the values calculated from Eq. (4.22) with ε_{sp} = 11.7, dash-dot line with ε_{sp} = 32.9, and dash line is obtained from the conventional expression, respectively. The results show that the effects of heavy doping, especially the bandgap narrowing and the carrier degeneracy, have a significant influence on the electron current density at the quasi-neutral region of a heavily-doped Si pn graded junction. This is probably because the bandgap gradient affects the transport of the injected minority carriers by influencing the carrier distribution in the quasi-neutral regions. The current density, therefore, depends on the width of the transition region outside the space charge region. Since this width is determined by the width of the space-charge region on either side, J will also depend on the applied voltage through x_n and x_p. λ_1 and λ_2 are the only weak functions of applied voltage, while $\exp(x_n/L_g)$ is the dominant factor.

The dependence of current density on bandgap gradient is due primarily to the fact that thermal equilibrium pn-product has to be modified for a semiconductor with position-dependent band structure. Thus, the dark saturation current in a pn junction as well as the common emitter gain of a bipolar transistor are directly affected by the modified pn-product.

4.4 Summary and conclusions

A theoretical approach of studying the heavy doping effects on the built-in potential and current density in a heavily-doped Si n^+p graded junction has been developed in this chapter. A closed form expresson for the I-V characteristics is presented by modifying the theory of anisotropy heterojunction diode [33-35], in which the depletion approximation and the rigid band model are assumed. The expression is valid for uniform doping and low-level injection cases. A transition region is modeled to extend beyond the space charge region with a constant bandgap gradient. Numerical calculations of the heavy doping effects such as carrier degeneracy, dopant density dependent dielectric constant, and bandgap narrowing were carried out by employing the models described in Section 2.2. The effects of heavy doping and variations of transition region width on the built-in potential and current density of a heavily-doped Si n^+p graded junction are theoretically analyzed in this chapter.

TABLE 4.1

A comparision of the calculated built-in otential of a heavily-doped Si pn graded junction with and without including the heavy doping effects for different transition regin width.

Built-in Potential (Calculated at V_a = 0.1 Volt)	L (μm)	0.05	0.1	0.2	0.4
ϕ_{bi}^{G}	(ε_{sp} = 11.7)	0.989	0.971	0.963	0.958
ϕ_{bi}^{G}	(ε_{sp} = 32.9)	1.01	0.984	0.969	0.962
(Nondegenerate expression)		1.10			

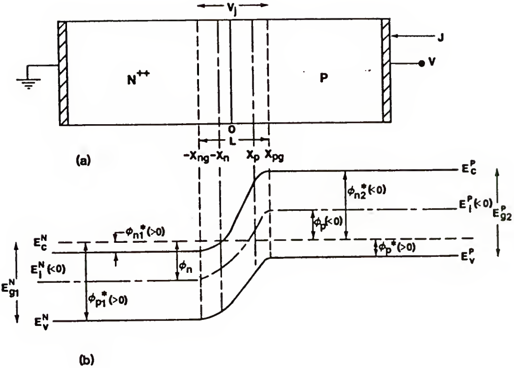

Figure 4.1 (a) Model of the N^{++}- P heavily-doped graded junction; V_j is the voltage across the space charge region and L is the width of the transition region.
(b) The corresponding energy band diagram.

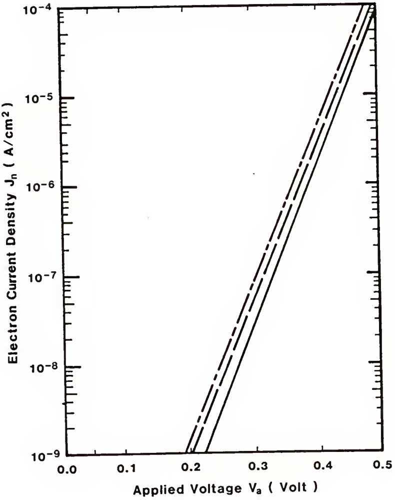

Figure 4.2 Electron current density vs. applied forward bias with transition region width as a parameter for a heavily-doped pn graded junction. Solid line is the values calculated from Eq. (4.22) with L = 0.05 μm, dash line with L = 0.1 μm, and dash-dot line with L = 0.4 μm, respectively; where $x_{ng} = x_{pg} = L/2$ is assumed.

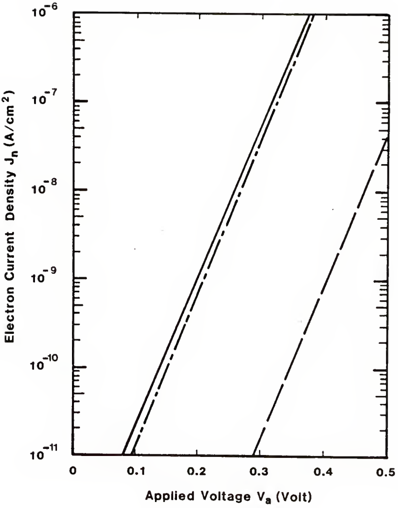

Figure 4.3 Electron current density vs. applied forward bias for a heavily-doped Si pn graded junction. Solid line is the values calculated from Eq. (4.22) with dielectric constant equal to 11.7, dash-dot line with dielectric constant equal to 32.9, and dash line is obtained from the conventional expression, respectively.

CHAPTER V
EFFECTS OF HEAVY DOPING ON THE BUILT-IN POTENTIAL, DEPLETION LAYER WIDTH, DEPLETION CAPACITANCE, AND I-V CHARACTERISTICS OF A HEAVILY-DOPED HETEROJUNCTION DIODE

5.1 Introduction

Recently, two new epitaxial technologies, namely, the molecular beam epitaxy (MBE) and the metal-organic chemical vapor deposition (MOCVD), have emerged into semiconductor technologies. They offer the promise of making highly advanced heterostructures routinely available. Among the different combinations of material being used to produce a heterojunction, the GaAlAs-GaAs system appears to be the most promising candidate. This is due to the fact that $Ga_{(1-x)}Al_xAs$ lattice closely matched to that of GaAs, and the heterojunction structure can be formed without severe interface state effects.

While many kinds of devices will benefit from these emerging technologies, the bipolar transistors and high electron mobility transistors (HEMT) (or Modulation-doped field effect transistors (MODFET)) using III-V compound semiconductor materials will benefit most from the MOCVD and MBE technologies.

The underlying physics is the use of energy gap variations besides electric field to control the forces acting on electrons and holes, it permits a re-optimization of doping levels and geometries, leading to high speed devices. The potential advantages of heterojunction bipolar transistors (HBJT) have been described [39]. For example, a high injection efficiency, a decrease in base resistance, a reduction of the emitter current crowding, and an improvement in frequency response (high gain bandwidth product) have become very promising possibilities in the near future. In addition, the double-heterostructure transistor with both wide-gap emitters and collectors offer additional advantages. It exhibits a better performance under saturated operation, and their emitter and collector may be interchanged by simply changing biasing conditions, greatly simplifying the architecture of bipolar IC's.

HEMT have been intensively studied by many researchers at different laboratories. This field-effect transistor is fabricated by a heterojunction with a doped AlGaAs layer to an adjacent undoped GaAs in such a way that the mobilities and velocities of the charge carriers moving in the undoped gallium arsenide can be modulated and optimized. The device also accepts and releases considerable amounts of charges rapidly, and it dissipates very little energy in switching operation. Thus it is also expected to be the very promising candidate for the needs of supercomputers [40].

Both the HBJT and HEMT contain heavily-doped heterojunction, thus it becomes very important to study the effects of heavy doping on the built-in potentail, depletion layer width, depletion capacitance, and I-V characteristics in a heavily-doped heterojunction diode. Since the effective density of conduction band states of GaAs and $Al_{0.3}Ga_{0.7}As$ are about 4.7×10^{17} and 7.0×10^{17} respectively at $T = 300$ K, carrier degeneracy will be the dominant heavy doping effect in the heavily-doped GaAs-AlGaAs heterojunction diode. While the effect of bandgap narrowing will be less important due to the very small electron effective mass in GaAs and AlGaAs.

Both MBE and MOCVD technologies are capable of growing epitaxial layers with high crystalline perfection and purity. Highly controlled doping levels up to 10^{19} impurities per cm^3 and higher can be achieved. In addition, highly controlled changes in doping level are possible during growth without interrupting the epitaxial growth, and with, at most, a minor adjustment in growth parameters [39]. The doping may be changed either gradually or abruptly due to the comparatively low growth in temperatures. Effects of heavy doping on a heavily-doped graded and abrupt heterojunction will thus be depicted in the following sections. In section 5.2, the expression for built-in potential is derived, and expressions for the depletion layer width and depletion capacitance are reformulated. Results of numerical calculations are described in section 5.3. Section 5.4 presents a summary and conclusions.

5.2 Graded heterojunction

5.2.1 Built-in potential

In addition to the assumptions made for a heavily-doped Si pn junction diode as described in Chapter IV, we also assume that the change in band structure due to strain is negligible.

The energy band diagram before formation of a pn GaAs-$Al_xGa_{1-x}As$ heterojunction diode is shown in Fig. 5.1. Where χ and Φ denote the electron affinity and work function of semiconductor, respectively. Fig. 5.2 shows the schematic representation of a GaAs-$Al_xGa_{1-x}As$ pn graded junction in thermal equilibrium. We may obtain the built-in potential across the space charge region

$$\phi_{bi}^{G} = (\phi_{n2}^{*} - \phi_{n1}^{*})$$

$$= \phi_{n2}^{*} + \{ \frac{1}{q} [E_{g1} + \frac{\delta E_g}{L} (x_{pg} - x_p) - \Delta X] - \phi_{p1}^{*} \} \tag{5.1}$$

where ΔX is the electron affinity difference across the space charge boundaries. A hyperbolic tangent is usually a good approximation for X [41], i.e.,

$$X(x) = (\delta X/2) \tanh (mx/L) + b \tag{5.2}$$

Here, m and b are constants, $\delta X = X_1 - X_2$, and $L = x_{ng} + x_{pg}$. If the width of the space charge region is small compared to that of the transition region, $X(x)$ can be approximated by its Taylor series expansion up to the linear term. Thus,

$$\frac{dX}{dx} = \frac{\delta X}{2} \frac{m}{L} \tag{5.3}$$

and

$$\Delta X = (x_n + x_p) \frac{\delta X}{2} \frac{m}{L} \tag{5.4}$$

For a heavily-doped graded heterojunction, we may use Eq. (2.1), (2.2) and (5.4), and modify Eq. (5.1)

$$\phi_{bi}^{G} = (\phi_{n2}^{*} - \phi_{p1}^{*}) + \frac{1}{q} [E_{g1}^{i} - \Delta E_{g1} + \frac{\delta E_g}{L} (x_{pg} - x_p) - \Delta X]$$

$$= \frac{kT}{q} [\ln (\frac{N_A N_D}{N_V N_C})] + \frac{kT}{q} [F(Y_n) + F(Y_p)] + E^*_{gG}/q \qquad (5.5a)$$

Where, $F(Y_n)$ and $F(Y_p)$ are defined by Eq. (2.3), and

$$E^*_{gG} = [E^i_{g1} - \Delta E_{g1} + \frac{\delta E_g}{L} (x_{pg} - x_p) - (x_n + x_p) \frac{\delta X}{2} \frac{m}{L}] \qquad (5.5b)$$

here, ΔE_{g1} is the bandgap narrowing in the heavily-doped p region.

5.2.2 Depletion layer width and depletion capacitance

The depletion layer boundaries, x_n and x_p, can be obtained by solving Poisson's equation

$$\frac{d^2\phi}{dx^2} = \frac{q}{\varepsilon_s} (n - p - N_D + N_A) - \frac{d\phi}{dx} \frac{d\ln\varepsilon_s}{dx} \qquad (5.6)$$

Since accurate numerical solution for an n^+-p structure with a Gaussian doping profile indicates that even a substantial variation of ε has little effect on the solution for $\phi(x)$ [33], Eq. (5.6) can be simplified by assuming ε_s to be constant in the region of interest and by making the depletion approximation. The boundary conditions for the quasi-neutral region are given by

$$\frac{d\phi(x_n)}{dx} = - \frac{1}{q} \frac{dX(x_n)}{dx} \qquad (5.7)$$

$$\frac{d\phi(-x_p)}{dx} = - \frac{1}{q} [\frac{dX(-x_p)}{dx} + \frac{kT}{L_g}] \qquad (5.8)$$

Solving the Poissons equation under these conditions we obtain the voltage drop across the space-charge region

$$\phi_{bi}^{G} - V_a = \frac{q}{2}\left(\frac{N_D x_n^2}{\varepsilon_{sn}} + \frac{N_A x_p^2}{\varepsilon_{sp}}\right) + \frac{1}{q}\left[x_n \frac{dX(x_n)}{dx} + x_p \frac{dX(-x_p)}{dx} + (\delta E_g/L)x_p\right] \tag{5.9}$$

Solving Eq. (5.9) and (4.31) simultaneously and using Eq. (5.3), we obtain

$$x_p = \frac{2\zeta}{qN_A}\left[\left(\frac{1}{C_{gh}^2} + \frac{\phi_{bi}^{G} - V_a}{\zeta}\right)^{1/2} - \frac{1}{C_{gh}}\right] \tag{5.10}$$

$$x_n = \frac{N_A}{N_D} x_p \tag{5.11}$$

where

$$\zeta = \frac{q\varepsilon_{sp}\varepsilon_{sn}N_A N_D}{2(\varepsilon_{sp}N_A + \varepsilon_{sn}N_D)} \tag{5.12a}$$

$$\frac{1}{C_{gh}} = \frac{m\delta X}{2q^2 L}\left(\frac{1}{N_A} + \frac{1}{N_D}\right) + \frac{\delta E_g}{q^2 N_A L} \tag{5.12b}$$

Thus the depletion layer width for a heavily-doped graded heterojunction can be expressed by

$$x_{dG} = \left(\frac{2\zeta}{q}\right)\left(\frac{1}{N_A} + \frac{1}{N_D}\right)\left[\left(\frac{1}{C_{gh}^2} + \frac{\phi_{bi}^{G} - V_a}{\zeta}\right) - \frac{1}{C_{gh}}\right] \tag{5.13}$$

where, ϕ_{bi}^{G} is given by Eq. (5.5).

The depletion capacitance can also be written as

$$C = qN_A \frac{dx_p}{dV_a}$$

$$= \left(\frac{1}{C_{gh}^2} + \frac{\phi_{bi}^G}{\zeta}\right)^{-1/2} \qquad (5.14)$$

where, the term $1/C_{gh}^2$ is due to the changes of bandgap and electron affinity at the edges of the space charge region. Using the dopant-density dependent bandgap narrowing data and assuming $x_{pg} = x_{ng} = L/2$, the transition region boundaries, x_{ng} and x_{pg}, can also be determined by the plot of $1/C^2$ vs. V_a and Eq. (5.5).

5.3 Abrupt heterojunction

An abrupt heterojunction is distinguished from a graded heterojunction according to the width of the transition region near the interface of the two semiconductors. For a heterojunction to be abrupt, the transition from one material to the other is completed within a few atomic distances. For this case, the material parameters are assumed to change abruptly at the interface. We assume this interface is formed between semiconductors with a good lattice match, e.g., GaAs-$Al_xGa_{1-x}As$, so that the effects of lattice strain, interface states, and dipoles [34] can be neglected (i.e., no interfacial charge at the interface).

5.3.1 Built-in potential

Fig. 5.3 shows the schematic representation of GaAs-$Al_xGa_{1-x}AS$ heterojunction in thermal equilibrium. Here, ϕ_D is the total built-in potential, ϕ_{DP} is the built-in potential on the P-side, and on the N-side is ϕ_{DN}. The total built-in potential across the space charge region is

$$\phi_D = \phi_n - \phi_p$$

$$= (\phi^*_{n2} - \frac{1}{q} E^N_i) + [\frac{1}{q} (E_{g1} + E^P_i) - \phi^*_{p1}] \qquad (5.15)$$

Since

$$E^N_i = E_{c2} - \frac{1}{2} E_{g2} + \frac{kT}{2} \ln (\frac{N_{v2}}{N_{c2}}) \qquad (5.16a)$$

$$E^P_i = E_{v1} + \frac{1}{2} E_{g1} - \frac{kT}{2} \ln (\frac{N_{c1}}{N_{v1}})$$

$$= (E_{c1} - \frac{1}{2} E_{g1}) - \frac{kT}{2} \ln (\frac{N_{c1}}{N_{v1}}) \qquad (5.16b)$$

Eq. (5.15) can be written as:

$$\phi_D = \frac{1}{q} [(E_{c1} - E_{c2}) + \frac{1}{2} (E_{g1} + E_{g2})] + \frac{kT}{2} \ln (\frac{N_{v1}/N_{c1}}{N_{v2}/N_{c2}}) + (\phi^*_{n2} - \phi^*_{p1})$$

$$(5.17)$$

Conventionally, the built-in potential for an abrupt nondegenerate doping heterojunction is given by [33]

$$\phi_{D0} = \frac{kT}{q} [\ln (\frac{N_A N_D}{N_{v1} N_{c2}})] + \frac{1}{2q} (E_{g1} + E_{g2}) + (X_1 - X_2) + \frac{kT}{2} \ln (\frac{N_{v1}/N_{c1}}{N_{v2}/N_{c2}})$$

$$(5.18)$$

For a heavily-doped abrupt pn heterojunction, Eq. (5.17) can be modified using Eq. (2.1) and (2.2)

$$\phi_D = \frac{kT}{q}[\ell n(\frac{N_A N_D}{N_{v1} N_{c2}})] + \frac{kT}{q}[F(Y_n) + F(Y_p)] + (X_1 - X_2) + \frac{kT}{2}\ell n(\frac{N_{v1}/N_{c1}}{N_{v2}/N_{c2}}) + \frac{1}{q}E^*_{gA} \tag{5.19a}$$

where,

$$Y_n = n/N_{c2}\ , \quad Y_p = p/N_{v1}\ ,$$

and

$$E^*_{gA} = \frac{1}{2}\,(E^i_{g1} + E^i_{g2}) - \frac{1}{2}\,(\Delta E_{g1} + \Delta E_{g2}) \tag{5.19b}$$

here, ΔE_{g1} and ΔE_{g2} are the bandgap narrowing due to the effect of heavy doping.

5.3.2 Depletion layer width and depletion capacitance

Since the electric flux density $D = \varepsilon_s E$ is continuous at the junction interface (i.e., $\varepsilon_{sn}E_N = \varepsilon_{sp}E_p$ at $X = 0$) and $\phi_D = \phi_{DN} + \phi_{DP}$, we can obtain the depletion region boundaries, x_n and x_p, for a heavily-doped abrupt heterojunction by using the nondegenerate formulations from [42] and replacing the conventional built-in potential with Eq. (5.19)

$$x_p = [\frac{2\varepsilon_{sp}\varepsilon_{sn}}{q}\ \frac{(\phi_D - V_a)N_D}{N_A(\varepsilon_{sp}N_A + \varepsilon_{sn}N_D)}]^{1/2} \tag{5.20}$$

$$x_n = [\frac{2\varepsilon_{sp}\varepsilon_{sn}}{q}\ \frac{(\phi_D - V_a)N_A}{N_D(\varepsilon_{sp}N_A + \varepsilon_{sn}N_D)}]^{1/2} \tag{5.21}$$

and

$$x_{dA} = x_p + x_n$$

$$= [\frac{2\varepsilon_{sp}\varepsilon_{sn}}{q}(\phi_D - V_a)]^{1/2} [\frac{(N_A + N_D)}{(\varepsilon_{sp}N_A + \varepsilon_{sn}N_D)N_A N_D}]^{1/2} \qquad (5.22)$$

The depletion capacitance thus is given by

$$C = |\frac{dQ}{dV_a}|$$

$$= [\frac{q\varepsilon_{sp}\varepsilon_{sn}}{2(\phi_D - V_a)}]^{1/2} [\frac{N_A N_D}{(\varepsilon_{sp}N_A + \varepsilon_{sn}N_D)}]^{1/2} \qquad (5.23)$$

By plotting $1/C^2$ as a function of V_a, Eq. (5.23) shows that the intercept of $1/C^2 = 0$ is ϕ_D. Now by measurement of capacitance per unit area, ΔE_g ($= \Delta E_{g1} + \Delta E_{g2}$) may be found from Eq. (5.19) if the ΔE_c ($= X_1 - X_2$), Fermi levels, dopant densities, and intrinsic energy gaps on each side of the heterojunction are known. Due to the very small electron density of state effective mass, the calculated values of ΔE_g will be mainly contributed by ΔE_{g1}. Thus, ΔE_{g1} may be separately determined from such calculations.

5.3.3 I-V characteristics

In the heterojunction case, the diffusion current is dominated by injection from the wider energy gap semiconductor into the narrow energy gap semiconductor. There are three assumptions for the ideal current-voltage model: 1) the space charge region depletion layer has abrupt boundaries so that outside the depletion region the semiconductor is assumed to be neutral; 2) the injected minority carrier densities are assumed small compared to the majority carrier densities; 3) there is no generation and recombination current in the depletion region so that the electron and hole currents are constant through the depletion region.

Thus, from Eq. (4.6) and Fig. 5.3, we may obtain the electron current flow at $X = -x_p$

$$J_n = qD_n \frac{dn}{dx}\bigg|_{x = -x_p}$$

$$= \left(\frac{qD_nN_D}{L_n}\right) \exp\left[-((q\phi_D - \delta E_c)/kT) + F(Y_n)\right] \cdot (e^{qV_a/kT} - 1) \qquad (5.24)$$

This flow of electrons in the negative x direction corresponds to a positive current in the positive x direction. Similarly, for holes on the N-side, the hole current density is given by:

$$J_p = \frac{qD_pN_A}{L_p} \exp\left[-((q\phi_D + \delta E_v)/kT) + F(Y_p)\right] \cdot (e^{qV_a/kT} - 1)$$

$$= J_{po} \cdot N_A \cdot \exp\left[-((q\phi_D + \delta E_v)/kT) + F(Y_p)\right] \qquad (5.25)$$

The influence of the heavy doping effects on a heavily doped heterojunction transisitor can be illustrated by taking the ratio J_n/J_p:

$$\frac{J_n}{J_p} = \frac{D_nL_pN_D}{D_pL_nN_A} \cdot \exp\left[(\delta E_c + \delta E_v)/kT + F(Y_n) - F(Y_p)\right]$$

$$= \beta^* \cdot \frac{N_D}{N_A} \cdot \exp\left[(\delta E_c + \delta E_v)/kT + F(Y_n) - F(Y_p)\right] \qquad (5.26)$$

Note that for the example of Fig. 5.3 with $X = 0.3$, where $\delta E_c + \delta E_v = (1.798 - 1.424) = 0.374$ eV, the exponential term in Eq. (5.26) dominates, and $|J_n| >> |J_p|$. Therefore the diffusion current is due to injection of majority carriers from the wider energy gap side into the narrower energy gap side. The total current density may then be generally approximated by $J_t \simeq J_n$.

5.4 Results and discussion

Calculations of the effects of heavy doping on the total built-in potential, depletion layer width, and hole current density for a heavily-doped pn abrupt heterojunction were carried out by using the expressions derived in Section 5.3. Fig. 5.4 and 5.5 show the values of function F(Y) vs. hole or electron density in the heavily-doped GaAs and $Al_{0.3}Ga_{0.7}As$ at T = 300 K, respectively, where F(Y) is calculated from Eq. (2.3). Solid lines are values for electrons, dash lines for holes. Values of F(Y) vary from 8×10^{-2} to 6.13 and 5.2×10^{-2} to 4.8 for n-type GaAs and $Al_{0.3}Ga_{0.7}As$ respectively for dopant densities in the range of 1×10^{17} to 1×10^{19} cm^{-3}.

The numerical results for the total built-in potential of a heavily-doped np abrupt heterojunction are shown in Figs. 5.6 and 5.7. Fig. 5.6 shows the total built-in potential vs. emitter dopant density, N_D, for a heavily-doped abrupt $Al_{0.3}Ga_{0.7}As$-GaAs emitter-base heterojunction of the wide-bandgap npn transistor at T = 300 K, in which the base dopant density, N_A, is assumed to be 1×10^{19} cm^{-3}. Solid line is the predicted values by using Eq. (5.19), dash line is calculated by using the conventional theory from Eq. (5.18). Fig. 5.7 shows the total built-in potential vs. base dopant density, N_A, for the same heavily-doped abrupt $Al_{0.3}Ga_{0.7}As$-GaAs heterojunction at T = 300 K, and the emitter dopant density, N_D, is assumed to be 1×10^{17} cm^{-3}. Solid line is the calculated values by using Eq. (5.19), dash line is calculated by using the conventional theory from Eq. (5.18). Thus, the heavy doping effects of carrier degeneracy and bandgap narrowing will also have a significant influence on the total built-in potential of a heavily-doped pn abrupt heterojunction. It is noted that owing to the effective masses of electron in GaAs and GaAlAs are very small, the effect of bandgap narrowing in n-type GaAs and AlGaAs is negligible. On the other hand, carrier degeneracy is the dominant heavy doping effect in the heavy-doped GaAs-AlGaAs heterojunction devices.

Fig. 5.8 shows the depletion layer width vs. emitter dopant density, N_D, for a heavily-doped abrupt $Al_{0.3}Ga_{0.7}As$-GaAs heterojunction at T = 300 K, in which base dopant density, N_A, is assumed to be 1×10^{20} cm^{-3}. Solid line is the calculated values by using Eq. (5.22), dash line is calculated by using the conventional nondegenerate expression as shown in [42]. The results show that the effects of carrier degeneracy and bandgap narrowing have little influence on the depletion layer width.

The hole current density vs. emitter dopant density at T = 300 K is shown in Fig. 5.9; where the base dopant density, N_A, is assumed to be 1×10^{17} cm^{-3}. Solid line is the calculated values using Eq. (5.25), dash line is calculated by using the conventional theory for abrupt heterojunction diodes [42]. Note that the value of conduction band discontinuity used in these calculations is given by [42]

$$\delta E_c = (0.85 \pm 0.03) \cdot (E_{g1}^{i} - E_{g2}^{i}). \tag{5.27}$$

From Fig. 5.9, it is clearly shown that carrier degeneracy and bandgap narrowing have an important effect on the current density. The results show significant difference from those predicted by the nondegenerate expressions. The effects of carrier degeneracy and bandgap narrowing on heavily-doped heterojunction transistor current gain are shown in Fig. 5.10, where the emitter dopant density, N_D, is assumed to be 1 x 10^{17} cm^{-3}. Solid line is the calculated values by using Eq. (5.26); dash line is calculated by using the conventional theory as shown in [42]. Thus, it is clearly shown that carrier degeneracy have significant influences on the current gain of a heavily-doped heterojunction transistor.

5.5 Summary and Conclusions

A theoretical study of the heavy doping effects on the built-in potential, depletion layer width, current density, and current gain for heavily-doped abrupt and graded heterojunction devices has been carried out in this chapter. A transition region is modeled to extend beyond the space charge region with a constant bandgap gradient for the graded heterojunction case. Calculations of the heavy doping effects such as carrier degeneracy and bandgap narrowing were carried out by employing the empirical models described in Section 2.2. Numerical results for a heavily-doped $Al_{0.3}Ga_{0.7}As$-GaAs heterojunction transitor are given. The results of the present study show that: 1) bandgap narrowing and carrier degeneracy have important effects on the total built-in potential and carrier current density, as well as, the transistor current gain, β; 2) the effects of heavy doping on the depletion layer width and depletion capacitance are insignificant; 3) the effect of carrier degeneracy is the dominant heavy doping effect in the heavily-doped GaAs-AlGaAs heterojunction devices due to the very small electron effective masses in GaAs and AlGaAs. The present results show that the new calculated values for the built-in potential, carrier current density, and transistor current gain may differ significantly from those predicted by the nondegenerate theories.

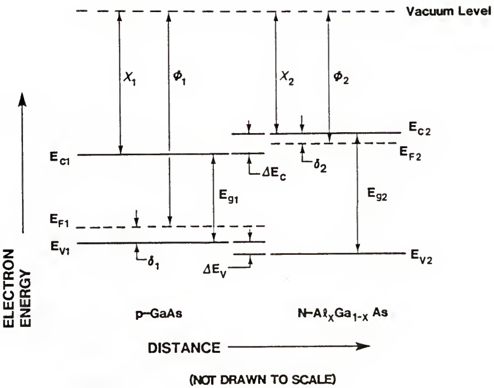

Figure 5.1 Energy band diagram before formation of an pn GaAs-AlGaAs heterojuction.

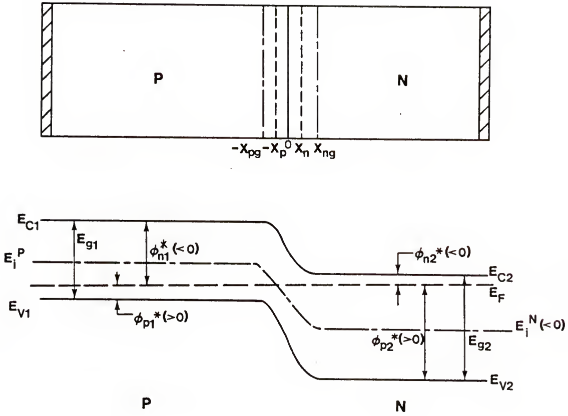

Figure 5.2 Schematic representation of a GaAs-Al$_x$Ga$_{1-x}$As pn graded junction in thermal equilibrium.

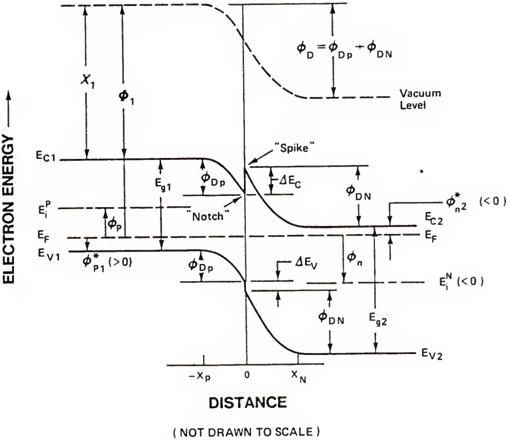

Figure 5.3 Schematic representation of a GaAs-Al$_x$Ga$_{1-x}$As pn abrupt heterojunction in thermal equilibrium.

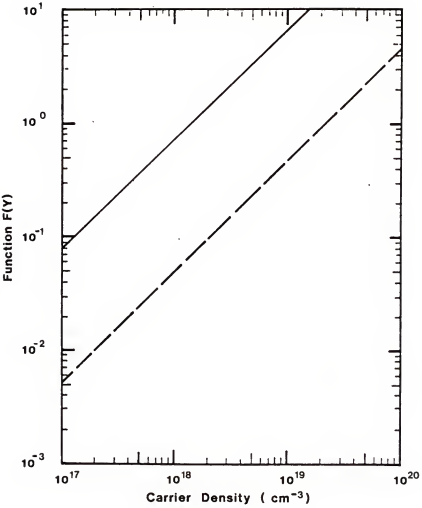

Figure 5.4 Values of function F(Y) vs. hole or electron density in the heavily-doped GaAs at T = 300 K. Where F(Y) is calculated from Eq.(2.3). Solid line is values for electrons, dash line for holes.

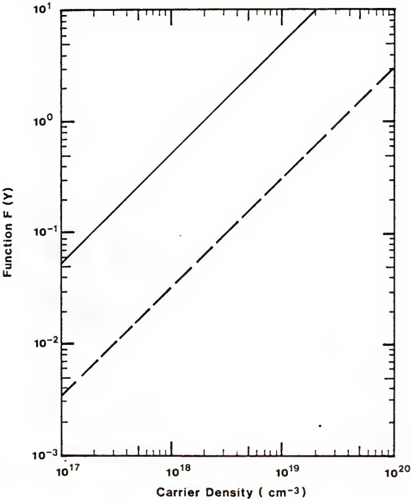

Fig. 5.5 Values of function F(Y) vs. hole or electron density in the heavily-doped $Al_{0.3}Ga_{0.7}As$ at T = 300 K. Solid line is values for electrons, dash line for holes.

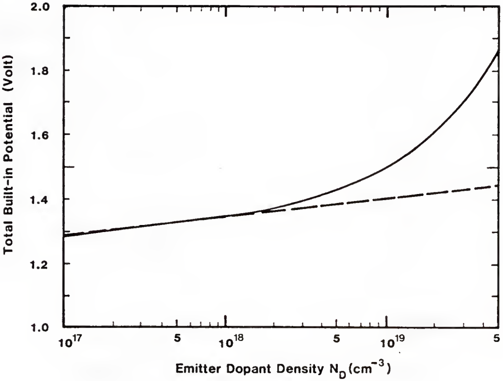

Figure 5.6 Total built-in potential vs. emitter dopant density, N_D, for heavily-doped abrupt $Al_{0.3}Ga_{0.7}As$-GaAs emitter-base heterojunction at T = 300 K. Solid line is the predicted values by using Eq. (5.19), dash line is calculated by using the conventional theory from Eq. (5.18).

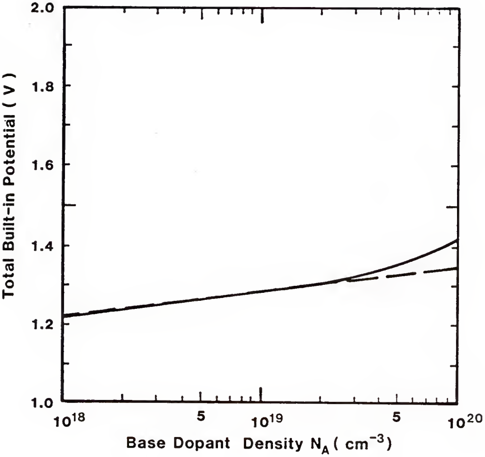

Figure 5.7 Total built-in potential vs. base dopant density, N_A, for heavily-doped abrupt $Al_{0.3}Ga_{0.7}As$-GaAs emitter-base heterojunction at T = 300 K.

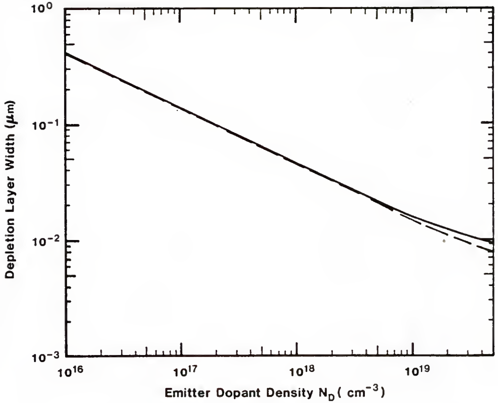

Figure 5.8 Depletion layer width vs. emitter dopant density, N_D, for heavily-doped abrupt $Al_{0.3}Ga_{0.7}As$-GaAs emitter-base heterojunction at T = 300 K.

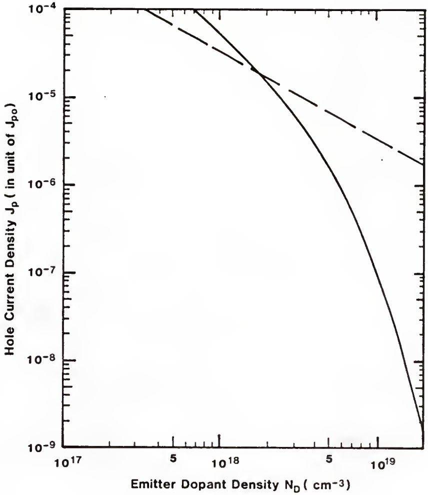

Figure 5.9 Hole current density vs. emitter dopant density, N_D, for heavily-doped abrupt $Al_{0.3}Ga_{0.7}As$-GaAs emitter-base heterojunction at T = 300 K.

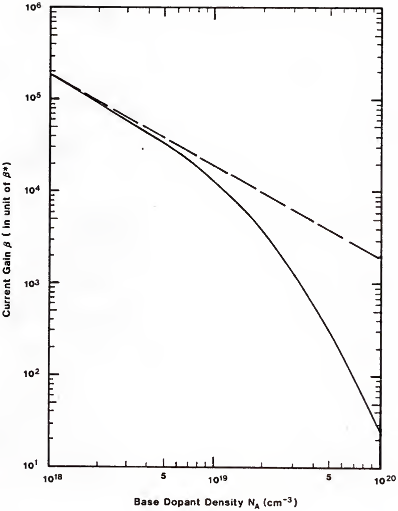

Figure 5.10 Current gain vs. base dopant density, N_A, for an npn transistor with wide bandgap $Al_{0.3}Ga_{0.7}As$ emitter.

CHAPTER VI
EFFECTS OF HEAVY DOPING ON I-V CHARACTERISTICS of GaAs JFET AND MESFET DEVICES

6.1 Introduction

GaAs JFETS and MESFETS, particularly the E-JFET and E-MESFET devices, show great promise for applications in high speed, low power integrated circuits and super computers [43,44]. In addition, for some military and space applications, GaAs ICs are particularly important for their exceptional radiation hardness.

To increase the speed of FET devices, shortening the gate length is most effective. Many experimental results [45-49] show a strong influence of short-channel effects if the channel doping is less than 1 ~ 2 x 10^{17} cm^{-3} and the gate length is shortened below 0.5 μm. The most pronounced short channel effect is a strong negative shift of the threshold voltage V_T. A shift of V_T by -1 to -2 V are reported [48,49], respectively, for intermediate doped channels (< 2 x 10^{17} cm^{-3}) when the gate length is decreased from more than 1 μm to less than 0.3 μm while doping concentrtion and channel thickness remain constant.

In addition to the lowering of the threshold voltage, a slight decrease of transconductance, and the lack of saturation behavior are also observed [50]. All these effects have to be taken into account for device layout and integrated circuit design. One effect, for instance, is that devices with different gate lengths need variations in the production processes to assure equal threshold voltage. On the other hand, an active layer thickness laid out following conventional design rules results in an undesired value for a submicrometer gate's threshold voltage [51]. Therefore, alleviation of these effects is necessary.

Theoretical investigations by Drangeid and Sommerhalder [52] show that the performance of MESFET's can be improved by reduction of the gate length if the dopiong concentration is increased correspondingly, so that the ratio of gate length L to the channel thickness t is maintained at L/t >> 3. Recently, Daembkes et al. [51] have fabricated GaAs MESFET with channel dopant density up to 5×10^{18} cm^{-3} along with both micrometer and submicrometer gates. They reported that the short-channel devices show a good saturation behavior and no shift in the threshold voltage compared to the long-channel devices. Thus, heavily-doped FETs demonstrate a pronounced alleviation of short-channel effects as experienced for 1×10^{17} cm^{-3} doping level. Moreover, it was shown that the use of heavily-doped channels enable the design rules for integrated circuits and device layout to be maintained down to less than 0.5 - µm devices [51].

Since it is necessary to increase the dopant density in order to reduce the size and to improve the electrical characteristics of active devices in the VLSI (or ULSI) and VHSIC circuts, it became more and more important to study how the heavy doping effects such as carrier degeneracy, and bandgap narrowing will affect the performance of a heavily-doped FET.

The purpose of this chapter is to theoretically analyze the effect of heavy doping on the threshold voltage and I-V characteristics of a heavily-doped GaAS JFET and MESFET. Numerical calculations are performed for the heavily-doped E-JFET and E-MESFET devices using a modified expression for the built-in potential described in Chapter II. Empirical approximation for the reduced Fermi-energy is presented by [1], and the GaAs bandgap narrowing expression is given by [53]. The theoretical treatment which includes the reformulation of the built-in potential for a JFET and MESFET are given in Section 6.2. The result and discussion are given in Section 6.3

6.2 Theoretical analysis

The disadvantage of the short-channel effects of a MESFET can be avoided by increasing the channel doping level and accordingly decreasing the channel thickness (i.e., the ratio of gate length L to the channel thickness t is kept at L/t >> 3). Therefore, the current-voltage relation for a uniformly- and heavily-doped FET may still be expressed by that for a long-channel FET, except for the built-in potential expression which should be replaced by Eq. (2.12).

Thus, the drain current for a heavily-doped short-channel and long-channel FET is given by

$$I_D = I_p \{3V_D/V_p - 2[(V_D - V_G + V_{bi})^{3/2} - (V_{bi} - V_G)^{3/2}]/V_p^{3/2}\} \qquad (6.1)$$

and the drain saturation current for a given gate voltage is obtained from Eq. (6.1) as

$$I_{DS} = I_p\{1 - 3[1 + (V_T - V_G)/V_p] + 2[1 + (V_T - V_G)/V_p]^{3/2}\} \tag{6.2}$$

where, I_p ($= w\mu q^2N_D^2t^3/6\varepsilon_sL$) is the pinch-off current; L is the channel length; W is the channel width; μ is the channel mobility; V_p is the channel pinch-off voltage; N_D is the channel doping density for the N-channel FET; V_D is the applied drain voltage; ε_s is the material dielectric constant; t is the channel thickness, and

$$V_T \equiv V_{bi} - V_p \tag{6.3}$$

is the threshold voltage. The built-in potential, V_{bi}, of the gate and channel junction in a conventional JFET device is given by [54]

$$V_{bi} = E_{gi}/q - V_{th}\ln(N_c/N_D) \tag{6.4}$$

where N_c is the effective density of conduction band states, E_{gi} is the intrinsic bandgap of semiconductor, and V_{th} ($= kT/q$) is the thermal voltage. Since the junction between gate and channel in a JFET is a heavily-doped pn junction, the built-in potential, V_{biJ}, for a heavily-doped n-channel JFET should be modified to include the heavy-doping effects as described in Chapter II. It can be rewritten here as:

$$V_{biJ} = V_{th}[\ln(\frac{pN_D}{N_cN_v}) + F(Y_n) + F(Y_p)] + E_g^*/q \tag{6.5}$$

and

$$E_g^* = E_{gi} - (\Delta E_{gN} + \Delta E_{gp})/2 \tag{6.6}$$

where $Y_n = N_D/N_c$, $Y_p = P/N_v$, P is the hole density in the heavily-doped p-gate region, and $F(Y_n)$ (or $(F(Y_p))$ can be approximated by Eq. (2.13). Fig. 5.4 shows the calculated values of $F(Y_n)$ and $F(Y_p)$ for GaAs, values of $F(Y_n)$ vary from 0.075 to 6.14 for electron densities in the range of 1×10^{17} to 1×10^{19} cm^{-3}, and values of $F(Y_p)$ vary from 0.05 to 4.34 for hole densities in the range of 1×10^{18} cm^{-3} to 1×10^{20} cm^{-3}. ΔE_{gN} and ΔE_{gp} are the bandgap narrowing in the n- and p-type semiconductor, respectively [53]. Since the effective mass of electron in GaAs is very small, the effect of bandgap narrowing is negligible for the present case. On the other hand, carrier degeneracy is the dominant heavy doping effect in a heavily-doped n-channel GaAs FET.

The built-in potential, V_{biM}, of the Schottky barrier in a heavily-doped n-channel MESFET can be expressed by [54]

$$V_{biM} = V_{BN} + E_{FN}/q \tag{6.6}$$

where the bandgap narrowing is very small and can be neglected. V_{BN} is the barrier height of the metal-semiconductor contact. The Fermi-energy for an n-type nondegenerate semiconductor is given by $E_{FN} = kT \ \ell n(n/N_c)$, and for a degenerate semiconductor, it can be approximated by [1]

$$E_{FN} = kT[\ell n(\frac{N_D}{N_c}) + F(\frac{N_D}{N_c})] \tag{6.7}$$

Thus, the transconductance of an FET in the saturation region can also be expressed by

$$g_{ms} = g_{max}\{1 - [(V_{biJ(M)} - V_G)/V_p]^{1/2}\} \qquad (6.8)$$

where V_{biJ} and V_{biM} are the built-in potential given by Eqs. (6.5) and (6.6), respectively; and

$$g_{max} = qN_D t\mu w/L \ , \qquad (6.9)$$

μ is dependent on channel doping density and can be described by Hilsum's formula [55].

6.3 Results and Discussion

Calculations of the effects of heavy doping on the threshold voltage shift, I-V characteristics, and transconductance of a JFET and MESFET are carried out at T = 300 K by using equations described in Section 6.2. Figs. 6.1 and 6.2 show the effects of carrier degeneracy and bandgap narrowing on the threshold voltage of a heavily-doped n-channel GaAs E-JFETS and E-MESFETS. Fig. 6.1 shows the threshold voltage shift vs. p-gate region density, N_A, for an n-channel E-JFETS, in which channel dopant density, N_D, is assumed to be 2 x 10^{18} cm^{-3}, and the threshold voltage is about 0.5 volt. The threshold voltage shift vs. channel dopant density for n-channel GaAs E-MESFETS is shown in Fig. 6.2, where the barrier height, V_{BN}, is assumed to be 0.8 volt, and the threshold voltage is about 0.3 volt for E-MESFETS. From Figs. 6.1 and 6.2, it is clearly show that the effects of heavy doping tend to increase the threshold voltage as high as 36% and 80% for E-JFETS and

E-MESFETS, respectively. On the contrary, the short-channel effects tend to reduce the threshold voltages for short-channel FETS. Thus, raising the channel doping level for short-channel FETs not only can avoid the disadvantages of the short-channel effects of a FET and satisfy the criteria of $L/a >> 3$, but also can act as an adjustment of the FET threshold voltage. The I-V characteristics of an n-channel E-MESFET with gate voltage as a parameter is shown in Fig. 6.3. Where channel dopant density, N_D, is assumed to be 1.5×10^{-18} cm^{-3}, channel depth a = 225 Å, and barrier height, V_{BN}, is assumed to be 0.8 volt. Solid lines are the predicted values by Eqs. (6.1), (6.2), and (6.7). Dash lines are the values calculated by the conventional nondegenerate theory from [54]. The results show that the drain current of E-MESFETS will decrease significantly when carrier degeneracy effect is included in the calculations.

Table 1 shows the calculated results of drain saturation current and saturation transconductance for several GaAs D-MESFETS and E-MESFETS with specific device parameters and gate voltages. It is noted that the effect of carrier degeneracy plays an important role on the drain saturation current, I_{DS}, and saturation transconductance, g_{ms}, of D-MESFETS as well as E-MESFETS via the built-in potential presented in the heavily-doped junction between gate and channel. It is expected that the carrier degeneracy will also have significant influence on the I_{DS} and g_{ms} of E-JFETS. On the contrary, carrier degeneracy will have only little influence on the D-JFETS.

6.4 Summary and discussion

In short, the considerations of short-channel effects on the heavily-doped FETs are justified by Daembkes et al. [54] and were shown to be not important for heavily-doped short-channel FETS. The effects of heavy doping on the I-V characteristics of JFETS and MESFETS have been theoretically investigated in this chapter. It is shown that carrier degeneracy has a significant effect on the threshold voltage and the I-V characteristics of a heavily-doped GaAs E-JFETS and E-MESFETS, while the bandgap narrowing effect has negligible influence on the electrical characteristics because of the very small electron effective mass.

TABLE 6.1

Comparisons of calculated drain saturation current and saturation transconductance of GaAs JFETs and MESFETs with specified device parameters and applied gate voltage.

Device	E-MESFET	E-MESFET	D-MESFET	D-MESFET
	n-channel	n-channel	n-channel	n-channel
	$N_D=1.5x10^{18}cm^{-3}$	$N_D=5x10^{18}cm^{-3}$	$N_D=1.5x10^{18}cm^{-3}$	$N_D=5x10^{18}cm^{-3}$
	#V_{BN} = 0.8	V_{BN} = 0.8	V_{BN} = 0.8	V_{BN} = 0.8
	a = 225 Å	a = 125 Å	a = 405 Å	a = 225 Å
	V_G = 0.7 volt	V_G = 0.7 volt	V_G = 0.0 volt	V_G = 0.0 volt
(Theory) parameter				
(Degenerate) I_{DS}/I_p	0.47	0.285	0.211	0.182
(Nondegenerate) I_{DS}/I_p	0.7	0.823	0.251	0.281
(Degenerate) g_{ms}/g_{max}	0.481	0.353	0.297	0.272
(Nondegenerate) g_{ms}/g_{max}	0.634	0.731	0.327	0.349

# in unit of volt.

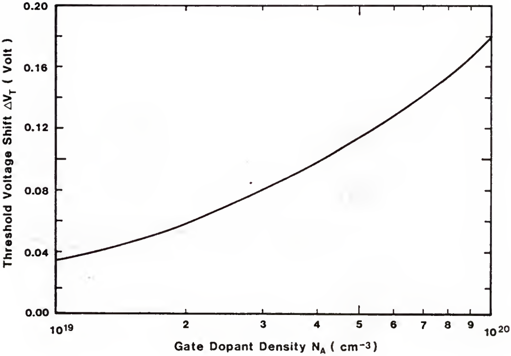

Figure 6.1 Threshold voltage shift vs. p-gate dopant density for n-channel E-JFETs, in which, channel dopant density, N_D, is assumed to be 2×10^{18} cm^{-3}.

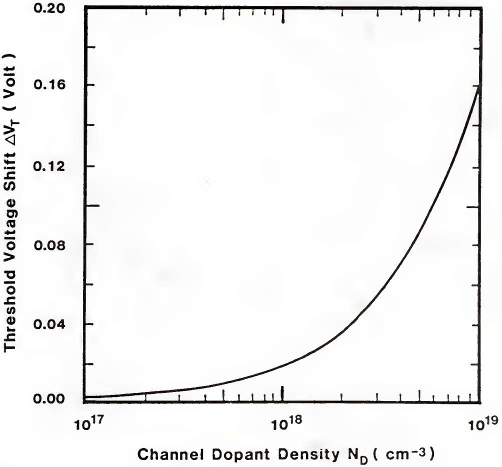

Figure 6.2 Threshold voltage shift vs. channel dopant density for n-channel E-MESFETs.

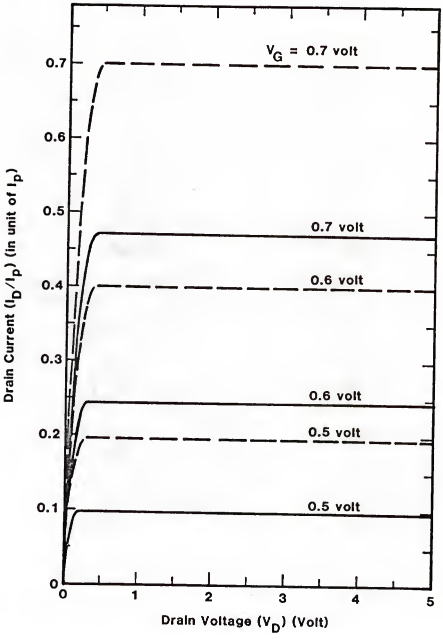

Figure 6.3 I-V characteristics of an n-channel E-MESFET with gate voltage as a parameter. Where, channel dopant density $N_D = 1.5 \times 10^{18}$ cm^{-3}, chnnel depth a = 225 Å, and barrier height V_{BN} is assumed to be 0.8 volt.

CHAPTER VII
EXPERIMENTAL METHODS FOR STUDYING THE METALLIC CONTAMINATION IN SILICON DEVICES

Experimental tools employed in the study of the effects of metallic contamination in electrical characteristics of semiconductor devices include the current-voltage (I-V) measurement, capacitance-voltage (C-V) measurement, thermally stimulated capacitance (TSCAP) measurement, and deep level transient spectroscopy (DLTS) measurement. From these measurements, one can determine the diode characteristics and the defect parameters such as defect energy levels, defect densities, and capture cross sections. Each of these measurement techniques is described in the following sections.

7.1 Current-voltage (I-V) measurement

Measurement of the current-voltage (I-V) characteristics under forward bias condition can yield useful information concerning the conduction mechanisms, recombination processes in the space charge region of a p-n junction diode or a Schottky barrier diode. For a good p-n diode with no surface leakage, the total current is composed of the diffusion current in the quasi-neutral region (QNR) and the recombination current in the space charge (SCR). When bulk diffusion current component dominates, the current expression is given by [9]

$$I_f = I_d[\exp(V_a/V_T) - 1] \tag{7.1}$$

Where V_a is the applied voltage, $V_T = kT/q$, and I_d is the magnitude of the saturation diffusion current.

$$I_d = qn_i^2A[(D_n/L_nN_A) + (D_p/L_pN_D)] \tag{7.2}$$

where n_i is the intrinsic carrier density; A is the diode area; D_n (D_p) is the diffusion constant for electrons (holes); L_n (L_p) is the diffusion length for electrons (holes); and N_A (N_D) is the acceptor (donor) density. If bulk generation-recombination current dominates, then the current expressin is given by [9]:

$$I_r = I_{rg} \exp (V_a/2V_T) \tag{7.3}$$

where I_{rg} is the magnitude of the generation-recombination current.

$$I_{rg} = qn_iW/2\tau_e \tag{7.4}$$

In Eq. (7.4), W denotes the depletion layer width; $\tau_e = (\tau_n\tau_p)^{1/2}$ is the effective carrier lifetime in the space charge region [56]; τ_n (τ_p) is the lifetime of electrons (holes), defined by:

$$\tau_n = 1/(N_t\sigma_n\langle v_{th}\rangle) \tag{7.5}$$

Where N_t is the trap density, σ_n (σ_p) is the capture cross section for electrons (holes); $\langle v_{th} \rangle$ is tHe average thermal velocity.

The total current can be expressed as:

$$I_t = I_f + I_r \approx I_o \exp (V_a/n^* V_T) \tag{7.6}$$

Where I_o is the saturation current; n^* is the ideality factor. The diode ideality factor, n^* can be used to identify the dominant current component in a p-n diode. Inspection of Eqs. (7.1) and (7.3) show that the bulk diffusion current depends more strongly on temperature than the recombination current in the junction SCR. Since the recombination current in the junction SCR is inversely proportional to the effective carrier lifetimes (and hence directly related to the defect density in the transition region), measurements of I-V characteristics under forward bias conditions would allow us to determine the effective lifetimes in Si.

7.2 Capacitance-voltage (C-V) measurement:

The capacitance-voltage (C-V) measurement can be used to determine the background doping concentration in the n- or p- Si epitaxial layers using a Schottky barrier structure or a one-sided abrupt p^+-n (or n^+-p) junction. The deplation capacitance across the Schottky barrier diode is given by:

$$C(V_T) = \varepsilon_s A/W = A\{q\varepsilon_s N_D/[2(\phi_i + V_r - kT/q)]\}^{1/2} \tag{7.7}$$

where ε_s is the dielectric constant of semiconductor, ϕ_i is the built-in potential, and V_r is the applied reverse voltage. Eq. (7.7) shows that the depletion capacitance of a Schottky diode is proportional to the square root of dopant concentration and inversely proportional to the square root of the applied voltage. If the inverse of the capacitance square (C^{-2}) is plotted as a function of the reverse bias voltage V_r, then the background concentration can be calculated from the slope of C^{-2} vs. V_r using the following expression:

$$C^{-2}(V_r) = [2/(q\varepsilon_s A^2 N_D)](\phi_i + V_r) \tag{7.8}$$

The intercept of C^{-2} vs. V_r plot with the voltage axis yields values of ϕ_i which is related to the barrier height of a Schottky diode by:

$$\phi_{BN} = \phi_i + V_n + \frac{kT}{q} - \Delta\phi \tag{7.9}$$

where

$$V_n = E_c - (kT/q)\ \ell n\ (N_D/N_c) \tag{7.10}$$

and $\Delta\phi$ is the image lowering potential of a Schottky diode; N_c is the density of state in the conduction band.

7.3 Thermally stimulated capacitance (TSCAP) measurement:

Thermally stimulated capacitance measurements (TSCAP) add another improvement over the stepped C-V measurement technique as reported by Sah, Senechal, and Basinski [57,58]. The main theoretical aspect which controls the TSCAP results [59-61] is given by

$$e_n^t = f(E,T,t) = \frac{\sigma_n \langle v_{th} \rangle N_c}{g} e^{-(E_c - E_t)/kT} \qquad (7.11)$$

where e_n^t is the electron thermal emission rate, $E_c - E_t$ is the trap depth measured from the band edge, g is a degeneracy factor of the defect level, k is the Boltzmann constant, $\langle v_{th} \rangle$ is the carrier thermal velocity, N_c is the effective density of conduction band states, T is the absolute temperature, and σ_n is the thermal capture cross-section for electrons. If we ignore the temperature dependence of some of the terms given in eq. (7.11), the general expression indicates that each trap will have a unique value of $(E_c - E_t)$ which will make the exponential term of eq. (7.11) maximum at a corresponding unique temperature. This means that when the unique temperature for each trap is reached, the emission for that trap will increase exponentially. However, the source of the emission is limited and must follow a certain time constant, and a peaked emission profile of the trap will result (as shown in Fig. 7.1) for a linearly increasing temperature. Fig. 7.2 shows a typical TSCAP scan that shows only majority carrier traps for a Schottky barrier (three single trap changes and a combined unknown at 77°K). A derivative (dC/dT) of Fig. 7.2 will then result in a capacitance versus temperature plot similar to Figure 7.2. It is also possible that some shallow traps may be present that would emit electrons at temperatures lowr than 77K. In this case, the net trap density can be determined by recording the change ($\Delta C = 0.7$ pf in Fig. 7.2) in the capacitance between $t = 0^+$ (immediately after reverse-bias) and at $t = \infty$ (after it ceases to change), while holding the temperature at 77 K.

The amplitude of the capacitance step (as shown in Fig. 7.2) is directly proportional to the trap density. The trap density for n-Si can be calculated from the following expression:

$$N_t = N_d(2\Delta C/C_o) \tag{7.12}$$

where C_0 is the depletion layer capacitance, and ΔC is the capacitance change due to the majority or minority carrier emission. Thus, knowing N_D (or N_A) and C_0 at the temperature where the capacitance step was observed, the trap density can be calculated from Eq. (7.12). Note that Eq. (7.12) is valid only for the case when $N_t < 0.1\ N_D$. For the case of large trap density with $N_t > 0.1\ N_D$, a more exact expression should be used instead.

7.4 Deep level transient spectroscopy (DLTS):

The Deep-Level-Transient-Spectroscopy (DLTS) experiment is a high frequency (20 MHZ) transient capacitance technique, which was introduced first by Lang in 1974 [62,63]. The DLTS scan displays the spectrum of deep level traps in the forbidden gap of a semiconductor as positive or negative peaks on a flat baseline as a function of temperature. Although this kind of measurement is time consuming, it offers several advantages. It is sensitive, easy to analyze and capable of measuring the traps over a wide range of depth in the forbidden gap.

Fig. 7.4. shows the schematic block diagram of a DLTS system used in this study. The DLTS system consists of a sensitive capacitance measurement apparatus with good transient response, a pulse generator, a boxcar with dual-gated signal integrator, an X-Y recorder, and temperature control system for heating and cooling. By properly changing the experimental parameters it is possible to measure the following parameters:

- The minority and majority carrier traps.
- The activation energy of each defect level.
- The defect concentration which is directly proportional to the peak height.
- The defect concentration profile.
- The electron and hole capture cross-sections for each trap.

7.4.1 Principles of the DLTS technique

The capacitance transient is associated with the return to thermal equilibrium of the carrier occupancy in a trap level following an initial nonequilibrium condition. The polarity of the DLTS peak depends on the capacitance change after trapping the minority or majority carriers. Because an increase in trapped minority carriers in the SCR would result in an increase in the junction capacitance, the minority carriers trapping will produce a positive polarity peak, and vice versa. For example, in a p^+n junction diode, the SCR extends mainly into the n-region, and the local charges are due to positively charged ionized donors. If a forward bias is applied, the minority carriers (holes) will be injected into this region. Once the holes are trapped in a defect level, the net positive charges in such region will increase. This results in a narrower SCR width which implies a positive capacitance change. Thus, the DLTS signal will have a positive peak. Similarly, if the majority carriers are injected into this region and captured by the majority carrier traps, which reduces the local charges, the SCR width will be wider, implying a decrease of the junction capacitance. Therefore, the majority carriers trapping will result in a nagative DLTS peak. The same argument can be applied to the n^+p junction diodes. All of the samples used in the DLTS measurements are p^+n diodes so that a positive peak represents the hole trap, and a negative peak represents the electron trap.

7.4.2 Minority carrier injection

Fig. 7.5 shows the injection of minority carriers. Fig. 7.5(a) is the injection pulse where $V = V_p > 0$ during the pulse ($t_a < t < t_b$) and $V = V_R < 0$ outside the time interval (t_a, t_b). Fig. 7.5(b) is a simplified energy band diagram (the band bending due to the junction electric field is omitted) in quiescent reverse bias condition ($t < t_a$). Fig. 7.5(c) is the saturation injection pulse ($t_a < t < t_b$). During the pulse, the minority carrier traps E_t are filled by holes. Fig. 7.5(d) is the transient process during the period ($t > t_b$); the trapped hoes begin to emit from the trap centers to valence band and then swept out of the SCR by the built-in electric field that causes the capacitance transient.

7.4.3 Majority carrier injection

Fig. 7.6 shows the injection of majority carriers. Fig. 7.6(a) is the injection pulse where $V = V_p = 0$ during the pulse ($t_a < t < t_b$) and

$V = V_R < 0$ outside the time interval (t_a, t_b). Fig. 7.6(b) is a simplified band diagram in quiescent reverse bias condition ($t < t_a$). Fig. 7.6(c) is the majority carrier injection. During the pulse period ($t_a < t < t_b$), the majority carriers were injected into the SCR and captured by the majority trap. Fig. 7.6(d) is the transient process for the period ($t > t_b$) in which the captured electrons begin to emit from the trap centers to conduction band and then swept out of the SCR by the built-in electric field, resulting in the observed capacitance transient.

7.4.4 Trap concentration

The defect concentration is directly proportional to the peak height as described before, and the peak height is proportional to the capacitance change $\Delta C(0)$ [$\Delta C(0)$ is shown in Figs. 7.5(d) and 7.6(d)]. Therefore, the defect concentration N_t is proportional to $\Delta C(0)$ to be derived as follows: Let $C(t)$ be the capacitance transient [64,65] which is proportional to the electron (hole) emitted to the conduction (valence) band. Then

$$
\begin{aligned}
C(t) &= A\{q\varepsilon_s[N_D - N_t \exp(-t/\tau)]/[2(\phi_i + V_r + kT/q)]\}^{1/2} \\
&= C_o\{1 - [N_t \exp(-t/\tau)/N_D]\}^{1/2} \qquad (7.13)
\end{aligned}
$$

where t is time; τ is the carrier emission time constant; $C_o = C(V_r)$, as shown in Eq. (7.7), is the junction capacitance at the quiescent reverse bias condition. For $N_t/N_d \ll 1$, Eq. (7.13) reduces to a simple form as:

$$C(t) = C_0[1 - N_t \exp(-t/\tau)/2N_D] \tag{7.14}$$

Eq. (7.14) can be rewritten as

$$N_t \exp(-t/\tau) = [2\Delta C(t)/C_0] \cdot N_D \tag{7.15}$$

where $\Delta C(t) = C_0 - C(t)$. From the DLTS technique, $\Delta C(0)$ can be measured. The junction capacitance C_0 and the background concentration can be obtained from C-V measurements. Thus, the defect concentration N_t can be calculated easily by using Eq. (7.15) at $t = 0$.

7.4.5 Activation energy of a deep level trap

As shown in Fig. 7.7, $\Delta C(t)$ begins to decay after the injection pulse is over. The decay associates with a specific time constant which is equal to the reciprocal of the emission rate. For an electron trap, the emission rate "e_n" is a function of temperature, coefficient and activation energy, and can be expressed by [11,66]

$$e_n = (\sigma_n \langle v_{th} \rangle N_c/g) \cdot \exp[(E_c - E_t)/kT] \tag{7.16}$$

where E_t is the activation energy of the trap; g is the degeneracy factor; σ_n is the electron capture cross-section which is temperature dependent [67]

$$\sigma_n = \sigma_\infty \cdot \exp(-\Delta E_b/kT) \tag{7.17}$$

where σ_∞ is the capture cross-section at very high temperature; ΔE_b is activation energy of the capture cross-section for the trap. e_n can be written as

$$\begin{aligned} e_n &= BT^2 \cdot \exp \{[E_c - (E_t + \Delta E_b)]/kT\} \\ &= BT^2 \cdot \exp [(E_c - E_m)/kT] \end{aligned} \tag{7.18}$$

where B is the proportionality constant and is independent of temperature. From this relation, e_n increases with increasing temperature. The capacitance transient is rearranged from Eq. (7.14) as

$$\begin{aligned} C(t) &= C_o(N_t/2N_D) \cdot \exp(-t/\tau) \\ &= \Delta C(0) \cdot \exp(-t/\tau) \end{aligned} \tag{7.19}$$

where $\tau = e_n^{-1}$. Eq. (7.19) implies a faster decay of $\Delta C(t)$, as is shown in Fig. 7.6, at high temperature and a smaller decay time constant which implies a faster decay of $\Delta C(t)$ as shown in Fig. 7.6. The same argument can also be applied to the hole trap. The only difference is that $\Delta C(t)$ has an opposite polarity.

The following is the procedures to deduce the activation energy of a defect level. We first set t_1 and t_2 in a dual-gated integrator boxcar, then we write

$$C(t_1) = C(0) \cdot \exp(-t_1/\tau) \tag{7.20}$$

$$C(t_2) = C(0) \cdot \exp(-t_2/\tau) \tag{7.21}$$

The DLTS scan along the temperature axis is obtained by taking the difference of Eq. (7.20) and (7.21) which yeilds:

$$S(T) = \Delta C(0)[\exp(-t_1/\tau) - \exp(-t_2/\tau)] \tag{7.22}$$

The maximum emission rate, τ_{max}^{-1}, is obtained by differentiating S(T) with respect to τ, and let it equal zero [$dS(T)/d\tau = 0$]. The result yields:

$$\tau_{max} = (t_1 - t_2)/\ell n(t_1/t_2) \tag{7.23}$$

Under this condition, S(T) reaches its maximum value at a specific temperature. The emission rate is given by $e_n = 1/\tau_{max}$ for each t_1 and t_2 setting. By changing t_1 and t_2 several times, a set of temperatures corresponds to this set of τ_{max} (or emission rate e_n) can be obtained. From the Arrhenius plot [i.e., $\ell n(e_n/T^2)$ vs. $1/kT$], the activation energy of the trap can be calculated from the slope of this plot.

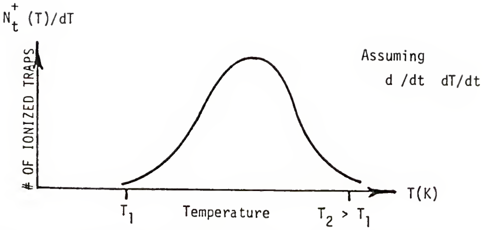

Figure 7.1 Rate of ionized traps vs. a linear temperature increase.

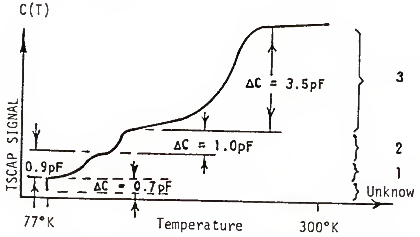

Figure 7.2 Typical TSCAP linear temperature scan of a Schottky diode.

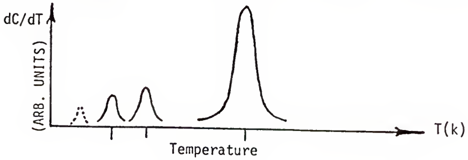

Figure 7.3 dC/dT (derivative) vs. temperature of Figure 7.2 showing the three trap peaks to give additional visibility and resolution over the TSCAP plot.

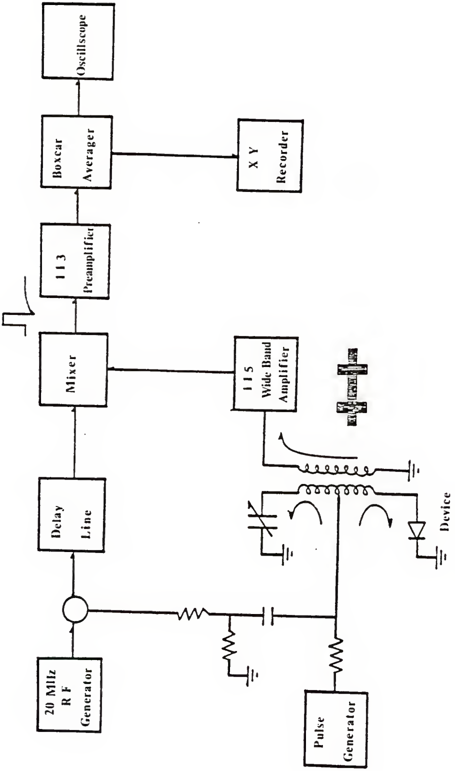

Figure 7.4 The block diagram of the DLTS.

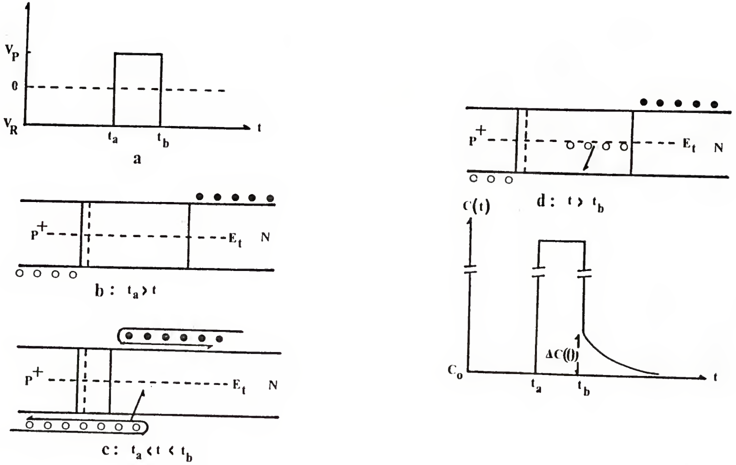

Figure 7.5 The process of minority carrier injection.

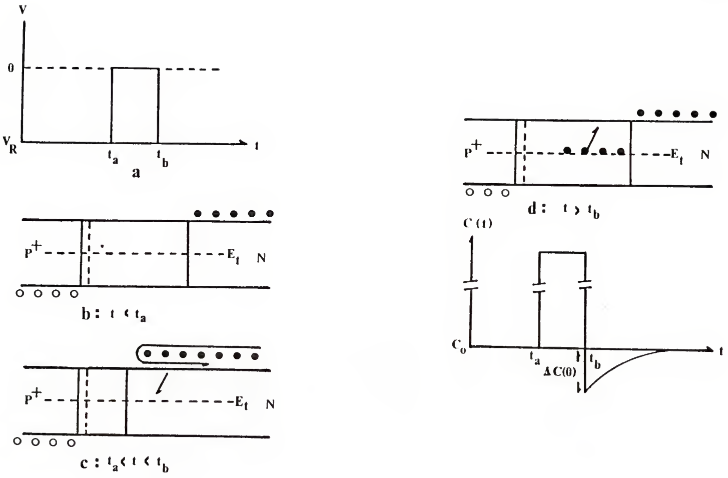

Figure 7.6 The process of majority carrier injection.

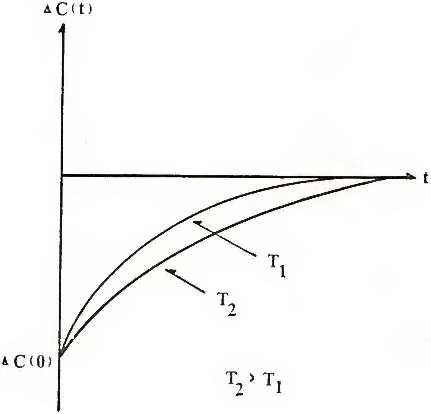

Figure 7.7 The transient capacitance decay exponentially after the injection pulse is over. The higher temperature corresponds to the smaller decay time constant.

CHAPTER VIII
THE EFFECTS OF METALLIC CONTAMINATION ON THE DEVICE PERFORMANCE

8.1 Introduction

In the IC fabrication, the unintentional metallic contamination may introduce into silicon substrate during high temperature processes. Most of these metallic contamination is associated with the transition metals.

The 3d transition metals such as Ti and Ni, and the noble metals such as Cu, Ag, and Au will diffuse interstitially into silicon and stay predominantly in these sites during high temperature processes. These impurities may introduce deep donor level or deep acceptor centers in silicon [68]. In bipolar devices, these deep levels may act as recombination centers under forward bias condition. The effect would be to reduce the current gain of a transistor, or to decrease its switching time. In a reverse biased p-n junction, these deep level traps act as current generation centers, and increase reverse leakage and noise in a p-n diode, or a transistor. Thus, the knowledge about the behavior and the influence of various transition metal impurities in a semiconductor, especially in silicon, is very important for improving the device performance.

The process-related defects in silicon has been actively investigated by many researchers [68-72]. Benton and Kimerling [71] use the capacitance transient spectroscopy monitors electrically active defects in the depletion region of a p-n junction. They recorded the capacitance transient spectra for metallic impurities in silicon and correlated it with sample spectra to identify trace contamination in the tested devices. The DLTS exhibits a characteristic thermal scanning peak for each defect. A complete DLTS analysis determines the defect state concentration, the activation energy for the trap levels, the carrier capture cross section, and the depth distribution of the defect in a semiconductor. Values of of activation energy E_T and majority carrier capture cross section (σ) give a unique set of parameters for each defect. Thus, from the DLTS spectra and the measured defect parameters one can determine the specific impurities present in each device [71].

In this chapter, studies of metallic contamination in low noise silicon JFET's are presented. Experimental tools employed in this study include the current voltage (I-V), capacitance voltage (C-V), thermally stimulated capacitance (TSCAP) and deep-level transient spectroscopy (DLTS) measurements. The correlations among the trap density, the reverse leakage current, and the 1/f noise are also investigated.

The device structures used in this study are described in section 8.2. Experimental results obtained from the I-V, C-V, TSCAP, and DLTS measurements on vertical P/N and N/P diodes as well as the MOS capacitors built on N- and P-collectors are presented and discussed in section 8.3. Section 8.4 gives the summary and conclusions.

8.2 Tested devices and structures

The large area junction diodes and MOS capacitors used in ths study are fabricated from ion-implanted JFETs process (run #JFET2-1358) and found on the test mask set shown in Figure 8.1. The large area junction diodes are illustrated in Figure 8.2 and 8.3. Figure 8.2 is a large PN junction structure, either N diffused into P or P diffused into N, with a maximum bottom plate area and a minimum sidewall area. The structure shown in Figure 8.3 differs from Figure 8.2 in that it has a maximum sidewall area and a minimum bottom plate area. Figure 8.2 is referred to as a bottom plate (BP) diode structure, while Figure 8.3 is referred to as a sidewall (SW) diode structure.

Table 8.1 summarized the tested devices showing their structures and applications. Figure 8.4 illustrates the cross-sectional view of the four diode structures D1, D2, D3, and D4. Two MOS capacitor structures are shown in Figure 8.5.

Several die from wafers of the JFET2-1358 run were characterized in this study. The group B diodes from die B-5 and B-8, are bonded out from the N^+/P_b BP, N^+/P_b SW and P^+/N_b BP diodes. The group C diodes from die C-9 and C-10 are bonded out from the N_b/P_c BP, N_b/P_c SW and P_b/N- and P_c bottom plates. The P2P1 parts are bonded out from the N_b/P_c BP and P_b/N- BP diodes.

8.3 Experimental observation

In this section, the experimental results obtained from the metallic contamination study in the devices from JFETS runs are discussed.

8.3.1 Results and discussions on group B (P1PB) diodes

The forward I-V characteristics of both B-5 and B-8 N^+/P_b BP diodes, N^+/P_b SW diodes, P^+/N_b SW and P^+/N_b BP diodes are shown in Figures 8.6 and 8.7 with good diode ideality factors ranging from 1.03 to 1.12. However, the reverse I-V characteristic curves, see Figure 8.8, show a large variation in leakage current, as much as five orders of magnitude, between diodes made from the same diffusion on two different die. Figure 8.8 shows that the N^+/P_b SW and the N^+/P_b BP diodes from the B-5 group have the highest leakage, followed by the P^+/N_b BP diodes from the group B-5 and B-8 diodes. The N^+/P_b SW and BP diodes from the B-8 die have the lowest reverse leakage current.

C-V measurements were made on N^+/P_b BP and SW diodes and P^+/N_b BP and SW diodes, and the results are shown in Figures 8.9 and 8.10. The dopant density in the base region of these diodes was determined from $1/C^2$ vs. V_R plots and the results are summarized in Table 8.2 and 8.3. The dopant density was found to vary from 2×10^{15} cm^{-3} in the N_c region to 5×10^{17} cm^{-3} in the N_b region.

Deep-Level Transient Spectroscopy (DLTS) measurements on several group of diodes were carried out. The N^+/P_b BP and SW diodes on the B-8 die had relatively low reverse leakage current as compared to the same diodes on the B-5 die as is seen in Figure 8.8. The higher reverse leakage current observed in the B-5 N^+/P_b BP and SW diodes was attributed to the presence of metallic contaminants at the surface of this diode. If this were true, the DLTS measurements on the B-5 diode should have indicated a higher defect density than was found on the B-8 diode. DLTS scans performed on N^+/P_b diode from both the B-5 and B-8 die indicate the presence of two hole traps in both the B-5 and B-8 N^+/P_b BP diodes. Figure 8.11 shows the DLTS scan of the B-5 N^+/P_b BP diode. The first hole trap, denoted as H2, has its energy level at E_V + 0.47 eV. The second hole trap, denoted as H4, has its energy level at E_V + 0.8 eV. The trap density of the H2 is 10^{14} cm^{-3}, and is about the same for both the B-5 and B-8 diodes. H4 is the dominant trap in both the B-5 and B-8 diodes. The density of the H4 trap in the B-5 diode is 5 x 10^{14} cm^{-3}. In the B-8 diode, the H4 trap was found to be located near the surface region of the diode at a depth of less than 0.7 µm.

In summary, the I-V, C-V and DLTS measurements on the diodes from the B-5 and B-8 dies from JFET2-1358 run show good correlation between reverse leakage current and the density of the corresponding metallic contaminants.

8.3.2 Results and discussion on phase 1 group C (P1PC) diodes

I-V, C-V and DLTS measurements were performed on some of the group C diodes, and the results are shown in Figures 8.12 through 8.19. The reverse I-V characteristics curves shown in Figure 8.13 indicate that the N_b/P_c BP diodes have consistently higher reverse leakage than the P_b/N- BP diodes on the same die. The high reverse leakage current is attributed to an induced n-channel being formed in the lightly doped P collector.

C-V and DLTS measurements were performed on the C-10 N_b/P_c BP and P_b/N- BP diodes, and the results are shown in Figures 8.14 through 8.19. Both the majority carrier (electron) traps in the N- and the majority carrier (hole) traps in the P_c were analyzed and identified. In the C-10 P_b/N- BP diode, two electron traps were identified (See Figs. 8.15-8.17). The first electron trap E1 has an energy level of E_c-0.19 eV and a density of 1.7 x 10^{12} cm^{-3}. The second electron trap E2 has an energy level of Ec - 0.56 eV and a density of 9.3 x 10^{13} cm^{-3}. Since the N- dopant density is one-tenth of the P_b dopant density, the observed electron traps E1 and E2 should be in the N- side of the junction.

Two shallow hole traps were observed in the C-10 N_b/P_c BP diodes as is shown in Figure 8.18. The first hole trap H1 has an energy level of Ev + 0.22 eV and a trap density of 7.3 x 10^{13} cm^{-3}. The energy level of the second hole trap H3 is E_V + 0.66 eV (see Figures 8.18 and 8.19). Table 8.4 shows the electron and hole traps observed in JFET 2-1358 run P1PB and P1PC diodes. A summary of the deep-level defects observed in P1PB and P1PC diodes is given in Table 8.5.

8.3.3 Results and discussion on phase 1 group D (P1P2) MOS capacitors

The results of the C-V, TSCAP and DLTS measurements on group D MOS capacitors from JFET2-1358 (die #13, #15, and #18) run are presented in this section.

C-V measurements vs. temperature (77 to 350 K) and frequency (1 MHz to 50 MHz), Thermally-Stimulated-Capacitance (TSCAP) and Deep-Level-Transient-Spectroscopy measurements were performed on the phase 1 group D MOS capacitors with N-substrate.

The results are quite interesting, and conclusions obtained from this study are consistent with the results obtained from the DLTS data on group B and group C P-N diodes concerning the metallic contaminants discussed above. The results of our analysis on the C-V, TSCAP and DLTS data for group D MOS capacitors with N- substrate are summarized as follows:

(1) The frequency dependence of C-V curves: Fig. 8.20 shows the C-V plots for device #18 for four different frequencies (i.e., 1, 5, 10, 20 MHz), respectively. It is noted that in the accumulation region (i.e., V > 0) the insulator (i.e., oxide) capacitance depends strongly on frequency (decrease with increasing frequency). To explain this result, Fig. 8.21 shows the equivalent circuit of an MOS capacitor including interface trap states and depletion capacitance; C_s and R_s are associated with the interface trap density. The product R_sC_s is defined as the interface-trap lifetime, which determines the frequency behavior of the interface traps. C_i and R_i are the oxide capacitance and oxide shunt resistance (which is infinity for ideal case), respectively. The reduction in equivalent capacitance with frequency in the accumulation region is due to the effect of R_i, R_s or both. The most interesting result shown in Fig. 8.20 is the hysteresis loops observed in the inversion region of the C-V plots. At a reverse bias voltage of -20 V, the donor states in the space charge region become positively charged due to the emission of electrons from the deep donor traps (as will be explained later in the DLTS and TSCAP data), and increases drastically to a maximum capacitance determined by the trap

density. This effect is more pronounced at 1 MHz than at other higher frequencies, and diminishes at 20 MHz in which the trap states can no longer follow the ac signal (i.e, $R_S C_S$ time constant is too large). The results also showed that the capacitance of these MOS capacitors becomes constant and independent of bias voltage, implying that the interface traps and depletion capacitance are negligible at very high frequencies. Fig. 8.22 shows the frequency dependence of C-V curves for an MOS capacitor on p-collector substrate at 300 K for four different frequencies. It is noted that in contrast to the MOS capacitor built on the n- subtrate shown in Fig. 8.20 negligible hysteresis loops were observed in the MOS capacitor built on the p- collector substrate.

(2) The temperature dependence of the C-V curves: The hysteresis loops observed in the inversion region of the C-V curves at 300 K shown in Fig. 8.20 disappear for temperatures below 250K (see Fig. 8.23); this is due to the freeze-out of the donor traps (which become neutral states). Fig. 8.24 shows the C-V curves vs. frequency (2 to 20 MHz) for capacitor #18 at 77 K. It is clearly shown that the C-V curves are quite normal with no hysteresis loops observed in all the frequency ranges studied. Thus, from the temperature dependence of the C-V characteristics curves it is obvious that the hysteresis effect observed in these MOS capacitors is due to the donor traps located at the surface of the N-substrate.

(3) Thermally-Stimulated-Capacitance (TSCAP) measurements: In order to explain the physical reasons for causing the observed hysteresis loops shown in Fig. 8.20 and Fig. 8.24, the TSCAP experiment was made on device #18. Fig. 8.25 shows the TSCAP scans for #18 MOS capacitor from 150 K to 350 K at 1 and 3 MHz. The solid lines are for the 1 MHz results, and the broken lines are for the 3 MHz results. The curves shown can be explained as follows: If the capacitor is reverse biased at -20 V initially, and cooled down from room temperature to liquid nitrogen, and is then warmed up to room temperature under the same reverse bias condition as the initial condition, we should see the result (upper solid curve) shown in this figure. If the capacitor is initially positively biased so that all traps were filled by electrons, then the TSCAP scan should reveal trap information from a single TSCAP scan. This is shown in the lower solid curve of the C-V plot. A big step change in the capacitance was observed in device #18 for T > 250 K. This capacitance step is a result of the electron emisson from the donor trap states at the Si-SiO$_2$ interface or near the silicon surface. The broken lines are the TSCAP scans taken on the same MOS device at 3 MHz frequency. Note that the change in capacitance at the onset of the thermal emission and at the end of electron emission is directly related to the density of the electron trap via the relation:

$$N_t = (2\Delta C/C_o)N_D \qquad (8.1)$$

The density of electron trap determined by the above formula and ΔC and C_o shown in Fig. 8.25 is found equal to 3 x 10^{15} cm^{-3}. Fig. 8.26 shows a similar TSCAP scan of the same MOS capacitor performed at 2 MHz and at a reverse bias voltage of -5 V. It is noted that two capacitance steps were observed in this plot between 250 and 280 K, indicating that there are two electron traps located very closely in energy in this temperature range. This is verified by the DLTS scan to be discussed next.

(4) The DLTS scan of electron traps was also made in #18 MOS capacitor, and the result was shown in Fig. 8.27. Two electron traps with energies of 0.4 and 0.56 eV were observed in this capacitor, and both are found to be donor type traps. These donor type traps are formed due to the metallic contamination in the tested devices.

8.3.4 Results and discussion on phase 2 part 1 (P2P1) diodes

The measured results of D3 and D4 diodes in phase 2 part 1 (P2P1) units selected from run JFET2-1358 are shown in Table 8.6 and 8.7, Figures 8.28 through 8.31. Table 8.6 and 8.7 summarize the experimental results for the H3 (Ev + 0.66 eV) and E2 (Ec - 0.56 eV) traps observed in the tested D3 and D4 diodes. The trap densities for the H3 and E2 traps are in the range of 4.1 x 10^{13} cm^{-3} and 1.9 x 10^{13} to 3.9 x 10^{13} cm^{-3}, respectively. Note that the measured trap density for the H3 and

E2 levels was lower than those observed in the units reported in our phase 1 study. The reason for this difference has been attributed to the reserve implant procedure used in these two units.

The reverse I-V curves for D3 diodes of unit #14, #19 and #15 selected from run JFET2-1358 P2P1 wafer lots are shown in Fig. 8.28, in which D3 diode from unit #14 was found to have the highest leakage current among the diodes tested. It is noted that #14, D3 diode was also found to have the highest H3 trap density. Fig. 8.29 shows the results of the C-V measurements for unit #14 for D3 and D4 diodes, respectively, for frequencies of 1 MHz and 20 MHz. The results of C-V measurements on diodes D3 and D4 showed that the capacitance values for D3 depend strongly on frequency but little dependent of frequency for D4 diode. It is probably because the D4 diode has low E2 trap density.

The DLTS scan of main hole trap H3 and main electron trap E2 in the D3 and D4 diodes from JFET2-1358 wafer lots are also shown in Figs. 8.30 through 8.31, respectively.

In order to find the correlation between the metallic contaminants induced hole trap density and the 1/f noise in seven NPN and PNP transistors as well as JFETS from JFET2-1358 run, the 1/f noise were measured in Harris on devices in which DLTS and C-V measurements have also been made. The results of the 1/f noise measurements at five different frequencies (i.e, 10, 100, 1K, 10K, and 100K) on seven npn and pnp transistors as well as JFETs are listed in table 8.8, 8.9, and 8.10. Note that the highest leaky device is listed at the top of table 8.8, 8.9, and 8.10, while the lowest leaky device is listed at the bottom of the table. From this table it is clearly shown that there is good correlation between the hole trap density (Ev + 0.66 eV hole trap) and the leakage current. However, it should be noted that the noise figures for both the NPN transistors and the JFETs are not closely related to the defect density deduced from the DLTS data. The only good correlation obtained among the leakage current, trap density, and the 1/f noise figures are those deduced from the PNP transistors, as is shown in Table 8.9. In order to find a better correlation between the noise figures and trap density due to metallic contamination, it is necessary to perform the noise measurements at frequencies below 10 Hz.

8.4 Summary and conclusion

From the analysis of the I-V, C-V, TSCAP, and DLTS data on the P/N and N/P diodes and MOS capacitors from the JFET2-1358 run, we reach the following conclusions:

(1) The metallic contaminants presented in these tested devices introduce several deep level hole and electron traps. The main hole trap is due to the Ev + 0.66 eV level and the main electron trap is due to the Ec - 0.56 eV level with the average trap density in the low to mid 10^{14} cm^{-3} range. The surface concentration of these traps is expected to be much higher than the value measured. If the hole trap is a donor type defect, it will have a detrimental effect on the low-doped p-type surface since an n-inversion layer may be formed by a large density of such hole trap contaminated at the surface, resulting in a large surface leakage current in this n-channel inversion layer. This is indeed the case for the lateral N^+/P diodes such as B-5 and C-10 diodes studied here.

(2) The reverse I-V characteristics were found closely related to the DLTS results in that the vertical junction diodes showed very little leakage current and smaller density of metalllic contaminant while the lateral N+/P diodes showed a very large surface leakage current and a large density of surface defect density. As for the lateral P^+/N diodes, the surface leakage current was moderate when compared to the lateral N^+/P diodes. This is due to the fact that N-surface will not be inverted by the donor-type metallic contaminants while an n-inversion channel may be formed in the lightly doped p-surface layer by the metallic contaminant.

(3) The results of our C-V, TSCAP, and DLTS measurements on #18 MOS capacitor are quite interesting and clearly show that a majority donor type electron trap located at the Si-SiO_2 interface plays a key role in influencing the temperature and frequency dependence of the high frequncy C-V behavior in this MOS capacitor. The density of this donor trap is very large (of the order of 1×10^{15} cm^{-3}), and is believed to have a substantial effect on the 1/f noise observed in the JFET devices fabricated from JFET2-1358 run. The donor trap observed in this MOS capacitor is believed to be due to the same electron trap we observed in the lateral P/N diode (C-10) discussed earlier. Thus, this donor type electron trap may be related to the metallic contaminants shown in Table 8.5.

(4) Since all the electron and hole traps observed in the diodes and MOS capacitors from implanted JFET wafer lots are donor-like traps, it is expected that p-silicon surface is more likely to be inverted than the n-silicon surface. Therefore, an n-type inversion channel can be easily formed in a lateral N^+/P diode, resulting in a larger leakage current and 1/f noise in such a device.

(5) The hysteresis loops observed in the C-V scans for some of the MOS capacitors from the implanted JFET wafer lot can also be attributed to the trap states introduced by the metallic contaminants at the $Si-SiO_2$ interface, in which the emission of electrons from the electron traps at a characteristic temperature results in the hysteresis behavior observed in the C-V plot.

(6) From the results presented in section 8.3.4, it is noted that there is a good correlation between the trap density and the reverse leakage current observed in the P2P1 devices, implying that the reverse leakage current observed in diodes assembled from JFET2-1358 run was due to the bulk generation recombination current stemmed from thermal generation and recombination via the electron and hole trap centers such as E2 and H3 traps reported above. As for the 1/f noise source, the results for the P2P1 devices shown in Table 8.8-8.10 are more random and scattered in nature, and showed only a certain degree of correlation to the density of metallic contaminants observed in these devices.

In short, this chapter presents the results of our studies of the effects of metallic contamination on the device performance. It helps us to obtain a better understanding concerning the correlation among the reverse leakage current, 1/f noise source, and the density of metallic contaminants determined by the C-V and DLTS measurements.

Table 8.1

List of the tested devices used in the metallic contamination study.

Phase 1	Part 1	Group B (P1Pb)	D1 (N^+/P_b) diode	B-5, B-8
			D2 (P^+/N_b) diode	
		Group C (P1PC)	D3 (N_b/P_C) diode	C-9, C-10
			D4 (P_b/N_-) diode	
	Part 2	Group D (P1P2)	MOS Capacitor	#13, #15, #18
Phase 2	Part 1 (P2P1)		D3 (N_b/P_C) diode	#6, #11, #14, #15, #18, #19 #20, #28, #31, #32, #34, #38, #39.
			D4 (P_b/N_-) diode	

Table 8.2

Results of the I-V and C-V measurements on Group B diodes.

DIE	PARAMETERS	N+/P_b BP	P^+/N_b BP	N^+/P_b SW
B-5	Diode Ideality Factor	1.05	1.06	1.06
	Base Concentration	2×10^{16}	9.7×10^{16}	2.6×10^{17}
B-8	Diode Ideality Factor	1.10	1.03	1.04
	Base Concentration	1.8×10^{16}	1.2×10^{17}	2.5×10^{17}

Table 8.3

Results of the I-V and C-V measurements on Group C diodes.

DIE	PARAMETERS	P_b/N- BP	N_b/P_c BP	N_b/P_c SW
C-9	Diode Ideality Factor	1.12	1.10	1.06
	Collector Concentration	2.1×10^{15}	1.1×10^{16}	1.3×10^{17}
C-10	Diode Ideality Factor	1.10	1.10	1.04
	Collector Concentration	2.0×10^{15}	1.2×10^{16}	1.0×10^{17}

Table 8.4

Electron and hole traps observed in P1PB and P1PC diodes from JFET2-1358 run.

DIODES	ELECTRON TRAPS		HOLE TRAPS	
	$E_C - E_T$ (eV)	N_T (cm^{-3})	$E_V - E_T$ (eV)	N_T (cm^{-3})
B-5 N^+/P_b BP			H2 = 0.47	1.0×10^{14}
			H3 = 0.66	1.0×10^{14}
			H4 = 0.83	5.0×10^{14}
B-8 N^+/P_b BP			H2 = 0.47	1.0×10^{14}
			H3 = 0.66	1.0×10^{14}
			H4 = 0.83	1.0×10^{14}
C-10 P_b/N_- BP	E1 = 0.19	1.7×10^{12}		
	E2 = 0.56	1.0×10^{14}		
C10 N_b/P_c BP			H1 = 0.22	7.3×10^{13}
			H3 = 0.66	5.3×10^{14}
			H4 = 0.83	8.9×10^{13}

Table 8.5

Summary of deep-level defects observed in the P1PB and P1PC diodes.

JFET DEVICES				
DEFECTS	E_T(eV)	DLTS PEAK (K)	e_n or e_p (s^{-1})	σ_n or σ_p (cm^2)
Fe	E1 = Ec- 0.19	138	555.6	7×10^{-17}
(Au, Co, Ti)	E2 = Ec- 0.56	295	555.6	1.2×10^{-16}
Fe	H1 = Ev+ 0.22	152	86	1.4×10^{-16}
Fe	H2 = Ev+ 0.47	217	277	9×10^{-13}
	H3 = Ev+ 0.66	334	86	1.2×10^{-14}
	H4 = Ev+ 0.8 ~ 0.86	369	86	4.7×10^{-13}

Table 8.6

Defect density and background dopent density for the N_b/P_c and P_b/N_c diodes from JFET2-1358 processes.

*Device	Parameters	Background Density (cm^{-3})	Trap Density (cm^{-3})
#14 (red) (high)	N_b/P_c P_b/N_c	1.03×10^{16} 2.7×10^{15}	$^{\$}H3 = 1.07 \times 10^{14}$ $^{\&}E2 = 2.2 \times 10^{13}$
#15 (red) (low)	N_b/P_c P_b/N_c	1.23×10^{16} 3.0×10^{15}	$H3 = 4.8 \times 10^{13}$ $E2 = 1.9 \times 10^{13}$
#19 (blue) (medium)	N_b/P_c P_b/N_c	1.03×10^{16} 3.1×10^{15}	$H3 = 6 \times 10^{13}$ $E2 = 2.2 \times 10^{13}$
#32 (blue) (high)	N_b/P_c P_b/N_c	9.8×10^{16} 2.86×10^{15}	$H3 = 9.13 \times 10^{13}$ $E2 = 3.3 \times 10^{13}$
#38 (green) (medium)	N_b/P_c P_b/N_c	1.07×10^{16} 3.0×10^{15}	$H3 = 8.1 \times 10^{13}$ $E2 = 3.9 \times 10^{13}$
#39 (green) (high)	N_b/P_c P_b/N_c	1.09×10^{16} 2.7×10^{15}	$H3 = 1.03 \times 10^{14}$ $E2 = 3.4 \times 10^{13}$

* Area: 1.652×10^{-3} cm^2

\$ H3: $E_V + 0.66$ eV

& E2: $E_C - 0.56$ eV

Table 8.7

Leakage current levels and hole trap density for the N_b/P_c diodes from JFET2-1358 processes.

* Device Parameter	#6	#11	#18	#20	#28	#31	#34
Level of leakage	Low	Medium	High	Medium	High	Low	Low
Hole trap (H3) Trap Density (cm^{-3})	4.1×10^{13}	7.2×10^{13}	1.2×10^{14}	8.4×10^{13}	1.1×10^{14}	4.7×10^{13}	5.4×10^{13}

* D3 (N-base/P-collector), Area = 1.65×10^{-3} cm^2, Pc = $1.\times 10^{16}$ cm^{-3}.

& H3 = $E_v + 0.66$ eV.

Table 8.8

Hole trap density, leakage current and 1/f noise data for P2P1 NPN transistors from JFET2-1358 run.

SN	Leak rank (Hi to Lo)	Hole density (cm^{-3})	Vnpn e_n $(nV/(Hz)^{1/2})$					Vnpn i_n $(pA/(Hz)^{1/2})$				
			10	100	1K	10K	100K	10	100	1K	10K	100K (Hz)
#18	47.9	12×10^{13}	4.4	3.4	3.0	3.3	3.4	2.87	1.76	0.58	0.47	1.11
#28	48.1	11×10^{13}	5.4	3.2	3.0	3.3	3.4	6.48	1.76	0.54	0.51	1.19
#20	102	8.4×10^{13}	4.5	3.1	3.0	3.3	3.4	4.08	1.24	0.42	0.44	1.02
#11	104	7.2×10^{13}	4.4	3.1	3.1	3.3	3.5	2.57	2.37	0.56	0.47	1.11
#34	125	5.4×10^{13}	4.5	3.1	2.9	3.2	3.4	4.79	1.55	0.52	0.48	1.15
#31	127	4.7×10^{13}	4.1	3.1	3.0	3.3	3.4	2.67	1.02	0.41	0.44	1.07
#6	145	4.1×10^{13}	4.5	3.0	2.9	3.2	3.3	4.48	1.96	0.88	0.52	1.19

Table 8.9

Hole trap density, leakage of current and the 1/f noise data for P2P1 PNP transistors from JFET2-1358 run.

SN	Leak rank	Hole density	Vnpn e_n $(nV/(Hz)^{1/2})$					Vnpn i_n $(pA/(Hz)^{1/2})$				
	(Hi to Lo)	(cm^{-3})	10	100	1K	10K	100K	10	100	1K	10K	100K (Hz)
#18	47.9	12×10^{13}	4.0	2.4	2.3	2.35	2.55	12.0	2.98	1.2	0.81	2.06
#28	48.1	11×10^{13}	3.3	2.2	2.25	2.25	2.45	5.99	2.37	0.91	0.83	2.12
#20	102	8.4×10^{13}	4.2	2.8	2.3	2.3	2.5	12.0	4.79	0.99	0.83	2.15
#11	104	7.2×10^{13}	3.4	2.4	2.3	2.35	2.5	6.19	2.67	0.88	0.78	2.0
#34	125	5.4×10^{13}	3.3	2.4	2.25	2.3	2.45	6.79	2.88	0.93	0.82	2.12
#31	127	4.7×10^{13}	3.3	2.4	2.25	2.3	2.45	5.39	1.71	0.93	0.86	2.15
#6	145	4.1×10^{13}	3.4	2.3	2.3	2.35	2.5	5.49	1.96	0.8	0.69	1.78

Table 8.10

Hole trap density, leakage current and 1/f noise data for P2P1 JFETs from JFET2-1358 run.

SN	Leak rank (Hi to Lo)	Hole density (cm^{-3})	JFET e_n ($nV/(Hz)^{1/2}$)					
			10	100	1K	10K	100K	(Hz)
#18	47.9	12×10^{13}	140	85	50	20	10	
#28	48.1	11×10^{13}	165	100	60	22	11	
#20	102	8.4×10^{13}	205	115	64	23	11	
#11	104	7.2×10^{13}	130	82	49	21	10	
#34	125	5.4×10^{13}	190	100	59	21	10	
#31	127	4.7×10^{13}	150	100	64	21	10	
#6	145	4.1×10^{13}	140	99	57	22	11	

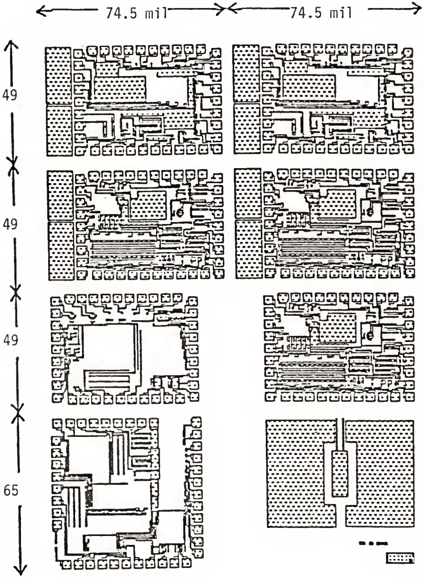

Figure 8.1 Photolithographic masks used in the fabrication of test devices for the I-V, C-V, and DLTS measurements.

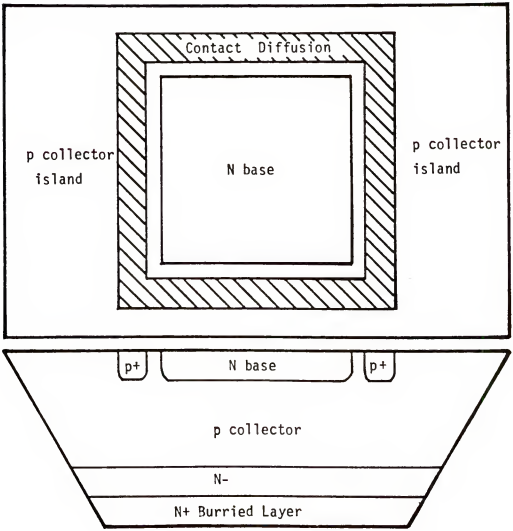

Structure Dimensions: N-base 16 mils x 16 mils

Figure 8.2 Test structure for a N_b/P_c bottom plate diode(BP).

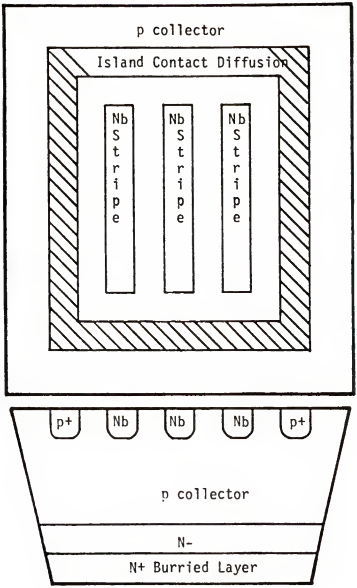

Structure Dimensions: N-base stripe 16 mils x 0.6 mils

Figure 8.3 Test structure for the N_b/P_c sidewall diode(SW).

D1 $(N+/P_b)$

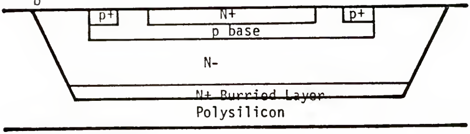

D2 $(P+/N_b)$

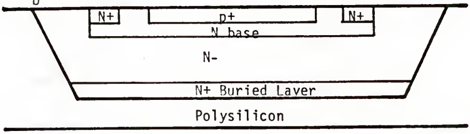

D3 (N_b/P_c)

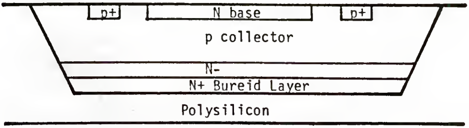

D4 $(P_b/N-)$

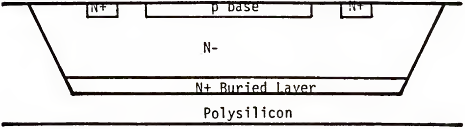

Figure 8.4 Cross sectional views of the D1, D2, D3, and D4 diodes.

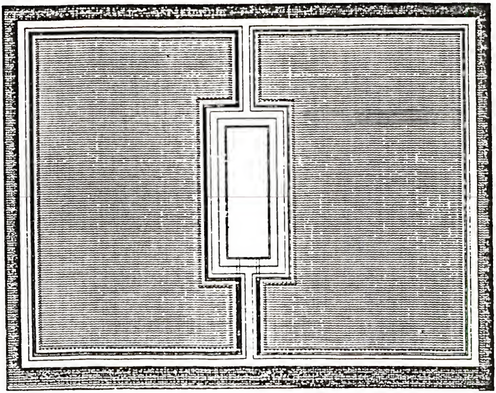

MOS CAPACITOR STRUCTURE

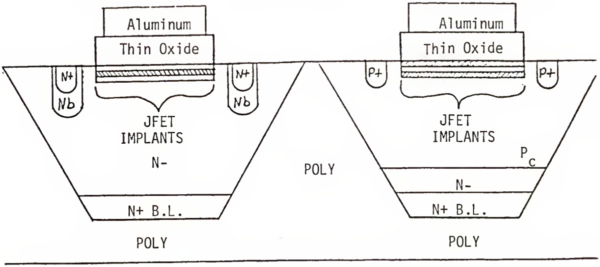

(Not To The Scale)

Figure 8.5 Top and cross sectional views of a MOS capacitor from #JFET 2-1358 run.

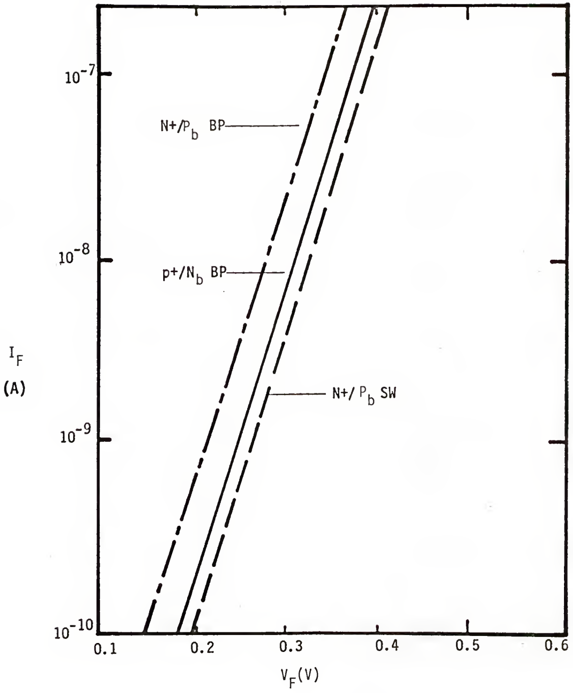

Figure 8.6 Forward current-voltage curves for three B-8 diodes selected from JFET 2-1358 (P1PB) run.

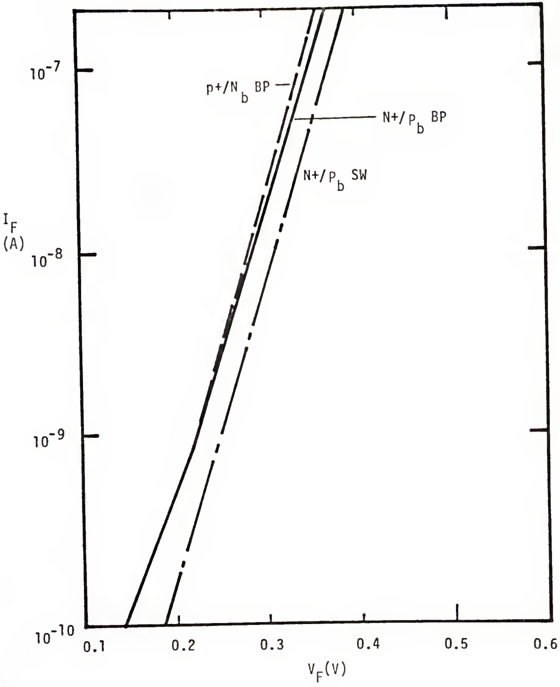

Figure 8.7 Forward current-voltage curves for three B-5 diodes selected from #JFET 2-1358 (P1PB) run.

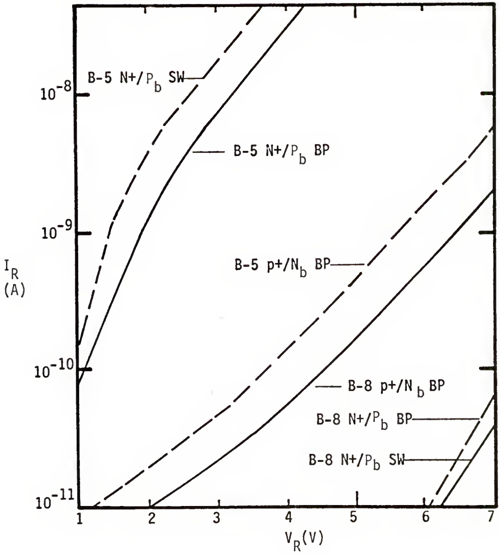

Figure 8.8 Reverse current-voltage curves for B-5 and B-8 diodes from #JFET 2-1358 (P1PB) run.

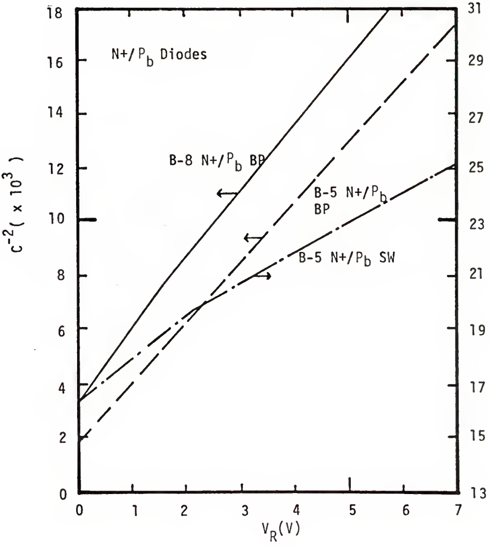

Figure 8.9 $1/C^2$ vs. V_R for B-5 and B-8 diodes from #JFET 2-1358 (P1PB) run.

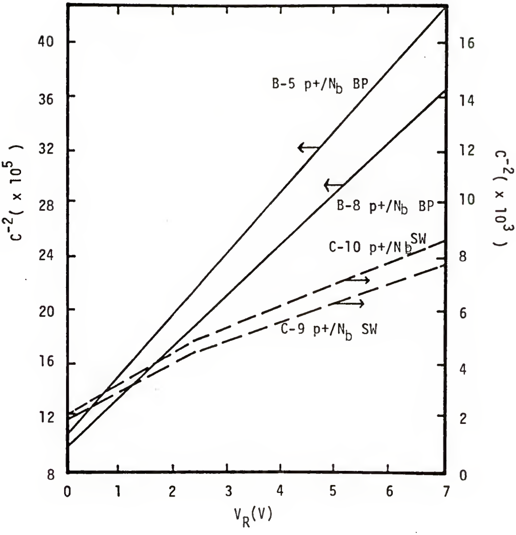

Figure 8.10 $1/C^2$ vs. V_R for group-B and -C diodes selected from #JFET 2-1358 (P1PB and P1PC) run.

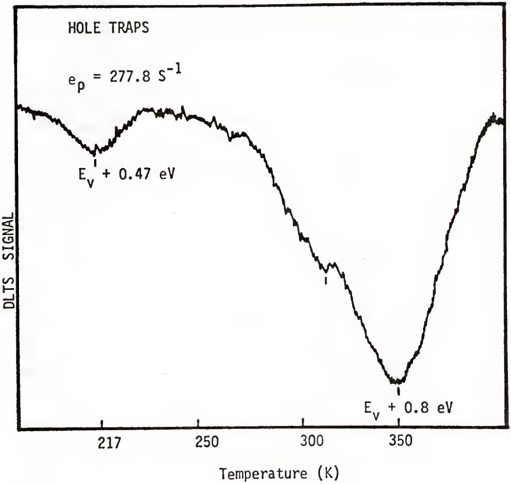

Figure 8.11 DLTS scan of hole traps in the B-5 N+/P_b BP diode selected from #JFET 2-1358 (P1PB) run.

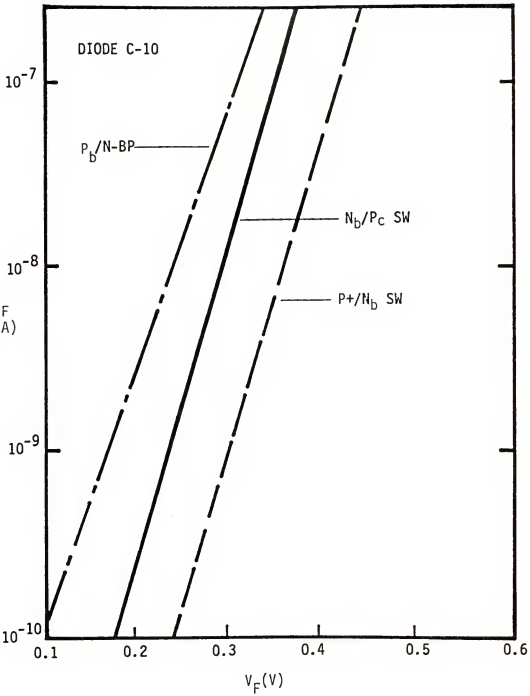

Figure 8.12 Forward I-V curves for C-10 diodes selected from #JFET 2-1358 (P1PB) run.

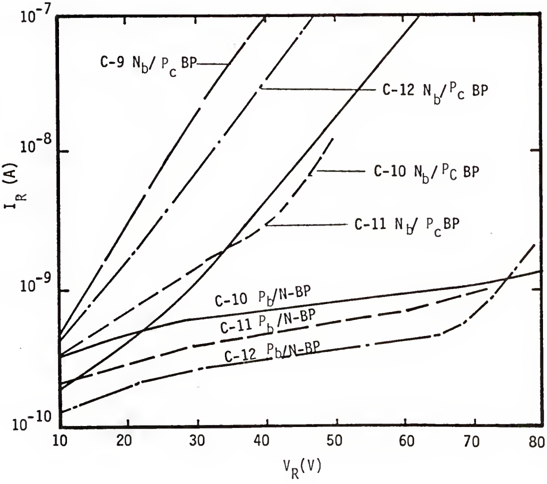

Figure 8.13 Reverse I-V curves for group-C diodes selected from #JFET 2-1358 (P1PC) run.

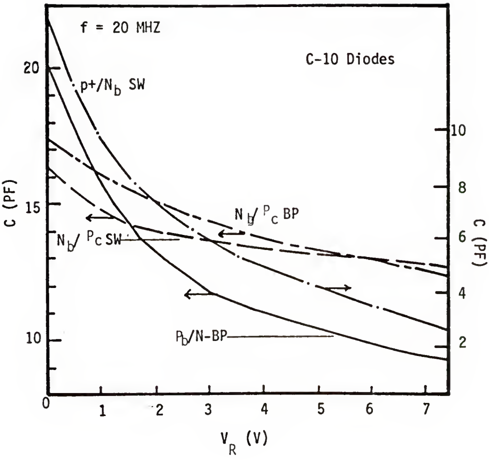

Figure 8.14 Capacitance-voltage curves for C-10 diodes measured at 20 MHz from #JFET 2-1358 (P1PC) run.

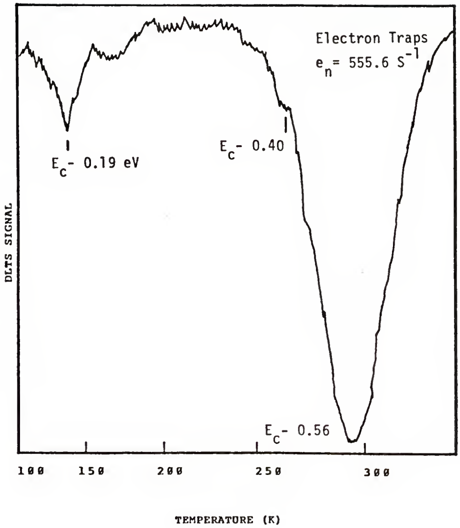

Figure 8.15 DLTS scan of electron traps in the C-10 P_b/N- BP diode selected from #JFET 2-1358 (P1PC) run.

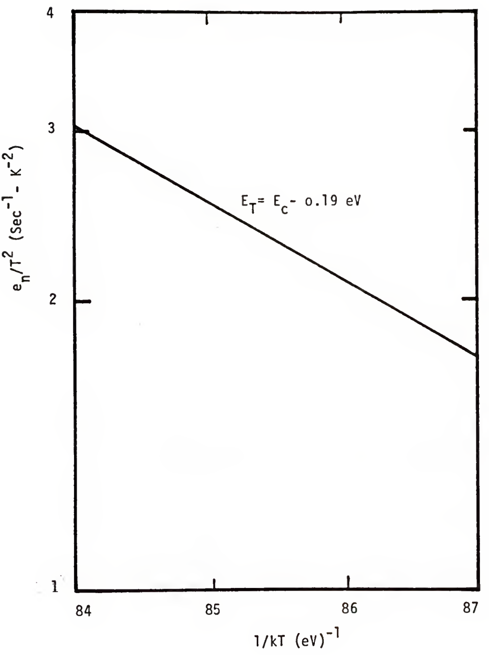

Figure 8.16 Thermal electron emission rates divided by T^2 vs. inverse of temperature for E1 electron trap in the C-10 P_b/N- BP diode selected from #JFET 2-1358 (P1PC) run.

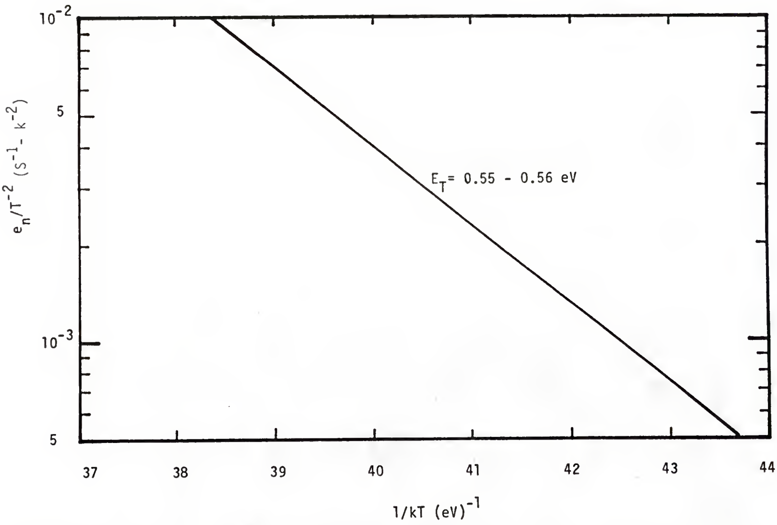

Figure 8.17 Thermal electron emission rates divided by T^2 vs. inverse of temperature for E2 electron trap in the C-10 P_b/N- diode selected from #JFET 2-1358 (P1PC) run.

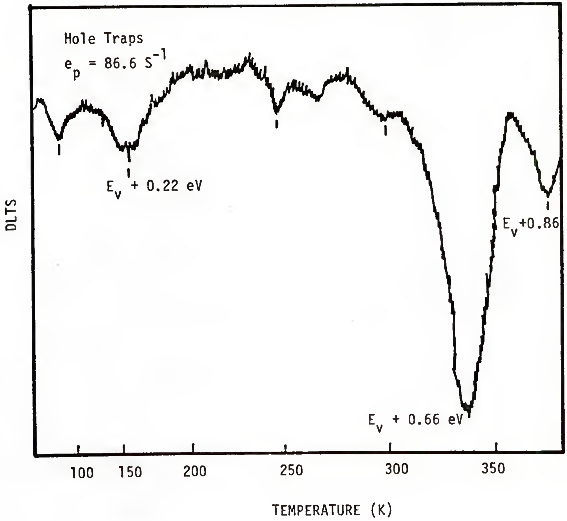

Figure 8.18 DLTS scan of hole traps in the C-10 N_b/P_c BP diode selected from #JFET 2-1358 (P1PC) run.

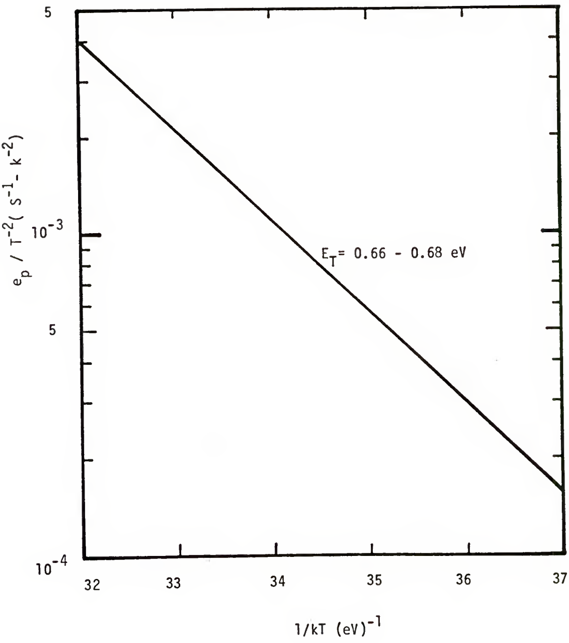

Figure 8.19 Thermal hole emission rates divided by T^2 vs. inverse of temperature for H4 hole trap in the C-10 N_b/P_c BP diode selected from #JFET 2-1358 (P1PC) run.

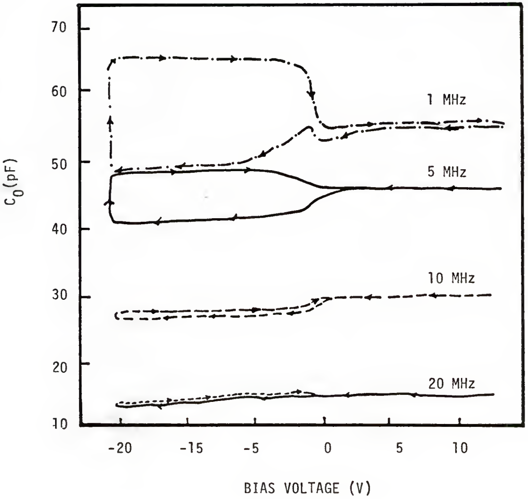

Figure 8.20 C-V curves vs. frequency at T = 300 K for #18 MOS (N-substrate) capacitor selected from run #JFET 2-1358 (P1P2). Hysteresis loop is clearly shown for f < 10 MHz and V < -5V.

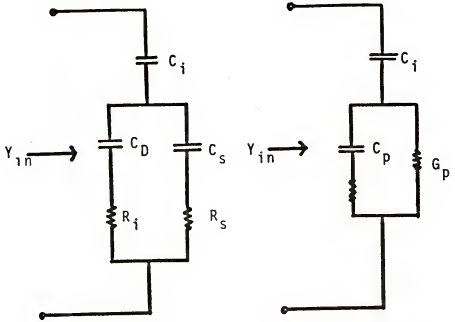

$$\tau = C_s R_s$$

$$C_p = C_D + C_s/(1 + \omega^2 \tau^2)$$
$$G_p = C_s \omega^2 \tau/(1 + \omega^2 \tau^2)$$

(a) (b)

Figure 8.21 Equivalent circuit including interface-trap effect, where C_s and R_s are associated with interface trap density.

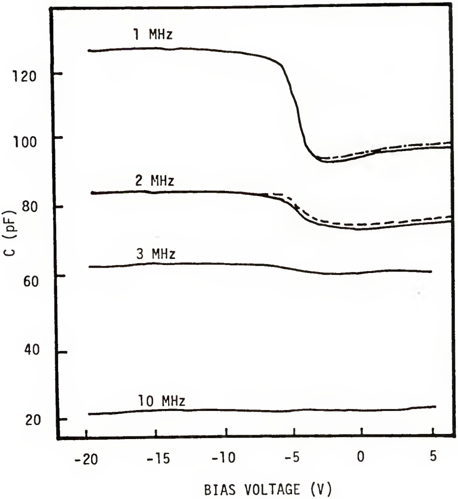

Figure 8.22 C-V curves vs. frequency at T = 300 k for #15 MOS capacitor on P_c-substrate selected from #JFET 2-1358 (P1P2) run. Hysteresis effects is negligible in this capacitor.

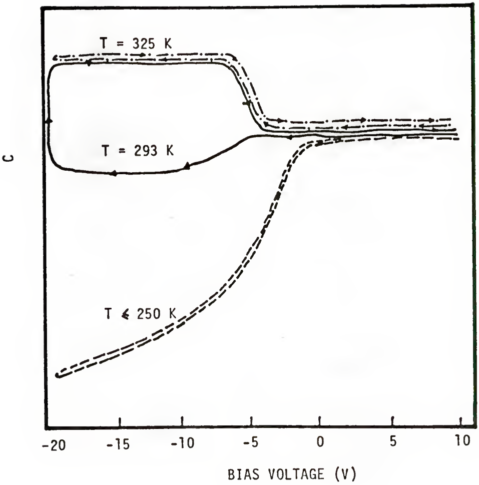

Figure 8.23 C-V plots at 1 MHz as a function of temperature for #18 MOS capacitor with N-substrate selected from #JFET 2-1358 (P1P2) run. Note that hysteresis effect disappears for ≤ 250 k.

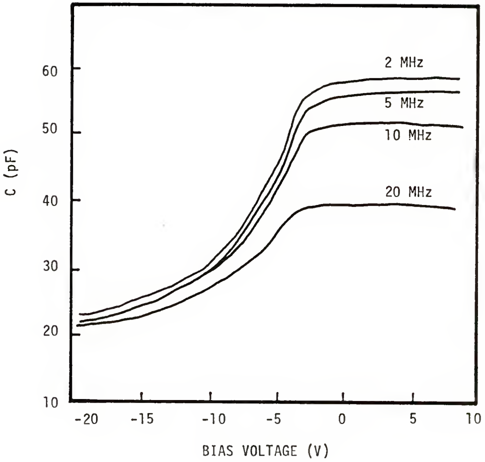

Figure 8.24 C-V plots at 77 K for #18 MOS capacitor (N-substrate) selected from run #JFET 2-1358(P1P2) for f = 2, 5, 10, and 20 MHz. Note that no hysteresis loop is shown in the C-V curves.

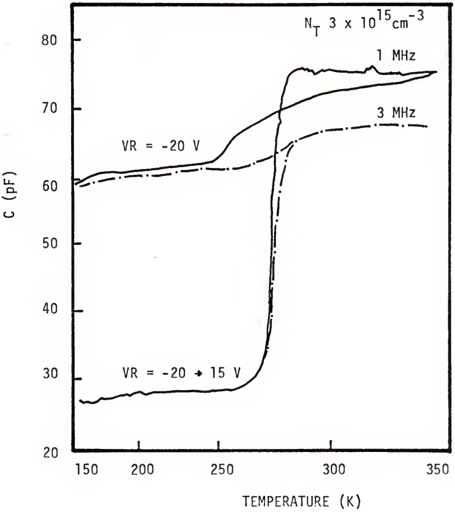

Figure 8.25 The thermally-Stimulated-Capacitance (TSCAP) scans for #18 MOS capacitor (N-substrate) at 1 and 3 MHz from run #JFET 2-1358(P1P2). The capacitance step observed for T > 265 K is due to the electron emission from the trap in the device.

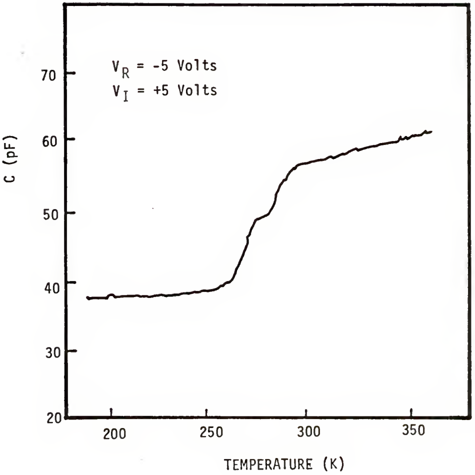

Figure 8.26 TSCAP scan taken at 2 MHz for #13 MOS capacitor (N-substrate) showing electron traps for $250 < T < 300$ k.

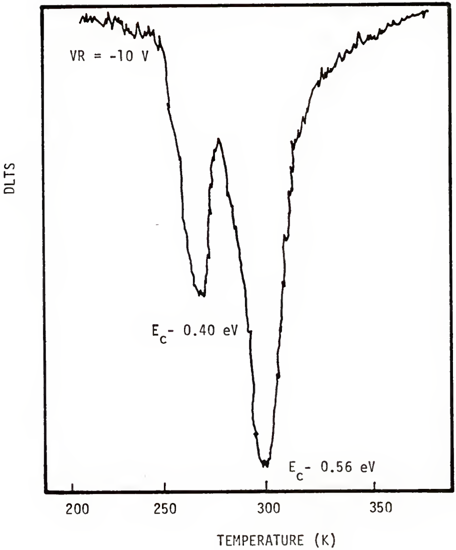

Figure 8.27 DLTS scan of electron traps for #18 MOS capacitor with N-substrate selected from run #JFET 2-1358(P1P2). Two donor-type electron traps were detected.

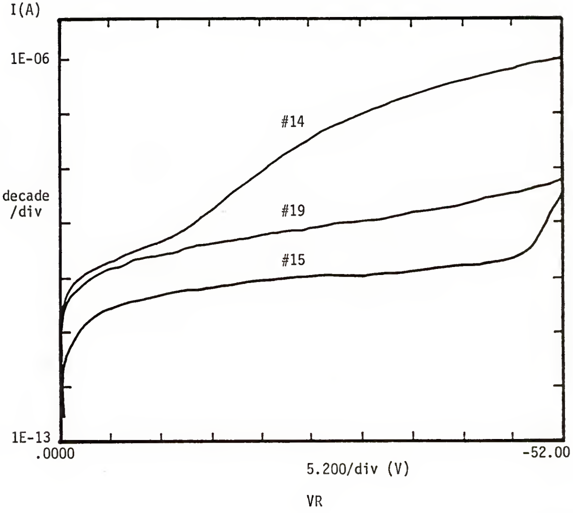

Figure 8.28 Reverse I-V curves for D3 diodes of unit #14, #19 and #15 selected from run #JFET 2-1358 (P2P1) wafer lots.

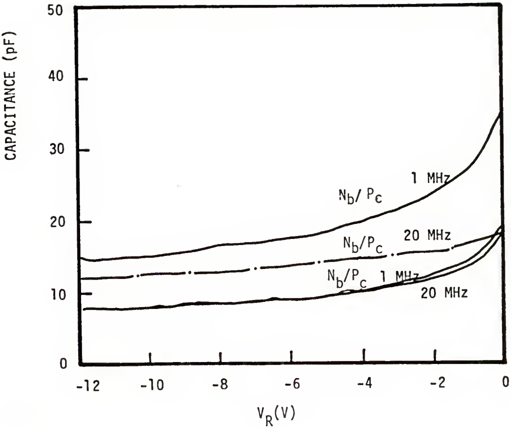

Figure 8.29 Capacitance vs. V_R for diodes D3 and D4 of unit #14 from #JFET 2-1358 (P2P1) run wafer lot.

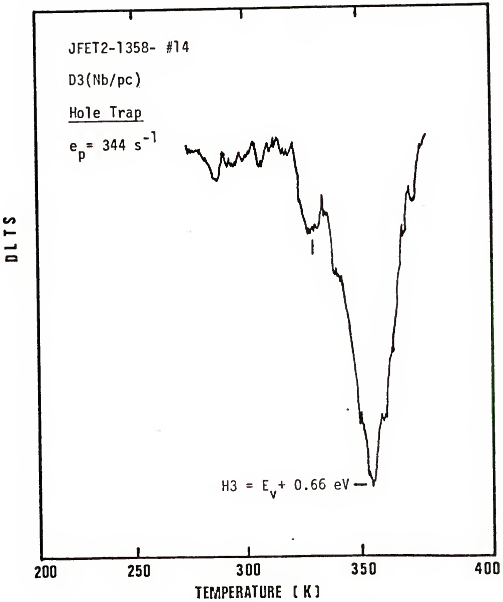

Figure 8.30 DLTS scan of hole trap H3 in the unit #39 D3 diode selected from #JFET 2-1358 (P2P1) run wafer lot.

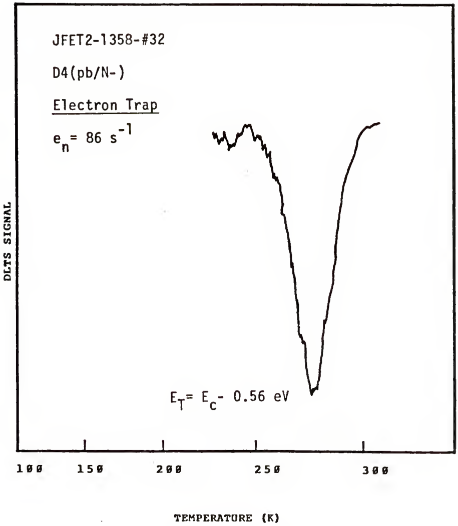

Figure 8.31 DLTS scan of the electron trap E2 in the unit of #32 D4 diode selected from #JFET 2-1358 (P2P1) run wafer lot.

CHAPTER IX
SUMMARY AND CONCLUSION

A theoretical study of the effects of increasing the density of shallow impurity dopants in a degenerate semiconductor device and an experimental study of the metallic contamination on device characteristics has been presented in this dissertation. The highlights and conclusions from this study are summarized as follows:

(1) Expressions for the Debye length, built-in potential and depletion layer width of a heavily-doped pn junction diode as well as a heterojunction diode are reformulated by including the heavy doping effects such as carrier degeneracy, bandgap narrowing, and dopant density-dependent dielectric constant. The results from numerical calculations show that a) bandgap narrowing and carrier degeneracy have important effects on the junction built-in potential; b) the dopant impurity density-dependent constant is the only heavy doping effect which will have a strong influence on the depletion layer width and depletion capacitance; c) the effect of carrier degeneracy will be the dominant heavy doping effect in the heavily-doped GaAs-AlGaAs devices due to the very small electron effective masses in GaAs and AlGaAs.

(2) The generalized Einstein relation for the majority carriers and minority carriers in a heavily-doped semiconductor are

still valid when assuming the parabolic density of states and rigid band approxmations. Additional terms should be added in when considering the impurity band broadening and band tail states instead of employing the parabolic density of states and rigid band approximation.

(3) A closed form expression for the I-V characteristics of a heavily-doped Si n^+p graded junction is presented by modifying the theory of anisotropic heterojunctions, in which, a transition region is modeled to extend beyond the space charge region with a costant bandgap gradient. Numerical analysis show that the effects of heavy doping, especially the bandgap narrowing and the carrier degeneracy, have a significant influence on the electron current density at the quasi-neutral region of a heavily-doped pn graded junction. This is because the bandgap gradient affects the transport of the injected minority carriers by influencing the carrier distribution in the quasi-neutral regions.

(4) The theoretical analysis of the effects of heavy doping on the electrical characteristics for GaAs JFETs and MESFETs show that the carrier degeneracy has a significant effect on the threshold voltage and the I-V characteristics of heavily-doped E-JFETs and E-MESFETs, while the bandgap narrowing has negligible influence on the electrical characteristics because of the very small electron effective mass.

(5) From the analysis of I-V, C-V, TSCAP, and DLTS data on the metallic contaminated silicon diodes and MOS capacitors, we

conclude that a) the metallic contaminants presented in the tested devices will introduce several deep level hole and electron traps. The main hole trap is due to the Ev + 0.66 eV level and the main electron trap is due to the Ec - 0.56 eV level with the average strap density in the low to mid 10^{14} cm^{-3} range; b) the results of I-V and DLTS measurements show that the reverse leakage current is closely related to the density of metallic contaminant induced traps in the corresponding tested devices; c) experimental evidence from the C-V, TSCAP, and DLTS measurements indicate that the metallic contamination will influence the temperature and frequency dependence of the high frequency C-V behavior in the tested MOS capacitors. An abnormal hysteresis behavior was also observed; d) the results of the measured 1/f figures showed only a certain degree of correlation to the density of metallic contaminant induced deep level trap.

The theoretical and experimental studies presented in this dissertation will certainly help us to obtain a better understanding of the effects of heavy doping and metallic contamination on the electrical characteristics of silicon devices, and the theoretical reults derived from this research may be applied to study other III-V compound semiconductor devices.

APPENDIX
DERIVATION OF THE DEPLETION LAYER WIDTH VS. BUILT-IN POTENTIAL FOR A HEAVILY DOPED LINEARLY GRADED PN JUNCTION

To derive an expression for the depletion layer width, x_{dL}^{H}, vs the modified built-in potential, ϕ_{bi}^{H}, in a heavily doped linearly graded pn junction taking into account of the effects of carrier degeneracy, impurity density-dependent dielectric constant, and bandgap narrowing, we consider a heavily-doped linearly graded junction with the space charge regions located at $-x_{pL}^{H}$ and x_{nL}^{H}, and a net dopant concentration gradient, a. Thus, the net dopant density in this linearly graded junction may be represented by $N_D - N_A = ax$. From discussions given in section 2.1, the dopant impurity density-dependent dielectric constant, $K_{sn}(x)$ and $K_{sp}(x)$, for a linearly graded pn junction can be expressed by

$$K_{sn}(x) = A_n\, e^{B_n N_{xn}} \quad ; \qquad 0 < x < x_{nL}^{H} \tag{A-1}$$

$$K_{sp}(x) = A_p\, e^{B_p N_{xp}} \quad ; \qquad -x_{pL}^{H} < x < 0 \tag{A-2}$$

where, $N_{xn} = N_D - N_A = ax$, and $N_{xp} = N_A - N_D = -ax$. The Gauss law, including the effect of impurity density-dependent dielectric constant, is given by

$$\nabla\,(K_s(x)\; E(x)) = \rho/\varepsilon_0 \tag{A-3}$$

Since $E(x_{nL}^{H}) = E(x_{pL}^{H}) = 0$, we obtain

$$E(x) = -\frac{qa}{\varepsilon_o K_{sn}(x)} \frac{1}{2} (x_{nL}^{H2} - x^2) \quad ; \quad 0 < x < x_{nL}^{H} \qquad \text{(A-4)}$$

$$E(x) = \frac{qa}{\varepsilon_o K_{sp}(x)} \frac{1}{2} (x^2 - x_{pL}^{H2}) \quad ; \quad -x_{pL}^{H} < x < 0 \qquad \text{(A-5)}$$

Thus, the potential can be expressed by

$$\phi(x) = \phi_n - \frac{qa}{2\varepsilon_o} \int_{x}^{x_{nL}^{H}} \frac{1}{A_n \exp(B_n ax)} (x_{nL}^{H2} - x^2)\, dx \quad ; \quad 0 < x < x_{nL}^{H} \qquad \text{(A-6)}$$

$$\phi(x) = \phi_p - \frac{qa}{2\varepsilon_o} \int_{-x_{pL}^{H}}^{x} \frac{1}{A_p \exp(-B_p ax)} (x^2 - x_{pL}^{H2})\, dx \; ; \; -x_{pL}^{H} < x < 0 \qquad \text{(A-7)}$$

where, we have substituted Eqs. (A-1) and (A-2) into Eqs. (A-4) and (A-5). By using integration by parts, Eqs. (A-6) and (A-7) are reduced to:

$$\phi(0) = \phi_n - \frac{qa}{2\varepsilon_o A_n}\left[-\frac{1}{C_n}(x_{nL}^{H})^2 + \frac{2}{C_n^2} e^{C_n x_{nL}^{H}} \cdot x_{nL}^{H} - \frac{2}{C_n^3}(e^{C_n x_{nL}^{H}} - 1)\right] \qquad \text{(A-8)}$$

$$\phi(0) = \phi_p - \frac{qa}{2\varepsilon_o A_p}\left[-\frac{1}{C_p}(x_{pL}^{H})^2 + \frac{2}{C_p^2} e^{-C_p x_{pL}^{H}} \cdot x_{pL}^{H} - \frac{2}{C_p^3}(e^{-C_p x_{pL}^{H}} - 1)\right] \qquad \text{(A-9)}$$

where, $C_n = -B_n a$, and $C_p = B_p a$. Thus, the built-in potential, ϕ_{bi}^{H}, for the heavily-doped linearly graded pn junction can be obtained from Eqs. (A-8) and (A-9) as

$$\phi_{bi}^{H} \equiv \phi_n - \phi_p$$

$$= \frac{qa}{2\varepsilon_o} \{\frac{1}{A_n} [- \frac{1}{4C_n} (x_{dL}^{H})^2 + \frac{1}{C_n^2} e^{\frac{1}{2}C_n x_{dL}^{H}} \cdot x_{dL}^{H} - \frac{2}{C_n^3}(e^{\frac{1}{2}C_n x_{dL}^{H}} - 1)]$$

$$- \frac{1}{A_p} [- \frac{1}{4C_p} (x_{dL}^{H})^2 + \frac{1}{C_p^2} e^{-\frac{1}{2}C_p x_{dL}^{H}} \cdot x_{dL}^{H} - \frac{2}{C_p^3}(e^{-\frac{1}{2}C_p x_{dL}^{H}} - 1)]\} \quad \text{(A-10)}$$

where determination of x_{dL}^{H} is made possible by iterating Eqs. (12) and (A-10). It is noted that values of K_{sn} and K_{sp}, which appeared in Eq. (A-10) in terms of A_n, B_n, A_p, and B_p, are determined from fitting the experimental data [2].

REFERENCES

1. N.G. Nilsson, Appl. Phys. Lett., 33, 653 (1978).

2. K.F. Berggren and B.E. Sernelius, Phys. Review B, 24, 1971 (1981).

3. M.H. Andrews, A.H. Marshak, and R. Shrivastava, J. Appl. Phys., 52, 6783 (1981).

4. T.G. Castner, N.K. Lee, G.S. Gieloszyk, and G.L. Salinger, Phys. Rev. Lett., 34, 1627 (1975).

5. W.P. Dumke, Appl. Phys. Lett., 43, 196 (1983).

6. G.E. Possin, M.S. Adler, and B.J. Baliga, IEEE Trans. Elec. Devices, ED-27, 983 (1980).

7. A. Neugroschel, S.C. Pao, and F.A. Lindholm, IEEE Trans. Elec. Devices, ED-29, 894 (1982).

8. J.W. Blakemore, Solid-State Electronic, 25, 1067 (1982).

9. R.S. Muller and T.I. Kamins, Device Electronics for Integrated Circuits, John Wiley and Sons, Inc., 1977.

10. C. Kittel and H. Kroemer, Thermal Physics, 2nd Ed., W.H. Freeman and Co., 1980.

11. S.M. Sze, Physics of Semiconductor Devices, 2nd Ed., John Wiley and Sons, Inc., 1981.

12. B.R. Chawla and H.K. Gummel, IEEE Trans. Electron Devices, ED-18, 178 (1971).

13. P.T. Landsberg, Proc. Roy. Soc., A213, 226 (1952); Proc. IEEE, 71, 476 (1973).

14. S.S. Li and F.A. Lindholm, Proc. IEEE, 56, 1256 (1968).

15. K.M. Van Vliet and A.H. Marshak, Phy. Stat. Sol.(b), 78, 501 (1976).

16. D.D. Tang, IEEE Trans. Elec. Devices, ED-27, 563 (1980).

17. A. Neugroschel and F.A. Lindholm, Appl. Phys. Lett., 42, 176 (1983).

18. D. Dziewior and D. Silber, Appl. Phys. Lett., 35, 170 (1979).

19. R.P. Mertens, J.L. Van Meerbergen, J.F. Nijs, and R.J. Van Overstraeten, IEEE Trans. Elect. Devices, ED-27, 949 (1980).

20. J. Van Meerbergen, J.F. Nijs, R.P. Overstraeten, Proc. Photovoltaic Specialists Conf., 66 (1978).

21. P.A. Iles and S.I. Soclof, Proc. Photovoltaic Specialists Conf., 19 (1979).

22. D.E. Burk and V. de la Torre, IEEE Trans. Elect. Devices, EDL-5, 231 (1984).

23. S. Othmer, Scanning Elect. Microscopy, 1, 727 (1978).

24. J.W. Slotboom, Solid-state Electronics, 20, 279 (1977).

25. Van Cong, Phys. Stat Sol. (A), 65, 863 (1981); 68, 697 (1981).

26. M.A. Shibib, Ph.D. Dissertation, University of Florida, 1979.

27. W.L. Kauffman and A.A. Bergh, IEEE Trans. Elect. Devices, ED-15, 732 (1968).

28. D. Buhanan, IEEE Trans. Elect. Devices, ED-16, 117 (1969).

29. J.W. Slotboom and H.C. Degraaf, Solid-State Electronics, 19, 857 (1976).

30. H.P.D. Lanyon, A.K. McCurdy, and R.A. Tuft, Proc. Photovoltaic Specialists Conf., 60 (1978).

31. A. Neugroschel, P.J. Chen, S.C. Pao, and F.A. Lindholm, Proc. Photovoltaic Specialists Conf., 70 (1978).

32. A.W. Wieder, IEEE Trans. Elect. Devices, ED-27, 1402 (1980).

33. A. Chatterjee and A.H. Marchak, Solid-State Electronics, 26, 59 (1983); 24, 1111 (1981).

34. A.G. Milnes and D.L. Feucht, Heterojunctions and Metal Semiconductor Junctions, Academic Press, New York (1972).

35. W.G. Oldham and A.G. Milnes, Solid-State Electronics, 6, 12 (1963).

36. M.N. Alexander and D.F. Halcomb, Rev. Mod. Phys., 40, 815 (1968).

37. N. Kobayashi, S. Ikehata, S. Lobayashi and W. Sasaki, Solid-State Commun., 24, 67 (1977).

38. R.W. Keyes, Solid-State Commun., 32, 179 (1979).

39. H.K. Kroemer, Proc. IEEE, 70, 13 (1982).

40. M. Morkoc and P.M. Solomon, IEEE Spectrum, 28 (1984).

41. W.G. Oldham and A.G. Milnes, Solid-State Electronics, 6, 121 (1967).

42. H.C. Casey, Jr. and M.B. Panish, Heterojunction Lasers, Academic Press, New York, 1978.

43. R.C. Eden, A.R. Livingston, and B.M. Welch, IEEE Spectrum, 20, 30 (1983).

44. R. Zuleeg, J.K. Notthoff, and K. Lehovec, IEEE Trans. Elect. Devices, ED-25, 628 (1978).

45. N. Kato, Y. Matsuoka, K. Ohwada, and S. Moriya, IEEE Elect. Device Lett., EDL-4, 417 (1983).

46. N. Nakamura, Y. Sano, T. Nonaka, T. Ishida, and K. Kaminishi, GaAs IC Symp. Tech. Dig., 134 (1983).

47. P.C. Chao, W.H. Ku, and J. Nulman, IEEE Elect. Device Lett., EDL-4, 9, 326, (1983).

49. N. Kato, K. Yamasaki, K. Asai, and K. Ohwada, IEEE Trans. Elect. Devices, ED-30, 6, 663 (1983).

50. C.L. Chen and K.D. Wise, IEEE Electron Device Lett., EDL-4, 10, 341 (1983).

51. H. Daembkes, W. Brockerhoff, K. Heime, and A. Cappy, IEEE Trans. Elect. Devices, ED-31, 1032 (1984).

52. K.E. Drangeid and R. Sommerhalder, IBM J. Res. Develop., Mar., 82 (1970).

53. H.C. Casey, Jr. and F. Stern, J. Appl. Phys., 47, 631 (1976).

54. R. Zuleeg and J.K. Notthoff, IEEE Trans. Nuclear Science, NS-24, 2305 (1977).

55. H. Hilsum, Electron Lett., 10, 259 (1974).

56. P.W. Lai, Master Thesis, University of Florida (1979).

57. C.T. Sah, Solid-State Electronics, 13, 759 (1970).

58. R.R. Senechal and J. Basinski, J. Appl. Phys., 39, 3723 (1968); J. Appl. Phys., 39, 4581 (1969).

59. C.T. Sah, W.W. Chan, H.S. Fu, and J.W. Walker, Appl. Phys. Lett., 20, 193 (1972).

60. C.T. Sah and J.W. Walker, Appl. Phys. Lett., 22, 384 (1973).

61. C.T. Sah, C.T. Wang, and S.H. Lee, Appl. Phys. Lett., 24, 523 (1974).

62. D.V. Lang, J. Appl. Phys., 45, 3014 (1974).

63. D.V. Lang, J. Appl. Phys., 45, 3023 (1974).

64. H. Okuski and Y. Tokumaru, Jap. J. Appl. Phys., 20, L45 (1982).

65. H. Tomokage, H. Nakashima, and K. Hasimoto, Jap. J. Appl. Phys., (1981).

66. W. Schottky and W.T. Read, Jr., Phys. Rev., 835 (1952).

67. C.H. Henry and D.V. Lang, Phys. Rev. B, 15, 989 (1977).

68. E.R. Weber and N. Wifhl, Mat. Res. Soc. Symp. Proc., 14, 19 (1983).

69. A. Rohatgi, J.R. Davis, R.H. Hopkins, and P.G. McMullin, Solid-State Electronics, 26, 1039 (1983).

70. L.C. Kimerling, J.L. Benton, and J.J. Rubin, Inst. Phys. Conf., 49, 217 (1981).

71. J.L. Benton and L.C. Kimerling, J. Electrochem. Soc., 129, 2098 (1982).

72. K. Graff and H. Pieper, Semiconductor Silicon, The Electrochemical Society Soft-bound Proceedings Series, Pennington, NJ, 1981.

BIOGRAPHICAL SKETCH

Ker-Weng Teng was born in Taipei, Taiwan, Republic of China, on June 8, 1954. He attended the Taipei Municipal Chen-Kuo High School in 1970 through a competative entrance examination.

In June 1977, he received the Batchelor of Science degree from the Department of Physics, National Tsing Hua University, Hsinchu, Taiwan. He started the graduate studies in electrical engineering at the University of Florida in September 1979, and received a Master of Science degree in December 1981. Since 1980, he has been a graduate research assistant at Solid-State Electronics Laboratory.

His research interests are in semiconductor device physics, semiconductor device modeling, computer aided IC circuit design, and quantum electronics. He is a member of the Institute of Electrical and Electronic Engineers.

I certify that I have read this study and that in my opinion it conforms to acceptable standards of scholarly presentation and is fully adequate, in scope and quality, as a dissertation for the degree of Doctor of Philosophy.

Sheng San Li

Sheng S. Li. Chairman
Professor of Electrical Engineering

I certify that I have read this study and that in my opinion it conforms to acceptable standards of scholarly presentation and is fully adequate, in scope and quality, as a dissertation for the degree of Doctor of Philosophy.

A. Neugroschel

Arńost Neugroschel
Professor of Electrical Engineering

I certify that I have read this study and that in my opinion it conforms to acceptable standards of scholarly presentation and is fully adequate, in scope and quality, as a dissertation for the degree of Doctor of Philosophy.

D. S. Burk

Dorothea Burk
Assistant Professor of Electrical
Engineering

I certify that I have read this study and that in my opinion it conforms to acceptable standards of scholarly presentation and is fully adequate, in scope and quality, as a dissertation for the degree of Doctor of Philosophy.

Tim Anderson

Tim Anderson
Professor of Chemical Engineering

I certify that I have read this study and that in my opinion it conforms to acceptable standards of scholarly presentation and is fully adequate, in scope and quality, as a dissertation for the degree of Doctor of Philosophy.

Paul H Holloway

Paul H. Hollaway
Professor of Material Engineering

This dissertation was submitted to the Graduate Faculty of the College of Engineering and to the Graduate Council, and was accepted as partial fulfillment of the requirements for the degree of Doctor of Philosophy.

December 1984

Herbert A. Bevis

Dean, College of Engineering

Dean, Graduate School